IMPERIAL COLLEGE LONDON OF SCIENCE, TECHNOLOGY AND MEDICINE

DEPARTMENT OF AERONAUTICS

AERODYNAMIC ANALYSIS OF MORPHING AIRFOILS IN DYNAMIC STALL USING THE ONERA MODEL

FINAL YEAR PROJECT

SUPERVISORS
Dr. Joaquim Peirò
Ch. Mo Prof. Ugo Galvanetto

STUDENT
Matteo Duzzi
CID 00715102

ABSTRACT

This study is divided in two sections: the first one concerns dynamic stall in two-dimensional flow, and more precisely the modeling of the global aerodynamic forces by means of differential equations. The equations used are based on the ONERA dynamic stall model. This model considers an airfoil subjected to a free stream with two degrees of freedom (dof): the pitch angle $\theta$and the plunge displacement h. This two dof enable the evaluation of the aerodynamic coefficients and forces through the implementation of the ONERA model in a MATLAB code. The differential equations are solved using the standard ODE solvers (ode15s).

The second section of the paper, which is the most important one and that is based on the first one, is about morphing airfoils. The unified model presented is composed by three components coupled together. The basic idea is that the airfoil motions (given by the angle of attack and the morphing dynamics) are transformed into a generalized set of coordinates (h_n and $h_n^{'}$). These generalized coordinates with the flowfield geometry (u_0, v_0, v_1) and the induced flow λ_n provide the boundary conditions used for the linear airloads theory. That process provides the generalized loads L_n (first component of the theory). The second component of the model is the induced flow model. This part is obtained by the simultaneous use of the linear loads and the eventual modifications due to stall. From the induced flow model is derived the flow due to the shed wake λ_n. The third and last part of the model is the dynamic stall model: the ONERA model. The idea is that the airfoil boundary condition in terms of generalized coordinates is used as a representation of the non-linear static stall data in order to get the static stall corrections for the loads (ΔC_n). These corrections drive the dynamic stall model which produces the corrections (Γ_{2n}) that have to be applied to the loads. This procedure is formulated as a feedback loop. The corrections guarantee the time delay and overshoot typical of dynamic stall behavior. Finally, the linear loads and the corrections are combined to obtain the total airload.

The validation of the unified model is accomplished by comparison with Theodorsen theory for harmonic motions correlating NACA 0012 dynamic stall data. Other simulations have been carried on for NACA 0012 airfoil with trailing edge flap and for the SC-1095 airfoil with leading edge droop. These correlations show good agreement with the experimental data obtained in wind tunnel tests.

CONTENTS

LIST OF TABLES

LIST OF FIGURES

NOMENCLATURE

The nomenclature used is divided by Chapter to prevent confusion with similar abbreviation. The nomenclature not repeated is the same for all the chapters.

Chapter 3

C_q	generic parameter of the system
C_{qs}	static value of C_q
θ	control parameter of the system, [rad]
θ_0	average position, [rad]
$a, b, c, \ldots$	coefficients
Q	load
Q_1	load in absence of stall
Q_2	load due to dynamic stall
ΔQ	static load residual
$\hat{\lambda}, \hat{s}, \hat{\sigma}, \hat{a}, \hat{r}, \hat{e}$	semi-empirical coefficient of ONERA model
τ	reduced time
U	free stream velocity, [m/s]
t	time, [s]
b	semi-chord, [m]
ΔC_z	measure of stall

Chapter 3.3

ρ	density, [kg/m^3]
Q	circulatory airfoil motion expression

$C(k)$	Theodorsen lift deficiency function
h	plunge variable
α	pitch variable
w	frequency
k_n	curvature variables

Chapter 4

$\theta(t)$	forced oscillation, [rad]
θ_m	mean angle of attack, [rad]
θ_a	amplitude of the oscillation, [rad]

Chapter 5

u_0	horizontal velocity, [m/s]
v_0	vertical velocity, [m/s]
v_1	rotation, [m/s]
w	total induced flow, [m/s]
$\bar{v}$	induced flow from bound circulation, [m/s]
λ	induced flow from shed circulation, [m/s]
γ_b	bound circulation per unit length, [m/s]
γ_w	wake circulation per unit length, [m/s]
ΔP	pressure drop across airfoil, [N/m^2]
ξ	dummy variable of integration
φ	Glauert variable, [rad]
$\gamma_s, \gamma_0, \gamma_n$	expansion coefficients of γ_b
τ_s, τ_0, τ_n	expansion coefficients of ΔP
h	generalized blade deformation, [m]

h_n	components of the generalized blade deformation, [m]
w_n	components of the generalized total velocity field, [m/s]
λ_n	components of the generalized velocity due to the shed wake, [m/s]
L_n	generalized loads per unit span, [N/m]
Γ	total bound circulation, [m^2/s]
D	drag force
b_n	induced flow expansion coefficients
Γ_{n2}	change in circulation due to dynamic stall of *n*th generalized load, [m^2/s]
Γ_{n1}	circulation of the linear lift coefficient
ΔC_l	static lift residual
$\hat{\omega}, \hat{\eta}, \hat{\epsilon}$	semi-empirical coefficients of ONERA model
$C_{l\alpha}$	static correction factor
$C_{l(l)}$	linear part of the lift coefficient
Re	Reynolds Number
Ma	Mach Number

Chapter 6

C_l	lift coefficient
α	angle of attack, [rad]
α_{ss}	static stall angle, [rad]
α_{shift}	shift in stall initiation angle, [rad]
z	shift variable
z_0	value of z below which ΔC_n is negligible
α_{0l}	angle of zero lift, [rad]

$h_n^{'}$	component of spatial gradient of airfoil meanline
C_{l0}	coefficient of lift at $\alpha = 0$
$C_{l(e)}$	experimental value of the C_l
$C_{l(ss)}$	value of the C_l at static stall angle
C_d	coefficient of drag
a	location of center of rotation aft of mid-chord
ΔC_m	static pitching moment residual
C_{m0}	moment coefficient at $\alpha = 0$
$C_{m\alpha}$	slope of the moment curve
$C_{m(e)}$	experimental value of the C_m
m	maximum ordinate mean line in percent chord
p	chord-wise position of maximum ordinate in tenths of chord

Chapter 7

E	fitness function
g	experimental data
$\hat{g}$	numerical solution
$k = wb/u_0$	reduced frequency of the test

Chapter 8

$C(k)$	Theodorsen lift deficiency function
a	distance respect to b at which the pitching motion is applied
d	location of trailing edge flap or droop hinge aft of mid-chord
β	trailing edge flap deflection, [rad]

ϕ	phase angle between pitch and flap input, [rad]
φ_m	Glauert variable at the flap hinge location d, [rad]
f_α	static correction factor to angle of attack
f_l	static correction factor to lift coefficient
a_c	static correction to center of rotation
f_β	static correction factor to trailing edge flap input
f_m	static correction factor to pitching moment coefficient
$C_{m(t)}$	theoretic value of C_m
t_n	components of vector $\{T\}_{flap}$

Chapter 9

α_m	mean angle of attack, [rad]
α_a	amplitude of the oscillation, [rad]

Appendix E

$\nabla^2\phi$	Laplace's equation
ϕ	velocity potential
T_n	Chebyshev polynomials
A_n	magnitude of Chebyshev polynomials contributing to the complete airfoil shape
$y(x,t)$	airfoil shape
σ	strength of the source/sink
X	x location in reference plane
Y	y location in reference plane
x	x location in mapped plane
y	y location in mapped plane

p_0	total pressure
p	pressure
p_∞	free stream pressure
U'	disturbance velocity in x direction
L_{NC}	non circulatory lift
h	plunge variable
α	pitch variable
k_n	high order shape terms
Γ	point vortex circulation
L_C	circulatory lift
γ_w	wake vorticity per unit length
Q	circulatory airfoil motion expression
$\bar{h}$	plunge amplitude
$\bar{\alpha}$	pitch amplitude
$\bar{k}_n$	curvature amplitude
w	frequency
k	reduced frequency
φ_{k_n}	phase angle of the motions
$F(k)$	real part of Theodorsen's function
$G(k)$	imaginary part of Theodorsen's function
i	imaginary number
$H_n(k)$	Hankel function
$J_n(k)$	Bessel function of the first kind
$Y_n(k)$	Bessel function of the second kind
$\dot{(\,)}$	$\partial(\,)/\partial t$
$\ddot{(\,)}$	$\partial^2(\,)/\partial t^2$

1) INTRODUCTION TO DYNAMIC STALL AND MORPHING AIRFOILS

An airfoil is dynamically stalling when its angle of incidence leads to a vortex-like disturbance. This disturbance, which originates near the leading edge and moves along the airfoil, is responsible for a highly non-linear pressure disturbance. The non-linearity causes the divergence between the airloads predicted from the linear thin-airfoil theory and those obtained by experimental tests.

Dynamic stall is one of the most challenging problems in aerodynamics and is a typical phenomenon of helicopters rotors. The difficulty is related to the fact that the rotor faces with different aerodynamic environments simultaneously: the advanced side of the rotor is characterized by a large Mach number and low angles of attack while the retreating side experiences lower Mach numbers and larger angles of attack, causing the airfoil to stall. This cyclic variation leads to the phenomenon of dynamic stall. The bigger difference between static and dynamic stall is that the dynamic stall limits the maximum forward velocity of the rotor. In addition, it causes torsional solicitations and vibrations [29]. All these effects are time-dependent and this is the reason why this type of stall has to be studied from a dynamic point of view.

There is a large number of works concerning the static stall that uses data collected from wind tunnels. This is partially due to the simplicity of setting up the static experiments: the airfoil is simply fixed in a particular position with a determinate angle of attack relative to the free stream. It has only one degree of freedom, i.e. the angle of attack (pitch). Data are collected at different angles in order to evaluate the aerodynamic forces in each configuration. The static stall phenomenon is well understood and it is not the purpose of this work to deal with it, but it has a key role in the determination of the dynamic stall's parameters.

On the other hand there are only a few theories of dynamic stall and there is not a complete physical model yet. The models are designed to match experimental data through the application of nonlinear equations. The main problem of this approach is that the equations need some empirical coefficients that are strictly correlated with the

experimental data and thus, if there are no data available for a particular airfoil or flow condition, it is impossible to obtain realistic information. Several semi-empirical models exist that can be used to simulate dynamical stall behavior. One of these models is the ONERA model, implemented by Petot [1] and extended by Peters and Rudy [3]. ONERA developed a model of dynamic stall in which a first-order equation coupled with mass terms is used to get a reasonable approximation of the rigid unstalled airfoil behavior. A second-order filter is then fed by the changes in stall observed in static test data to simulate the delay of stall onset and the stall overshoot. This semi-empirical model is adopted in this work to compute dynamic stall.

This study makes a further step towards the comprehension of this phenomenon and investigates the possibility to create morphing airfoils to improve their efficiency and alleviate the dynamic stall. There has been increasing interest in dynamically morphing airfoils, due to the need for heavy-lift applications as well as noise and vibration reduction. This is also more feasible thanks to the improvements in structural technology, materials and adaptive controls. Reference [8] describe the use of a trailing edge droop to mitigate the effects of dynamic stall including testing data. In Reference [22] Mac Gaunaa shows that it is possible to obtain a load reduction using deformable trailing edge geometry (DTEG). The model implemented was used to investigate the effect of the DTEG control system on flutter velocity in two-dimensional cases. The results indicate that the relative air velocity at which instabilities occurs may be reduced significantly with the addition of a DTEG control system. This is directly related with the load reduction because the instabilities cause a reduction of effectiveness in creating lift.

In Reference [24] the authors investigate a possible reduction of the cost of wind-generated electricity by mitigating fatigue loads acting on the blades of wind turbine rotors. The study adopts active aerodynamic load control devices like trailing edge tabs and flaps for mitigation. The work is focused on the time-dependent effects on sectional lift, drag and pitching moment given by the use of these micro-devices and their effectiveness in mitigating high frequency loads on the wind turbine. The goal of the study is to compare the transient aerodynamic characteristics of the microtab and microflap, to determine the deployment time requirements for these devices, and to assess the occurrence of any nonlinear aerodynamic phenomena during their deployment. The results show that the deployment transients dissipate leading to an asymptotic rise towards a steady-state response. Reference [25] also makes an analysis of the operating conditions of wind turbines, which are subjected to fluctuating loads that create fatigue damage on their components. The results show that the use of variable geometry

airfoils is an effective way to reduce vibration on an airfoil when subjected to stochastic wind signals.

In Reference [23], the author derived analytical expressions for distributed and integral unsteady two-dimensional forces on a variable geometry airfoil undergoing arbitrary motion under the assumption of incompressible, irrotational, inviscid flow. The airfoil is represented by its camber line as in classic thin-airfoil theory and the deflection of the airfoil is given by superposition of chord-wise deflection mode shapes. The analytical expressions derived for the forces simplify to the thin-airfoil results by Theodorsen [11] in case of unsteady flow over a flat airfoil with a flat flap. The thrust predicted with the algorithm implemented is in complete agreement with Garrick's [15] results.

1.1) OBJECTIVES OF THE PROJECT

This work follows the studies conducted by Loren A. Ahaus [4]. The most important goal is to derive a unified airloads theory for morphing airfoils integrated with ONERA dynamic stall model. This theory is not developed to supplant wind tunnel tests and CFD analysis but rather is intended for preliminary design calculations and simulations. In fact, due to the complex non-linearity of the phenomenon, CFD methods need adequate transition models and must solve Navier-Stokes equations to obtain reasonable solution. This is very onerous in terms of time integration and computing time and hence semi-empirical models are quite popular for the calculation of dynamic stall for rotors used in helicopters propellers and wind turbines, also because they provide better results than most CFD computations.

The work presents a brief but complete description of the dynamic stall phenomenon (Chapter 2) in which are analyzed all the typical phases: from the unstalled airfoil to the complete flow separation when the leading edge vortex reaches the trailing edge of the airfoil.

In Chapter 3 are described the basis of the ONERA model and its applications to dynamic stall of airfoils as developed by Petot [1].

Chapter 4 contains the verification and validation of the ONERA model through some simulations regarding an airfoil subjected to three different forced oscillation. The results are then compared with McCroskey experimental data [9].

Peters, *et al.*, developed a finite-state aerodynamic model via expansions in Glauert series [13], [18], [19]. This model is adopted in the current work to evaluate the linear airloads and it is the subject of

Chapter 5. The model is based on two-dimensional potential flow theory with the non-penetration boundary condition applied on the airfoil and the Kutta condition applied at the trailing edge. The theory is developed in terms of the Chebyshev polynomials which are a natural coordinate systems for airfoil motions. Further, only a limited numbers of polynomials are required to capture the essential physics of the phenomenon. For example, a symmetric airfoil like NACA 0012 undergoing simple pitch motions requires only two terms of the expansion. Obviously, if a more complicated airfoil is studied (like a cambered one), then more terms have to be added. For this reason the model is considered general and computationally efficient, making it a good tool for preliminary design calculations. Another interesting feature is that any induced-flow model can be incorporated in the theory (both two- or three-dimensional).

Chapter 6 contains the static airfoil section characteristics. These are essential for the calculation of the residuals both for NACA 0012 and SC-1095 airfoils, which are the driver of the dynamic stall model.

In Chapter 7 is outlined the procedure used to identify appropriate stall parameters. Through large amplitude test data the parameters are obtained both for NACA 0012 and SC-1095 airfoils and are then implemented into the ONERA model's equations.

In Chapter 8 is verified the accuracy of the airload theory with the dynamic stall data. NACA 0012 airfoil is used both for harmonic pitch and flap simulations and combined pitch and flap oscillations whereas the SC-1095 airfoil is used to predict airloads for a drooped leading edge. The results obtained are satisfying.

Chapter 9 shows the camber effects in dynamic stall with harmonic oscillations. The airfoils selected are NACA 0012 and NACA 6712. The simulations demonstrate that a relevant parameter for the dynamic stall is the reduced frequency k. In fact, when the frequency is raised it is possible to notice a significant dynamic stall effect.

Finally, in Chapter 10 is presented a comparison between the results obtained from the original ONERA model and the unified model. From the simulations, it is possible to conclude that the implementations of the ONERA model are in good agreement with the experimental data only when the lift coefficient is considered.

2) DESCRIPTION OF THE DYNAMIC STALL PHENOMENON

This section describes the physics of dynamic stall. The information are taken from Ing. C. Marongiu [5] and from Reference [10]. J. G. Leishman [28] provides a complete description of this phenomenon, reported here for clarity.

“The phenomenon of dynamic stall has long been known to be a factor that limits helicopter performance. The problem of dynamic stall usually occurs on the rotor at high forward flight speed or during maneuvers with high load factors and is accompanied by the onset of large torsional airloads and vibrations on the rotor blades. Whereas for fixed wing aircraft, stall occurs at low flight speeds, stall on a helicopter rotor will occur at relatively high airspeeds as the advancing and retreating blades begin to operate close to the limits where the flow can feasibly remain attached to the airfoil surfaces. The advancing blades operates at low values of angle of attack but close to its shock induced flow separation boundary. The retreating blade operates at much lower Mach numbers but encounters very high values of angle of attack close to stall. Because of the time varying blade element angle of attack resulting from blade flapping, cyclic pitch inputs and wake inflow, the flow separation and stall ultimately occurs on a rotor in a very much more dynamic or time dependent manner. This stall phenomenon is, therefore, referred to as “dynamic stall”.

Dynamic stall will occur on any airfoil or other lifting surface when it is subjected to time dependent pitching, plunging or vertical translation or other type of non-steady motion that takes the effective angle of attack above its normal static stall angle. Under these circumstances, the physics of flow separation and the development of stall have been shown to be fundamentally different from the stall mechanism exhibited by the same airfoil under static quasi-steady conditions. Dynamic stall is in part distinguished by a delay in the onset of flow separation to a higher angle of attack than would occur statically.

This initial delay in stall onset is obviously advantageous as far as the performance and operational flight envelope of a helicopter is concerned. However, when dynamic flow separation does occur, it is found to be characterized by the shedding of a concentrated vertical disturbance from the leading edge region of the airfoil. As long as this vortex disturbance stays over the airfoil upper surface, it acts to enhance the lift being produced. Yet, the vortex flow patterns is not stable, and the vortex is quickly swept over the chord of the blade by the oncoming flow. This produces a rapid aft movement of the center of pressure, which results in large nose-down pitching moments on the blade section and an increase in torsional loads on the blades. This is the main characteristic of dynamic stall that concerns the rotor analyst, for which the effects have proved difficult to predict.

Nonlinearities in the airloads associated with dynamic stall can introduce further effects that give rise to dangerously high blade stresses, vibrations, and control loads. Because of the significant hysteresis in the airloads as functions of angle of attack that take place during dynamic stall, and also because of the possibilities of lower aerodynamic damping, an otherwise stable elastic blade mode can become unstable if flow separation is present. Therefore, the onset of dynamic stall generally defines the overall lifting, propulsive, and aeroelastic performance limits of an helicopter rotor.

The effects of unsteady motion on unsteady airfoil behavior and dynamic flow separation have been recognized for many years, mainly through studies of oscillating airfoils in wind tunnel tests. As mentioned previously, for an increasing angle of attack it has been observed that the flow remains attached to the upper surface of an airfoil to an angle of attack much higher than that could be attained quasi-statically, giving a corresponding increase in maximum lift. The delay in the onset of flow separation under unsteady conditions is a result of three primary unsteady phenomena. First, during the conditions where the angle of attack is increasing with respect to time, the unsteadiness of the flow resulting from circulation that is shed into the wake at the trailing edge of the airfoil causes a reduction in the lift and adverse pressure gradients compared to the steady case at the same angle of attack. Second, by virtue of a kinematic induced camber effect, a positive pitch rate further decreases the leading edge pressure and pressure gradients for a given value of lift. This can be considered a quasi-steady effect. Third, in

response to the external pressure gradients, there are also additional unsteady effects that occur within the boundary layer, including the existence of flow reversals in the absence of any significant flow separation. The onset of flow separation on airfoils is generally found to be delayed by unsteady effects such as those associated with increasing pitch rate. Coupled with the aforementioned pressure gradient reductions, the resulting lag in the formation of the boundary layer separation causes the onset of dynamic stall to be averted to a significantly higher angle of attack that would be obtained under quasi-steady conditions.

Ultimately, with increasing angle of attack, the high adverse pressure gradient that builds up near the leading edge under dynamic conditions causes flow separation to occur there. Experimental evidence suggests the formation of a free shear layer that forms just downstream of the leading edge which quickly rolls up and forms a vortical disturbance. This feature is now known to be a very characteristic aspect of dynamic stall. Not long after it is formed, this vortical disturbance leaves the leading edge region and begins to convect over the upper surface of the airfoil. This induces a pressure wave that sustains lift and produces airloads well in excess of those obtained under steady conditions at the same angle of attack."

Figure 2.1 shows typical static lift and dynamic curves for an aerofoil. The dynamic curve corresponds to an oscillatory motion in pitch.

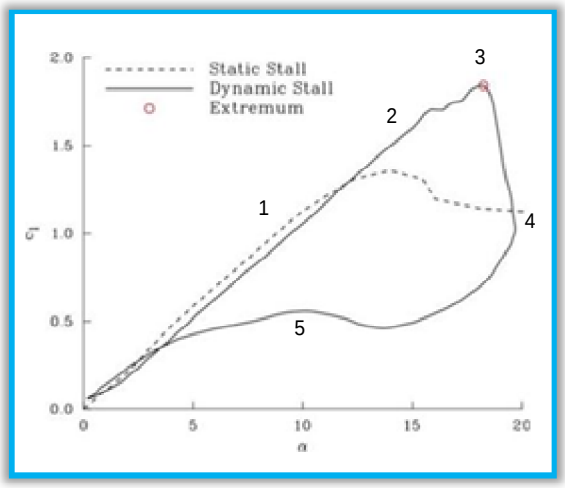

Figure 2.1: Static and dynamic lift curves.

Up to point 1, the behavior is linear and consistent with the unsteady linear thin-airfoil theory. If the angle of attack is increased (Point 2 in Figure 2.1), the linear behavior extends further than the angle of static stall. Flow reversal might be present between the points 1 and 2 and therefore the linear trend could not be considered exactly as linear behavior (Figure 2.2).

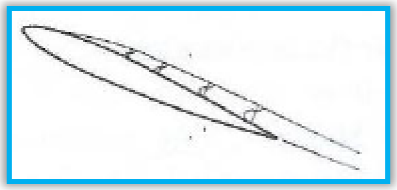

Figure 2.2: Airfoil exceeds static stall angle and flow reversal takes place in the boundary layer.

The additional lift depicted in the figure is due to a strong vortex (leading edge vortex, LEV) that forms and grows from the leading edge of the airfoil (Figure 2.3) and spread rearward. The presence of this vortex affects the pressure distribution and the total lift: it creates a low pressure zone that increases the lift. Its strength monotonically increases well past the aerofoil mid-chord. In some cases, primarily at low Mach numbers, the additional lift overshoots produced by this process may be between 50 and 100% higher than the static value of maximum lift. The LEV is also responsible for the differences in pitching moment from its previous trend to large negative values (Figure 2.7, Point 2), which result from an aft moving center of pressure as the vortex disturbance is swept downstream across the chord. The drag begins to rise dramatically (Figure 2.8, Point 2). However, until the vortex reaches the back of the profile, the lift does not collapse even though the flow separation zone increases (Figure 2.4).

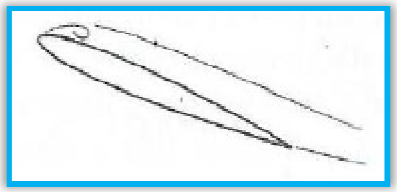

Figure 2.3: Flow separation at the leading edge.

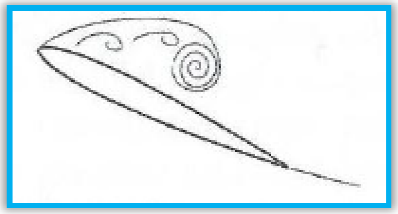

Figure 2.4: The leading edge vortex increases in strength and moves towards the trailing edge.

When the vortex reach the trailing edge, the maximum value in the cycle is obtained (Point 3) and then the lift drops dramatically. This drop of the lift coefficient occurs at a higher angle of attack than that for the divergence in the pitching moment; that is, the pitching moment break occurs at the onset of vortex shedding (Point 2 in Figure 2.7) whereas the lift break occurs when the vortex passes into the wake (Point 3 in Figure 2.1). The drag follow the same trend of the lift. After this point, the vortex detaches from the surface of the airfoil and it accompanies a sudden loss of lift (Point 4), a peak in the pressure drag (Point 3) and a maximum in the nose-down pitching moment (Point 3). Many secondary vortices could be obtained. These latter vortices are not as strong as the LEV so they are not able to generate as much lift. They could also be the cause of fluctuations in the lift curve (Figure 2.5).

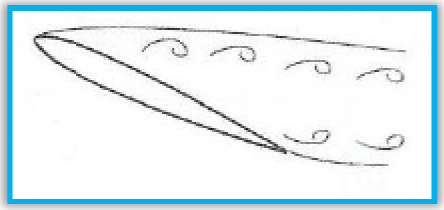

Figure 2.5: Lift stall. When the LEV reaches the trailing edge, the flow is fully separated.

The flow is now completely detached but, as the angle of attack is reduced, the flow gradually reattaches, eventually returning to its static value (Point 5). The angle of reattachment is lower than the initial angle of static stall. The result is a hysteresis loop in the lift, moment and drag curves. The lag in the reorganization of the flow is due to the reverse kinematic induced camber effect on the leading edge pressure gradient by the negative pitch rate. The resulting lift curve is asymmetrical (Figure 2.6).

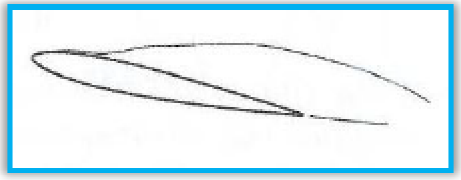

Figure 2.6: At lower angles of attack the flow reattaches front to back.

Figures 2.7 and 2.8 show the static and dynamic moment and drag curves, respectively.

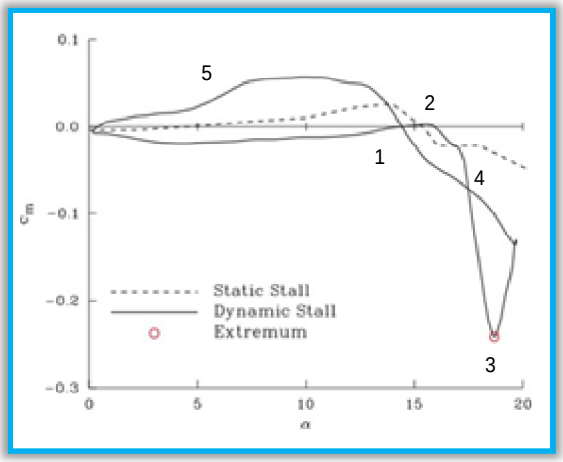

Figure 2.7: Static and dynamic moment curves.

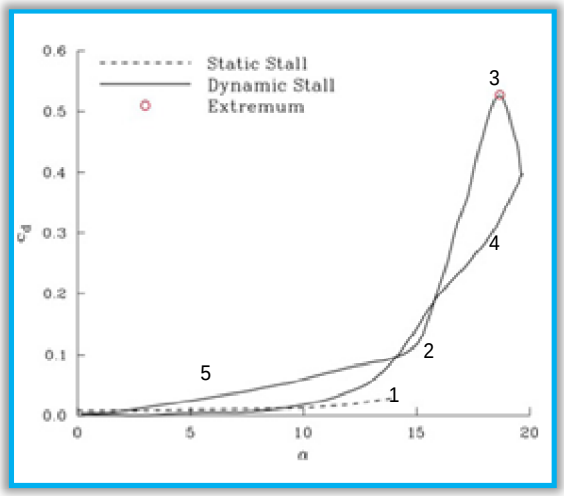

Figure 2.8: Static and dynamic drag curves.

All these phases increase greatly the complexity of the study of the dynamic stall phenomenon. Separation, transition to turbulent flow and final reattachment are really difficult to simulate. This is the reason why only semi-empirical models have been developed till now although numerous efforts are constantly carried out to obtain the best model possible.

Some features of the lift curve should be noted. First of all, for an oscillating airfoil, the maximum C_l in dynamic stall is delayed significantly compared to the static curve. On the other hand, when stall occurs, the drop in lift for the dynamic case is heavier and more persistent than in the case of the static one. Secondly, as the frequency of oscillation increases, the amount of hysteresis increases. For low frequencies of oscillation, the dynamic curve is similar to the static one, with a small hysteresis. However, at higher frequencies, the lift curve barely recovers the linear value before beginning another loop (Figure 2.9). In the steady case the aerodynamic forces are functions of the angle of attack α. In the unsteady case, the reduced frequency, $k = wb/u_0$, is another important parameter (see Chapter 9). An example of the effect of frequency on the lift curve is depicted in Figure 2.9 that clearly shows how the amplitude of the hysteresis loop increases with reduced frequency.

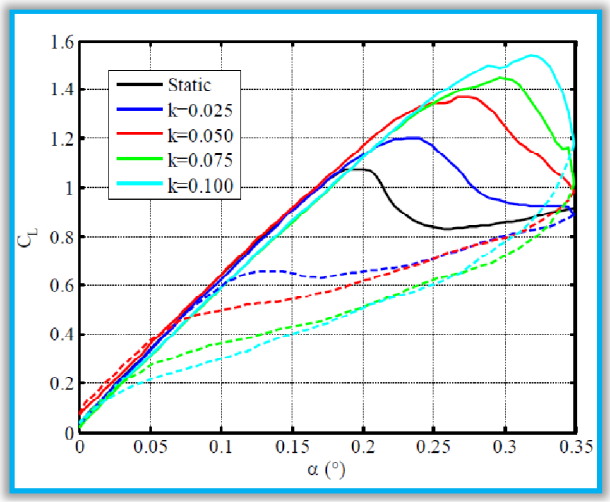

Figure 2.9: Lift coefficient for VR-12 airfoil with a reduced frequency k<0.1. Figure 4.2 from Reference [4] reprinted here for comparison.

3) ONERA MODEL THEORY

This section presents the ONERA model and verifies its capability and accuracy to predict the dynamic stall phenomenon for a NACA 0012 airfoil. The ONERA model theory used here is based on the work of D. Petot [1] and is implemented in a Matlab code developed by O. Celebi [2] (see Appendix G).

Several semi-empirical models have been proposed in the literature to quantify the effect of dynamic stall on airloads. Flow over airfoils in dynamic stall is highly non-linear and typically models are built through empirical corrections applied to steady data and are based on wind tunnel tests. The French aerospace research institute ONERA developed a model of dynamic stall [1]. The purpose of this chapter is to describe such a model (the original ONERA model), following Petot [1].

3.1) BASIS OF THE MODEL

The basic idea is that a non-linear system generally behaves linearly for small variations of its parameters. Nevertheless this rule has not general application, it has been demonstrated by experiments that, for unsteady stall, the lift and moment are linear for angle of attack variations of around 0.5 degrees. These variations are well described by a second-order transfer function that is valid only for small perturbations about the mean angle of attack considered. However, if the test is repeated over a wide range of mean angles, it is possible to obtain a global transfer function whose coefficients depend on the angle of attack. This is the procedure followed by ONERA to derive the mathematical model for dynamic stall. The results obtained confirm that this model is capable of providing reasonable correlation with experimental data as good as other more sophisticated models. Further, it provides a functional form for the parameters that seems to vary with ΔC_z^2 (where ΔC_z is the static residual, see Chapter 6.2). Reference [1] suggests a range of values for the parameters which can be used for the optimization.

The principle of modeling consists of finding a differential equation that correlates a generic aerodynamic coefficient C_q with changes, $\delta\theta$, of a control parameter of the system θ (angle of attack)

$$a\delta C_q + b\delta C_q' + c\delta C_q'' = d\delta\theta + e\delta\theta' + f\delta\theta'' \qquad (3.1)$$

such that it correctly expresses the transfer function measured.

This differential equation, is valid for any low amplitude variation around an average position θ_0. For this reason it is possible to write

$$a(\theta_0)\delta C_q + b(\theta_0)\delta C_q' + c(\theta_0)\delta C_q'' = d(\theta_0)\delta\theta + e(\theta_0)\delta\theta' + f(\theta_0)\delta\theta'' \qquad (3.2)$$

If the coefficients $a, b, \dots, e, f$ do not vary too rapidly with the average value θ_0 , then it is possible to apply the equation to a high amplitude variation of $\theta(t)$ with a negligible error, therefore we choose

$$\delta C_q = C_q - C_{qs} \qquad (3.3)$$

$$\delta\theta = \theta - \theta_0 \qquad (3.4)$$

where C_{qs} is the static value of C_q. Substituting θ for θ_0 yield the final form of the equation

$$a(\theta)C_q + b(\theta)C_q' + \cdots = a(\theta)C_{qs} + e(\theta)\theta' + \cdots \qquad (3.5)$$

This represents a model of the system as a differential equation which gives the response to any variation $\theta(t)$ of the test parameter. However, the movement $\theta(t)$ must not to be too rapid in order to take into account the hypothesis of small variations of the parameters.

3.2) APPLICATION TO DYNAMIC STALL OF AIRFOILS

Difficulties arise when the method is directly applied to dynamic stall because the domain of large angles of attack is strongly nonlinear; transition from unstalled to stalled state does not occur at a specific angle of attack. In general, a physical system may be modeled as transfer functions and their associated differential equations. ONERA assumed that in the linear regime the behavior of the airloads can be described by a first order transfer function while in the non linear one a second order transfer function is introduced. This is due to the time delay and overshoot due to the passing of shed vorticity. These assumptions, confirmed by extensive experimental correlations, lead up to the following system of differential equations

$$\begin{cases} Q = Q_1 + Q_2 \\ \dot{Q}_1 + \hat{\lambda}Q_1 = \hat{\lambda}Q_L + (\hat{\lambda}\hat{s} + \hat{\sigma})\dot{\theta} + \hat{s}\ddot{\theta} \\ \ddot{Q}_2 + \hat{a}\dot{Q}_2 + \hat{r}Q_2 = -(\hat{r}\Delta Q + \hat{e}\dot{Q}) \end{cases} \qquad (3.6)$$

where $\hat{\lambda}, \hat{s}, \hat{\sigma}, \hat{a}, \hat{r}, \hat{e}$ are semi-empirical coefficients of ONERA model (for more information about the values of these parameters, see reference [1]) and the load Q is expressed as a sum of two terms:

- Q_1, that represents the load in absence of stall. In the case of lift, the second equation in the system (3.6) must be a first-order differential while in the case of moment or drag it is an explicit expression

$$Q_1 = Q_L + (\hat{s} + \hat{\sigma})\dot{\theta} + \hat{s}\ddot{\theta} \qquad (3.7)$$

  It depends on Q_L which is the steady value of the aerodynamic coefficient in the absence of stall.

- Q_2 , that represents what must be added to Q_1 to obtain the total load (Q_2 is the load due to dynamic stall). The variable $\Delta Q = Q_L - Q_s$ determines the entrance and exit from the stalled region.

  These equations are written in terms of reduced time parameter

$$\tau = \frac{Ut}{b} \qquad (3.8)$$

where U is the free stream velocity, b the semi-chord and t the time.

Moreover, as mentioned in Chapter 2, high amplitude tests show that effective stalling occurred at higher angles of attack than during static testing and this delay in stalling is constant when expressed in reduced time.

Although the form of $\hat{r}, \hat{a}$ and $\hat{e}$ is not known, it is found that these parameters of the equations fit the data remarkably well if they are expressed as

$$\sqrt{\hat{r}} = r_0 + r_2 \Delta C_z^2 \qquad (3.9)$$

$$\hat{a} = a_0 + a_2 \Delta C_z^2 \qquad (3.10)$$

$$\hat{e} = e_2 \Delta C_z^2 \qquad (3.11)$$

where ΔC_z is the measure of stall given by the difference between the linear static aerodynamic coefficient extrapolated to the stalled domain and its real value measured at the angle of attack considered (Figure 3.1).

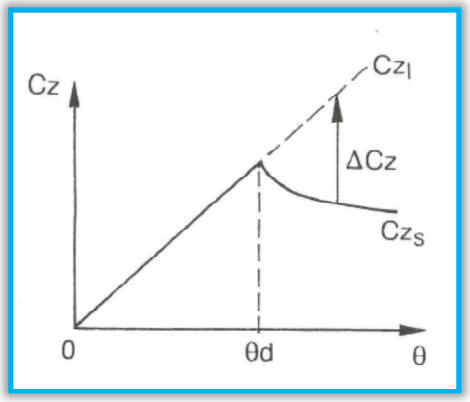

Figure 3.1: Definition of ΔC_z.

This choice of equations and the choice of the maximum order of the differentials led to results in remarkable agreement with the experiment.

The equation in Q_1 must often be completed by a corrective term in ΔC_z given by

$$\hat{\sigma} = \sigma_0 + \sigma_1 |\Delta C_z| \qquad (3.12)$$

The inclusion of this term (that vanishes at low angle of attack) in an equation designed for linear loading is required by the tests done by ONERA to match the results with experimental data.

The above model was extended following the ideas of Peters [20]. He remarked that the equations could be written in many forms and that the variable used in aerodynamic theories is not the lift coefficient but the circulation. Therefore he rewrote the differential equations in terms of circulation. We will see later in Chapter 5.2 how this can be used to extend the ONERA model to flexible airfoils.

3.3) MODIFIED ONERA MODEL BY LAXMAN AND VENKATESAN

Laxman & Venkatesan [21] modified the ONERA model by incorporating a second-order approximation of Theodorsen's lift deficiency function $C(k)$ (see Appendix E). The total lift expression derived from Theodorsen and Garrick aerodynamic theory is given by equation *(E.39)*, re-written here for clarity (see Appendix E for more details)

$$L = L_{NC} + L_C = -\pi\rho b^2\left[U\dot{\alpha} + \ddot{h} - \frac{b^2}{8}\ddot{k}_1\right] - 2\pi\rho UbQC(k)$$
$$= -\pi\rho b^2\left[U\dot{\alpha} + \ddot{h} - \frac{b^2}{8}\ddot{k}_1\right]$$
$$- 2\pi\rho UbC(k)\left(U\alpha + \dot{h} + \frac{b}{2}\dot{\alpha} + \frac{Ub}{2}k_1 + \frac{Ub^2}{8}k_2\right.$$
$$\left. + \frac{Ub^3}{48}k_3\right) \qquad (3.13)$$

where ρ is the density, $\dot{\alpha}$ and $\dot{h}$ are the time derivative of the pitch and plunge variables respectively and k_1, k_2, k_3 are the curvature variables.

The only difference between the original ONERA model and the modified one is given by Theodorsen's function $C(k)$ that is replaced here with a second order approximation in the form of:

$$C(k) \cong \frac{A_1\left(\frac{iwb}{U}\right)^2 + A_2\left(\frac{iwb}{U}\right)^2 + A_3}{\left(\frac{iwb}{U}\right)^2 + B_2\left(\frac{iwb}{U}\right)^2 + B_3} \qquad (3.14)$$

whit $A_1 = 0.50$, $A_2 = 0.393$, $A_3 = 0.0439425$, $B_2 = 0.5515$ and $B_3 = 0.0439075$. U is the free stream velocity, w the excitation frequency and i the complex variable. Comparing the second order approximation with the first order approximation of the original ONERA model and the exact Theodorsen function $C(k)$ one can see that the second order approximation provides a better agreement (Figure 3.2).

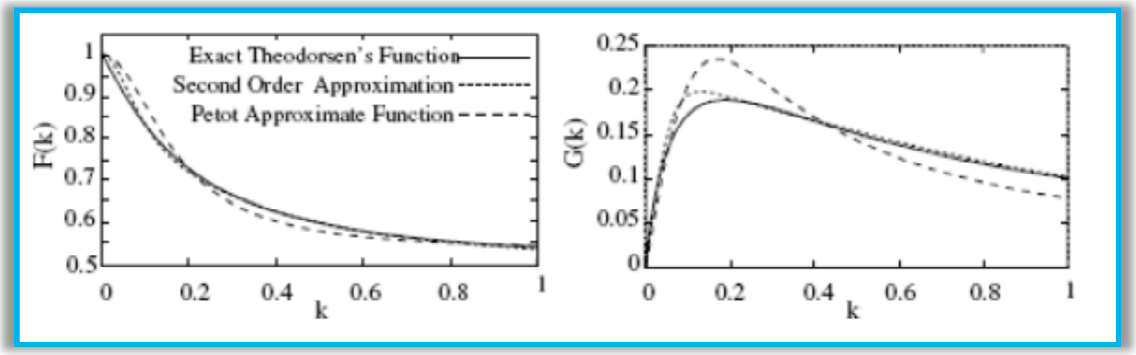

Figure 3.2: Comparison among different approximation of Theodorsen function. Source of the figure: Reference [2].

4) VERIFICATION AND VALIDATION OF ONERA MODEL

A MATLAB code [2] has been written to validate the ONERA model. The outputs of the code are the lift, moment and drag forces, that can be plotted as function of the pitch angle (Appendix G). From these aerodynamic forces is possible to obtain the lift, moment and drag coefficients, that are more interesting. To validate the code, the results will be compared with experimental data by McCroskey [9] for an oscillating airfoil.

The forced oscillation is of the form

$$\theta(t) = \theta_m + \theta_a \sin(w_\theta t) = \theta_m + \theta_a \sin(k\tau) \qquad (4.1)$$

where θ_m is the mean angle of attack of the airfoil, θ_a is the amplitude of the oscillation, k is the reduced frequency and τ the reduced time.

Three cases are considered, with all the same parameters except θ_m that assumes three different values: 5°, 10° and 15°. It is therefore possible to obtain the following form of the forced oscillation

$$\theta(t) = 5° + 10° \sin(0.1\tau)$$

$$\theta(t) = 10° + 10° \sin(0.1\tau) \qquad \theta(t) = 15° + 10° \sin(0.1\tau)$$

(4.2)

Figures 4.1, 4.2 and 4.3 show a comparison of predicted and experimental results of C_z, C_m and C_d for $\theta_m = 5, 10, 15°$ respectively.

(a)

(b)

(c)

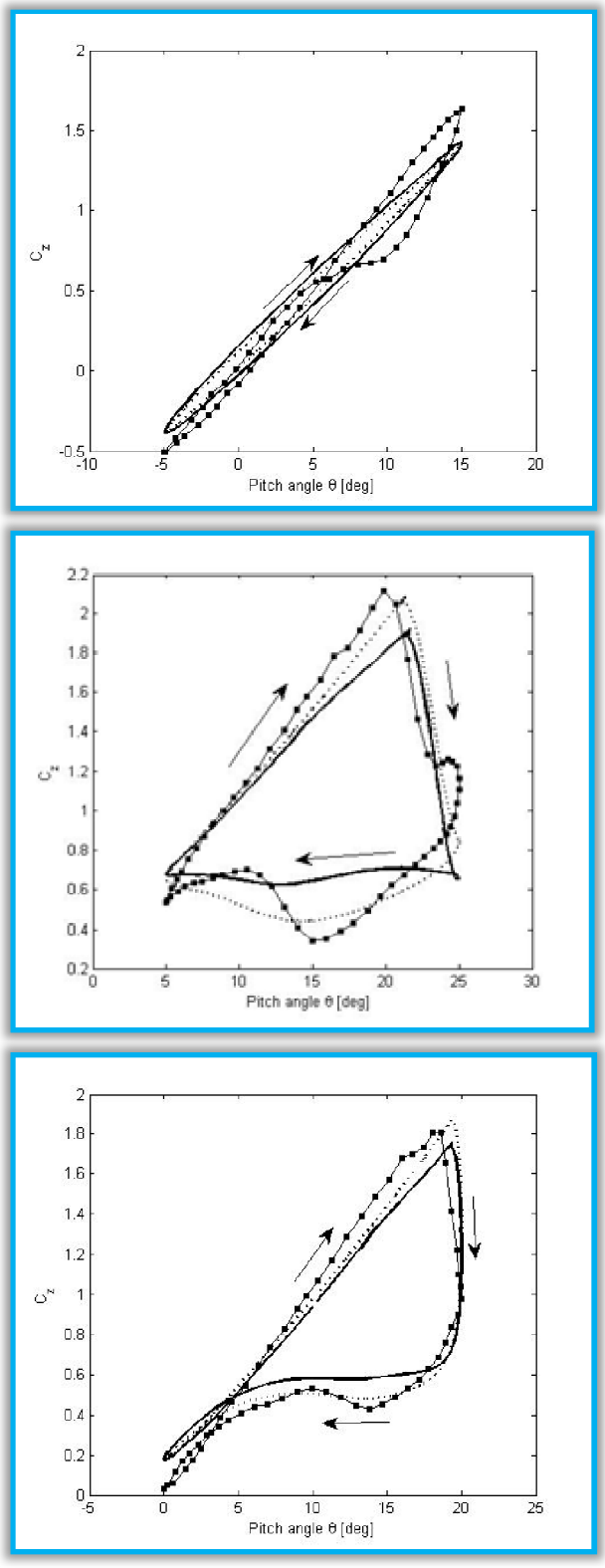

Figure 4.1: Variation of the lift coefficient as a function of the pitch angle. (a) $\theta_m = 5°$, (b) $\theta_m = 10°$, (c) $\theta_m = 15°$.

(a)

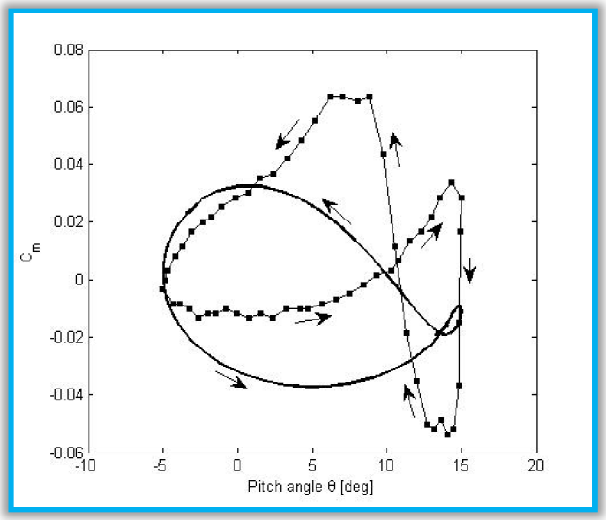

(b)

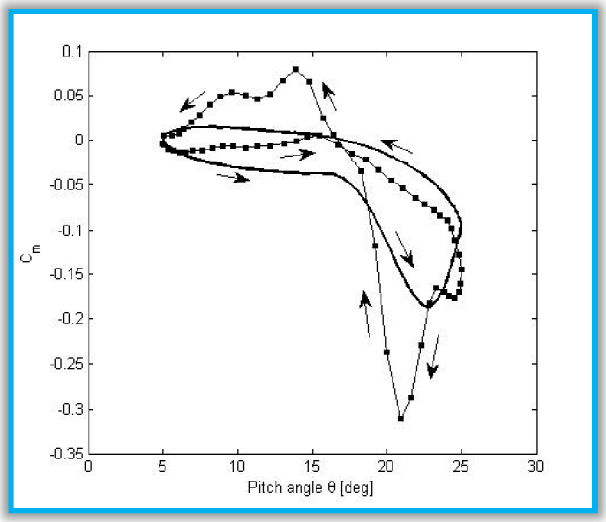

(c)

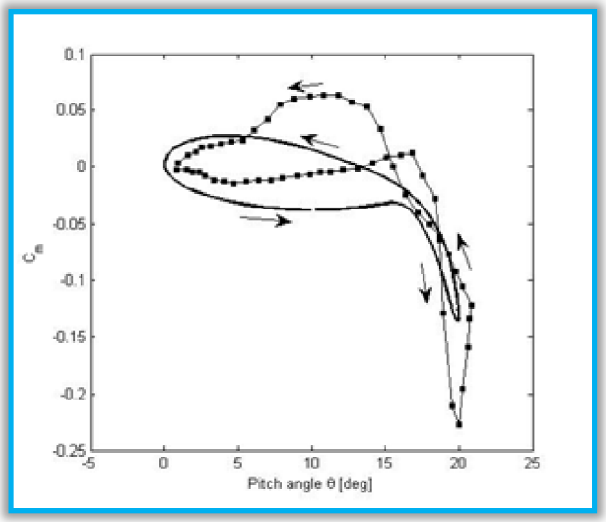

Figure 4.2: Variation of the moment coefficient as a function of the pitch angle. (a) $\theta_m = 5°$, (b) $\theta_m = 10°$, (c) $\theta_m = 15°$.

(a)

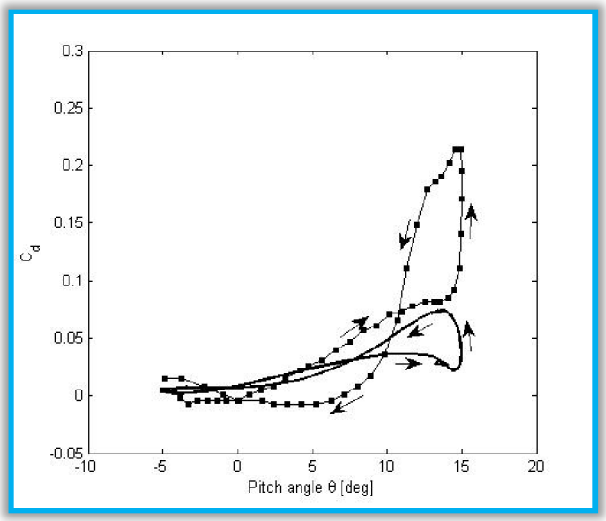

(b)

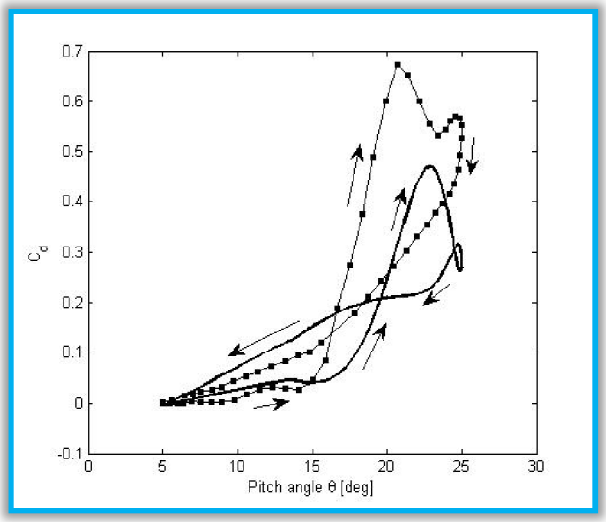

(c)

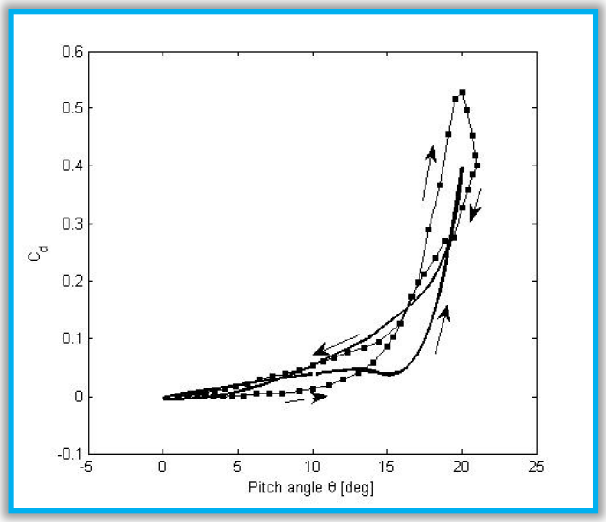

Figure 4.3: Variation of the drag coefficient as a function of the pitch angle. (a) $\theta_m = 5°$, (b) $\theta_m = 10°$, (c) $\theta_m = 15°$.

The arrows indicate the hysteresis and the black line with the square marks represent the experimental data.

As it can be seen, the original model (the black line) shows a good correlation with the experimental data, especially for the lift coefficient that is considered the most important one. It denotes less agreement when it is used to calculate the moment and drag coefficients. The modified model by Laxman and Venkatesan [21] (the dotted line in lift plots) provides good results particularly in the region of reattachment of the flow but this result is obtained with a higher computational cost.

The correlation with experimental data can be increased by conducting an optimization of the empirical coefficients of the model. This could be the subject of future work.

5) JOHNSON/PETERS FLEXIBLE AIRLOAD THEORY

This section concerns Johnson/Peters flexible airloads theory. The theory is selected to investigate the dynamic stall phenomenon and is implemented in a MATLAB code. The results obtained are then compared with Theodorsen [14] and Garrick [15] theory (see Appendix E for more details).

The Johnson/Peters theory is a general linear aerodynamic theory for flexible airfoils. The geometry of the deformed airfoil is accomplished through the use of Chebyshev polynomials. The first three polynomials correspond to plunge, pitch and camber motions about the mid-chord respectively. Therefore, the first two polynomials can be used to take into account the rigid body motion and the rest of the infinite series of polynomials can be used for the deformations. The use of these polynomials guarantees a natural coordinate system for airfoil motions. Peters developed a finite-state aerodynamic model via expansions in a Glauert series which is based on a two-dimensional potential flow, with the non-penetration boundary condition applied on the airfoil and the Kutta condition applied at the trailing edge. The theory can be coupled with any two or three dimensional induced-flow model and therefore it can be applied into rotorcraft aerodynamic analysis tools.

Theodorsen and Garrick theory is used here for comparison with Peters theory (for more information regarding this theory, see Appendix E). In order to make such a comparison, the Chebyshev polynomials are used also for this theory. Theodorsen used two dimensional elementary flows to develop the flow around a flat plate with a flap undergoing pitch and plunge motions [14]. This flow was modeled using the Joukowski conformal transformation, that maps the flow around a circle to a flow around a flat plate. The boundary condition was satisfied by using source/sink distribution for the airfoil whereas vortices were used for the wake model. Bernoulli's equation was finally used to obtain the airloads. Theodorsen considered small perturbations and harmonic motions. These assumptions allowed the creation of a vortex sheet for the wake (Appendix F) which extend from the trailing edge to infinity and, more important, they permit the integration of the sheet leading to a solution in the form of Bessel functions. In this way, Theodorsen was able to show that the lift due to the circulation (i.e. the lift due to the wake) was a function of the reduced frequency. Garrick [15] extended Theodorsen

theory to develop the thrust force generated by a flat plate in unsteady flow. Following the work of W. P. Walker [16] this theory is also applied to deformable airfoils.

The solution is obtained by representing the aerofoil and its wake (both assumed to be straight) by a distribution of vorticity per unit length. The derivation of the Johnson/Peters flexible airloads theory from first principles is presented here, following reference [18]. Consider a thin-airfoil of arbitrary shape and length equal to $2b$ (where b is the length of the semi-chord) moving through a mass of still air (Figure 5.1). The coordinate system is centered at the mid-chord so that $-b \leq x \leq +b$ with the x-axis as horizontal axis (positive on the right) and the y-axis as vertical axis (positive down). The coordinate system is moving with arbitrary motion described by a horizontal velocity u_0, a vertical velocity v_0 and a rotation v_1. The velocities are constant in modulus and depends on Mach number and air speed. The deformations of the airfoil are considered to be small, $h \ll b$, $\partial h/\partial x \ll 1$ and $\partial h/\partial t \ll u_0$ where with h is denoted the airfoil shape. The bound circulation per unit length is given by γ_b while the wake circulation per unit length is γ_w and is shed along the x-axis. The wake is considered flat for simplicity (Appendix F).

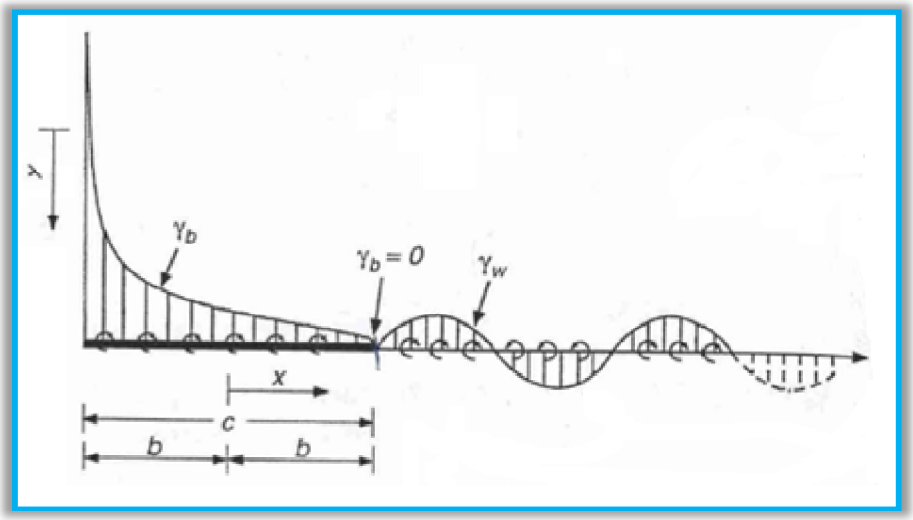

Figure 5.1: Thin airfoil of arbitrary shape and its associated coordinate system. Source of the figure: Reference [5].

As in the case of thin-airfoil theory, the system is constrained by the non-penetration boundary condition at the airfoil surface. This condition could be expressed as:

$$w = \bar{v} + \lambda = u_0 \frac{\partial h}{\partial x} + \frac{\partial h}{\partial t} + v_0 + v_1 \frac{x}{b} \qquad (5.1)$$

where w is the total induced flow, $\bar{v}$ is the induced flow from bound circulation and λ is the induced flow from shed circulation. The first two terms on the right side are the result of the shape of the airfoil mean-line whereas the second two terms originate from the frame motion. The equation represents both static and dynamic shape changes and this is why it could be applied to morphing airfoils.

From the Biot-Savart law, the induced flow may be expressed in terms of circulation per unit length over the interval $-b \leq x \leq +b$ corresponding to the airfoil surface. Thus we obtain

$$\bar{v} = -\frac{1}{2\pi} \int_{-b}^{+b} \frac{\gamma_b(\xi, t)}{x - \xi} d\xi \qquad (5.2)$$

$$\lambda = -\frac{1}{2\pi} \int_{+b}^{\infty} \frac{\gamma_w(\xi, t)}{x - \xi} d\xi \qquad (5.3)$$

where ξ is the variable of integration. From the vorticity equation, the loading due to the circulation is

$$\Delta P(x,t) = \rho u_0 \gamma_b + \rho \int_{-b}^{x} \frac{\partial \gamma_b(\xi, t)}{\partial t} d\xi \qquad -b \leq x \leq +b \qquad (5.4)$$

The loading across the shed wake must be zero therefore

$$0 = u_0 \gamma_w + \frac{d\Gamma}{dt} + \int_{b}^{x} \frac{\partial \gamma_w}{\partial t} d\xi \qquad b < x \qquad (5.5)$$

where Γ is the total bound circulation on the airfoil given by

$$\Gamma = \int_{-b}^{+b} \gamma_b dx \qquad (5.6)$$

The solution of equation (5.5) implies that circulation is shed into the air mass and maintains its strength at that point in space as the airfoil moves on (Appendix F). A corollary of this result is that the spatial gradient of induced flow due to the shed wake is related to the temporal gradient of the induced flow

$$\frac{\partial \lambda}{\partial t} + u_0 \frac{\partial \lambda}{\partial x} = \frac{1}{2\pi} \frac{d\Gamma/dt}{b - x} \qquad (5.7)$$

Now these equations $(5.1, 5.2, 5.4, 5.7)$ represent the airloads theory and must be transformed in order to derive a general formulation that does not depend on the coordinate system. In order to do this, all the variables are expressed as expansions with respect to the Glauert variable φ, represented by the change in variable

$$x = b\cos\varphi \qquad -b \le x \le +b, \qquad 0 \le \varphi \le \pi \qquad (5.8)$$

The expansions for the circulation and the loading (Reference [4]) are defined as

$$\gamma_b = 2\left[\frac{+\gamma_s}{\sin(\varphi)} - \frac{\gamma_0\cos(\varphi)}{\sin(\varphi)} + \sum_{n=1}^{\infty}\gamma_n\sin(n\varphi)\right] \qquad (5.9)$$

and

$$\Delta P = 2\rho\left[\frac{+\tau_s}{\sin(\varphi)} - \frac{\tau_0\cos(\varphi)}{\sin(\varphi)} + \sum_{n=1}^{\infty}\tau_n\sin(\varphi)\right] \qquad (5.10)$$

where the first two terms of each expansion (γ_s, γ_0, τ_s and τ_0) are the singular potential functions that allow suction peaks at either end of the airfoil. The γ_n coefficients are the components of velocity due to bound circulation whereas the τ_n coefficients are simply the expansion coefficients for ΔP.

The airfoil deformation, the total velocity and the induced flow can be transformed with the Glauert variable as

$$h = \sum_{n=0}^{\infty} h_n\cos(n\varphi) \qquad (5.11)$$

$$w = \sum_{n=0}^{\infty} w_n\cos(n\varphi) \qquad (5.12)$$

$$\lambda = \sum_{n=0}^{\infty} \lambda_n\cos(n\varphi) \qquad (5.13)$$

where h_n, w_n, and λ_n are the components of the generalized airfoil deformation, of the total velocity field and of the velocity due to the shed wake, respectively. The $cos(n\varphi)$ terms are equivalent to Chebyshev polynomials and represent the shape functions of the system. The first three terms correspond to plunge, pitch and camber deformation respectively. For $n = 0$, we have

$$\cos(n\varphi) = \cos(0\varphi) = 1 \qquad (5.14)$$

which represents a plunge motion (Figure 5.2)

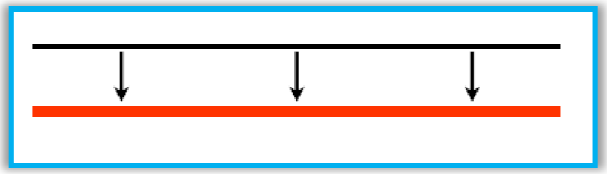

Figure 5.2: Plunge motion.

For $n = 1$, we have

$$\cos(n\varphi) = \cos(1\varphi) = \frac{x}{b} \qquad (5.15)$$

i.e. a pitch motion (Figure 5.3)

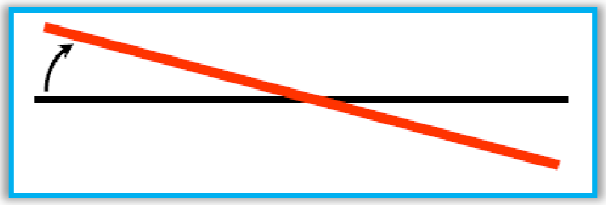

Figure 5.3: Pitch motion.

Finally, for $n = 2$ we have

$$\cos(2\varphi) = 2\cos^2(\varphi) - 1 = 2\left(\frac{x}{b}\right)^2 - 1 \qquad (5.16)$$

that corresponds to a camber deformation (Figure 5.4) with fixed points at $\frac{x}{b} = \pm\sqrt{\frac{1}{2}}$.

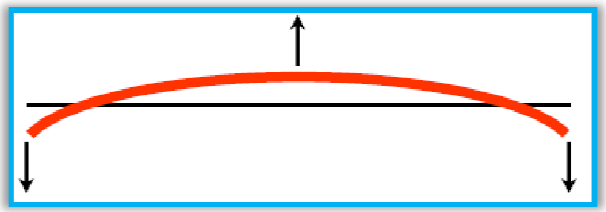

Figure 5.4: Camber deformation.

It is possible to obtain a general form of the loads first by using the Glauert transformation (equation 5.8) and secondly by expressing them entirely in terms of w_n and λ_0. From equation (5.1) we have

$$\bar{v} = w - \lambda \qquad (5.17)$$

Then, substituting the expansion of the total velocity (equation 5.12) and recalling the expression of $\bar{v}$ (5.2) it is possible to obtain an expression in terms of γ_b, w_n and λ. The final step consist of substituting the expansion in equation (5.13) for the induced flow λ and the expansion for the circulation γ_b in equation (5.9). The final result is an expression in terms of γ_n, w_n and λ_n which substituted into equation (5.10) leads to

$$\tau_0 = u_0(w_0 - \lambda_0) \qquad (5.18)$$

$$\tau_1 = u_0 w_1 + b\left(\dot{w}_0 - \frac{1}{2}\dot{w}_2\right) \qquad (5.19)$$

$$\tau_n = u_0 w_n + \frac{b}{2n}(\dot{w}_{n-1} - \dot{w}_{n+1}) \qquad n > 2 \qquad (5.20)$$

where $\dot{w}_n$ are the components of the total acceleration.

The generalized loads are obtained from the integration of ΔP

$$L_n = \int_{-b}^{+b} \Delta P \cos(n\varphi)\, dx = -\int_{0}^{\pi} (b\Delta P \cos(n\varphi) \sin\varphi)\, d\varphi \qquad (5.21)$$

Using (5.10) and carrying out the integration we get

$$L_0 = -2\pi\rho b f u_0(w_0 - \lambda_0) - \pi\rho b u_0 w_1 - \pi\rho b^2\left(\dot{w}_0 - \frac{1}{2}\dot{w}_2\right)$$

$$L_1 = \pi\rho b u_0(w_0 - \lambda_0) - \frac{1}{2}\pi\rho b u_0 w_2 - \frac{1}{8}\pi\rho b^2(\dot{w}_1 - \dot{w}_3)$$

$$L_2 = \frac{1}{2}\pi\rho b u_0(w_1 - w_3) + \frac{1}{2}\pi\rho b^2\left(\dot{w}_0 - \frac{1}{2}\dot{w}_2\right) - \frac{1}{12}\pi\rho b^2(\dot{w}_2 - \dot{w}_4)$$

$$L_n = \frac{1}{2}\pi\rho b u_0(w_{n-1} - w_{n+1}) + \frac{1}{4(n-1)}\pi\rho b^2(\dot{w}_{n-2} - \dot{w}_n) - \frac{1}{4(n+1)}\pi\rho b^2(\dot{w}_n - \dot{w}_{n+2}) \qquad n \geq 3$$

(5.22)

These loads correspond to the virtual work of each shape function. L_0 is a uniform force acting in the negative *y* direction and thus it can be assumed as the forcing of the plunge motion whereas L_1 is a linear force distribution that can be associated to the pitch moment. λ_0 is a component of the induced flow velocity.

The terms w_i (with $i = 0, \dots, n$) can be obtained from the airfoil as

$$w_0 = v_0 + \dot{h}_0 + u_0 \sum_{n=1,3,5,\dots}^{\infty} n h_n / b \qquad (5.23)$$

$$w_1 = v_1 + \dot{h}_1 + 2u_0 \sum_{n=2,4,6,\dots}^{\infty} n h_n / b \qquad (5.24)$$

$$w_m = \dot{h}_m + 2u_0 \sum_{n=m+1,m+3,\dots}^{\infty} n h_n / b \qquad m \geq 2 \qquad (5.25)$$

Substituting equation (5.9) into equation (5.6) and resolving the integral it is possible to obtain

$$\Gamma = 2\pi b\left(\gamma_s + \frac{\gamma_1}{2}\right) \qquad (5.26)$$

and from this it is possible to obtain the total bound circulation in terms of w_n and λ_n as

$$\Gamma = 2\pi b\left[w_0 - \lambda_0 + \frac{1}{2}w_1 - \frac{1}{2}\lambda_1\right] \qquad (5.27)$$

Considering that the local lift is always perpendicular to the local deformed airfoil surface, the drag force is given by

$$D = \int_0^{\pi}\left(b\Delta P\frac{\partial h}{\partial x}\sin\varphi\right)d\varphi - 2\pi\rho b(w_0 - \lambda_0)^2 \qquad (5.28)$$

In compact matrix form, all these equations can be written as

$$\frac{1}{2\pi\rho}\{L_n\} = -b^2[M]\{\ddot{h}_n + \dot{v}_n\} - bu_0[C]\{\dot{h}_n + v_n - \lambda_0\} - {u_0}^2[K]\{h_n\} - b[G]\{\dot{u_0}h_n - u_0v_n + u_0\lambda_0\} \tag{5.29}$$

$$\frac{1}{2\pi}\{\Gamma_n\} = b\{1\}^T[C - G]\{\dot{h}_n + v_n - \lambda_1\} + u_0\{1\}^T[K]\{h_n\} \tag{5.30}$$

$$\frac{1}{2\pi\rho}\{D_n\} = -b\{\dot{h}_n + v_n - \lambda_0\}^T[S]\{\dot{h}_n + v_n - \lambda_0\} + b\{\ddot{h}_n + \dot{v}_n\}^T[G]\{h_n\} - u_0\{\dot{h}_n + v_n - \lambda_0\}^T[K - H]\{h_n\} + \{\dot{u_0}h_n - u_0v_n + u_0\lambda_0\}^T[H]\{h_n\} \tag{5.31}$$

All the matrices [ ] and vectors { } are define in Appendix A.

5.1) TWO-DIMENSIONAL DYNAMIC INDUCED FLOW MODEL

The airloads theory requires the knowledge of the λ_0 component of the induced flow (inflow). The amount of decrease in the total circulation $\Gamma(t)$ is equal to the amount of vorticity shed from the trailing edge. The expansion of the relationship between the spatial gradient of the induced flow due to the shed wake and the temporal gradient of the induced flow (equation 5.7 in the previous Chapter)

$$\frac{\partial\lambda}{\partial t} + u_0\frac{\partial\lambda}{\partial x} = \frac{1}{2\pi}\frac{d\Gamma/dt}{b - x} \tag{5.32}$$

leads to the differential equation for the generalized inflow

$$b\left(\dot{\lambda_0} - \frac{1}{2}\dot{\lambda}_2\right) + u_0\lambda_1 = \frac{\dot{\Gamma}}{\pi} \tag{5.33}$$

$$\frac{b}{2n}\left(\dot{\lambda}_{n-1} - \dot{\lambda}_{n+1}\right) + u_0\lambda_n = \frac{\dot{\Gamma}}{n\pi} \qquad n \geq 2 \tag{5.34}$$

This is a system of N differential equations in $N + 1$ coefficients $\lambda_0, \dots, \lambda_N$ that is valid for any wake geometry (Appendix F). $\dot{\lambda}_n$ are the accelerations due to the shed wake while N is the number of induced flow states considered. Reference [13] shows that a good approximation of Theodorsen's results is obtainable with $N = 8$. A flat wake model is

implemented here (see Appendix F for more details) and λ_0 can be approximated by

$$\lambda_0 = \frac{1}{2}\sum_{n=1}^{N} b_n \lambda_n \qquad (5.35)$$

with

$$b_n = (-1)^{n-1}\frac{(N+n-1)!}{(N-n-1)!\,(n!)^2} \qquad n = 1,2,3,\dots,N-1 \qquad (5.36)$$

$$b_N = (-1)^{N+1} \qquad (5.37)$$

The coefficients should also satisfy the constraint

$$\sum_{n=1}^{N} b_n = 1 \qquad (5.38)$$

It is now possible to obtain the following differential equation for Γ by the derivative of the expression of the total bound circulation (equation 5.27) and the substitutions of the terms above (equations 5.35, 5.36 and 5.37)

$$\dot{\Gamma} = 2\pi b\left[\left(\dot{w}_0 - \frac{1}{2}\{b\}^T\{\dot{\lambda}\}\right) + \frac{\dot{w}_1 - \dot{\lambda}_1}{2}\right] + \dot{\Gamma}_{n2} \qquad (5.39)$$

where $\dot{\Gamma}_{n2}$ is the variation in total bound circulation due to stall. The presence of this term will be explained later in Chapter 5.2. Substitution of this result into the differential equations for the generalized inflow (5.33 – 5.34) gives

$$\frac{1}{2}\{b\}^T\{\dot{\lambda}\} + \dot{\lambda}_1 - \frac{1}{2}\dot{\lambda}_2 = 2\left(\dot{w}_0 + \frac{1}{2}\dot{w}_1\right) + \frac{1}{b\pi}\dot{\Gamma}_{n2} - \frac{u_0}{b}\lambda_1 \qquad n = 1$$

(5.40)

$$\frac{1}{2}\{b\}^T\{\dot{\lambda}\} + \frac{3}{4}\dot{\lambda}_1 - \frac{1}{4}\dot{\lambda}_3 = 2\left(\dot{w}_0 + \frac{1}{2}\dot{w}_1\right) + \frac{1}{2b\pi}\dot{\Gamma}_{n2} - \frac{u_0}{b}\lambda_2 \qquad n = 2$$

(5.41)

$$\frac{1}{n}\{b\}^T\{\dot{\lambda}\} + \frac{1}{n}\dot{\lambda}_1 - \frac{1}{2n}\dot{\lambda}_{n+1} = \frac{2}{n}\left(\dot{w}_0 + \frac{1}{2}\dot{w}_1\right) + \frac{1}{nb\pi}\dot{\Gamma}_{n2} - \frac{u_0}{b}\lambda_n \qquad n \geq 3$$

(5.42)

that can be rewritten in matrix form as follows

$$[A]\{\dot{\lambda}\} = \{c\}\left(\dot{w}_0 + \frac{1}{2}\dot{w}_1\right) + \frac{1}{2b\pi}\dot{\Gamma}_{n2} - \frac{u_0}{b}\{\lambda\} \qquad (5.43)$$

The matrices and vectors are defined in Appendix A. The total velocity vector $\{w\}$ can be expanded in function of the airfoil motions $\dot{h}_n$ (velocities) and $\ddot{h}_n$ (accelerations) and the free stream accelerations $\dot{v}_n$. The result is

$$\{\dot{\lambda}\} = [A]^{-1}\left[\{c\}\left(\{e\}^T\{\dot{v}_n + \ddot{h}_n\} + \frac{u_0}{b}\{f\}^T\{\dot{h}_n\} + \frac{1}{2b\pi}\dot{\Gamma}_{n2}\right) - \frac{u_0}{b}\{\lambda\}\right] \qquad (5.44)$$

5.2) DYNAMIC STALL MODEL: ONERA MODEL

Now that the equations of the airloads and the inflow model are set, the only thing that remains to do is to define the dynamic stall model. The model used herein is the ONERA model, which has been presented in Chapter 3.

As discussed in Chapter 2, up to a certain static stall angle α_{ss} (which is characteristic of every airfoil and depends on the Reinolds' number), the airfoil behaves linearly. After that point the airfoil begins to stall and its behavior cannot be considered longer linear: there is a deficiency between the projection of the linear lift and the real lift. That difference, denoted with ΔC_l, is the static loss of lift that drives ONERA differential equations (static stall residual). The evaluation of this deficiency is the focal point of the theory, because it is the forcing function which guides the dynamic stall. In general, we will require to define a static loss ΔC_n, for each of the airloads C_n considered.

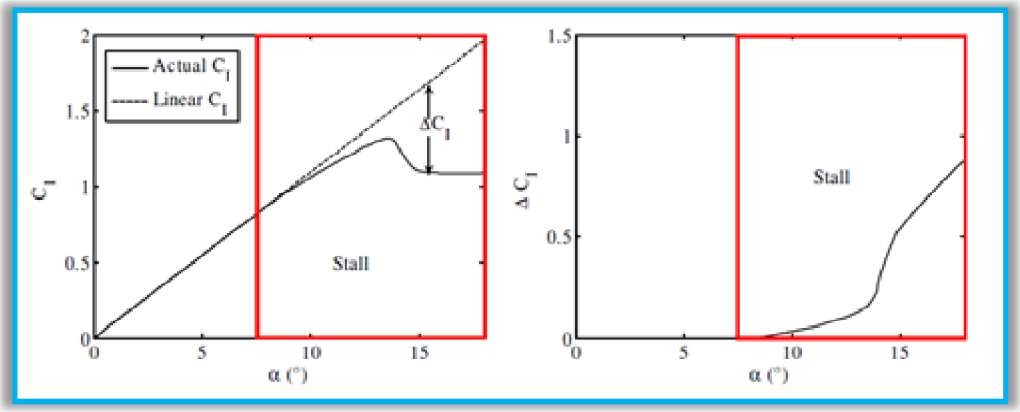

Figure 5.5: Lift residual. Source of the figure: Reference [4].

As explained before, the ONERA model is based on two differential equations: the first one is a first-order transfer function used to calculate the linear lift coefficient. This equation describes the linear regime below α_{ss} as

$$\dot{\Gamma}_{n1} + \hat{\lambda}\Gamma_{n1} = \hat{\lambda}\hat{a}\theta + \left(\hat{\lambda}\hat{s} + \hat{\sigma}\right)\dot{\theta} + \hat{s}\ddot{\theta} \qquad (5.45)$$

where here $\hat{\lambda}, \hat{a}, \hat{s}, \hat{\sigma}$ are empirical coefficients and θ is the angle of attack.

The second one is a second-order transfer function that describes the stalled regime, where the airloads display a time delay and overshoot due to the shed vorticity. This function evaluates the loss of lift due to dynamic stall as

$$\frac{b^2}{U}\ddot{\Gamma}_{n2} + \hat{\eta}\frac{b}{U}\dot{\Gamma}_{n2} + \hat{\omega}^2\Gamma_{n2} = -bu\hat{\omega}^2\left[\Delta C_l + \hat{\epsilon}\frac{d\Delta C_l}{dt}\frac{b}{U}\right] \qquad (5.46)$$

where $\hat{\omega}, \hat{\eta}$ and $\hat{\epsilon}$ are stall coefficients derived from a series of small-amplitude tests as explained after-written.

The results are finally combined to give the total lift coefficient

$$C_l = \frac{\Gamma_{n1}}{(Ub)} + \frac{\Gamma_{n2}}{(Ub)} = C_{l\,(l)} + \frac{\Gamma_{n2}}{(Ub)} \qquad (5.47)$$

where $C_{l\,(l)}$ is the linear part of the static stall curve.

Equations $(5.45 - 5.46)$ can be written both as functions of the lift or of the lift coefficient but studies confirmed that the best match with experimental data are obtained when the equations are expressed in terms of circulation. This is somewhat obvious as dynamic stall is due to a loss of circulation for the presence of the vortices shed at the leading edge.

These differential equations have time-varying coefficients that in turn depend on a dynamic variations of the angle of attack. ONERA identifies these parameters by dynamic perturbations considering some mean angles of attack. The assumption made is that the coefficients varies sufficiently slowly to allow the perturbation results to define the coefficients. If these stall parameters are identified in such a way, it is possible to obtain good agreement with experimental data. Both ONERA and NASA executed a series of small-amplitude tests to determine the stall parameters (References [26] and [27]). The tests have provided the following form for the stall coefficients:

$$\begin{cases} \hat{\omega} = \omega_0 + \omega_1 \Delta C_l{}^2 \\ \hat{\eta} = \eta_0 + \eta_1 \Delta C_l{}^2 \\ \hat{\epsilon} = \epsilon_0 + \epsilon_1 \Delta C_l{}^2 \end{cases} \qquad (5.48)$$

where $\omega_0, \omega_1, \eta_0, \eta_1, \epsilon_0, \epsilon_1$ are all empirical coefficients.

5.3) UNIFIED MODEL

To incorporate stall modeling within the flexible airfoil theory, each generalized load L_n is presented with its own ONERA-like stall correction. The linear airloads are calculated by Johnson/Peters state-space airloads theory with their own appropriate inflow model. The total loads including dynamic stall for each generalized coordinate are computed by the use of the second-order differential equation of ONERA model as

$$\frac{b^2}{U}\ddot{\Gamma}_{n2} + \hat{\eta}\frac{b}{U}\dot{\Gamma}_{n2} + \hat{\omega}^2\Gamma_{n2} = -bu\hat{\omega}^2\left[\Delta C_l + \hat{\epsilon}\frac{d(\Delta C_l)}{dt}\frac{b}{U}\right] \qquad (5.49)$$

where the time derivative $d(\Delta C_l)/dt$ is calculated through the time derivative of stall residuals explained in Appendix D. Γ_{n2} is the loss in generalized circulation due to dynamic stall of the nth generalized load.

Once the dynamic stall is computed, it is possible to obtain the total lift coefficient by simply adding the linear part (obtained from the first-order differential equation) to the non-linear part (obtained by the second-order differential equation re-written above) as

$$C_l = C_{l(l)} + \frac{\Gamma_{n2}}{Ub} \qquad (5.50)$$

The stall correction then feeds back through the induced flow and modifies the linear loads (see the term $\dot{\Gamma}_{n2}$ in equation 5.39 in Chapter 5.1). The coefficients of interest (like the lift and moment coefficients) can then be calculated from the generalized airloads. Figure 5.6 shows this feedback loop and how the equations of the unified model are linked.

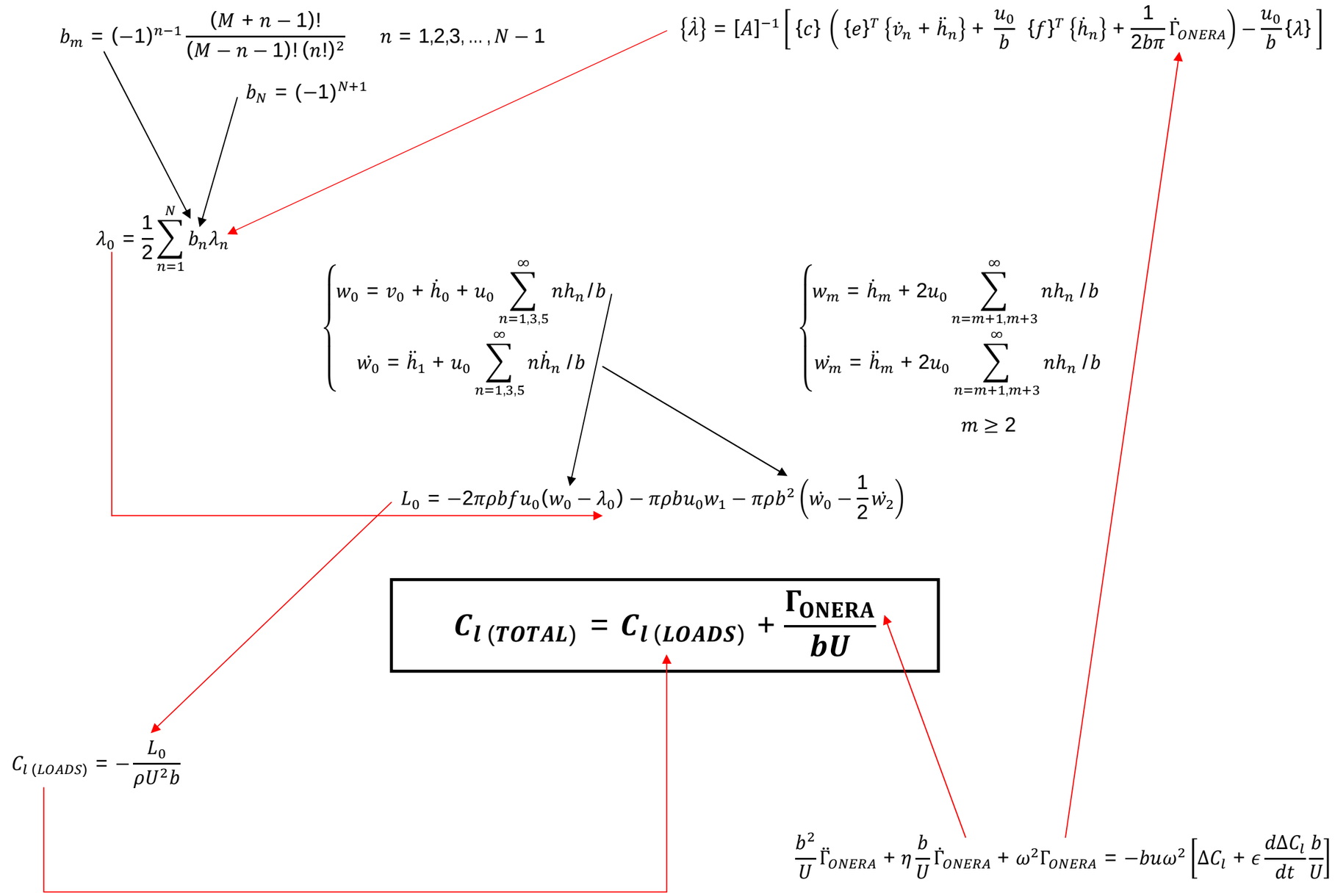

Figure 5.6: Feedback loop.

5.4) STATIC CORRECTION FACTOR

To account for thickness and compressibility effects some corrections factors must be added to correlate with experimental data. NASA performed various wind tunnel tests for the NACA 0012 airfoil which show that the slope of the lift curve is not 2π (like thin airfoil theory predicts) but is a function of both Reynolds and Mach numbers. For Reynolds numbers between $2 \cdot 10^6$ and $2 \cdot 10^7$ the lift curve slope is approximated by

$$C_{l\alpha} = \frac{5.8728 + 0.2997 \log\left(Re/10^6\right)}{\sqrt{1 - Ma^2}} \qquad (5.51)$$

This correction is used in this theory instead of the factor 2π.

Other static correction factors are considered in the case of an airfoil with a trailing edge flap (or a leading edge slat). The flap deflection change effectively the shape of the camber line of the airfoil and thus the lift coefficient change accordingly. Viscous effects decrease significantly the ability of the flap to generate lift. The presence of the flap creates a discontinuity in the thick turbulent boundary layer, the flap hinge creates an adverse pressure gradient and the gaps alter the boundary layer. Corrective factors needed to take into account this loss of effectiveness are presented later in Chapter 8.2.

6) STATIC AIRFOIL SECTION CHARACTERISTICS

As in Chapter 5.2 the dynamic stall model is driven by the static stall residuals, which depends on the airfoil shape. For airfoil with fixed geometry these data can be obtained easily from tables or wind tunnel tests but for morphing airfoils is different: their static characteristics change with the airfoil shape and there is no tables that can predict the values. Only limited wind testing data are available.

In order to get these data, static airload values for the baseline airfoil are needed, as well as values of the morphing variables considered.

The generalized spatial gradient coefficients h_n' (see Appendix B) are calculated by a transformation from the morphing variables and then used to parameterized the curves. In this manner it is possible to obtain a static database in terms of generalized coordinates that can be used for every arbitrary morphed airfoil. The airfoil considered here are the symmetric NACA 0012 and the cambered SC-1095. These two airfoils behave linearly for small angles of attack and so the thin-airfoil theory can be adopted. This theory states that

$$C_{l(l)} = C_{l\alpha}(\alpha - \alpha_{0l}) \qquad (6.1)$$

where α_{0l} is the angle of attack at which zero lift is produced. For a symmetric airfoil, like NACA 0012, α_{0l} is zero.

All the lift curves of different airfoils pass through the origin if they are plotted as function of $\alpha - \alpha_{0l}$ and therefore it is possible to have a general overview about the trend.

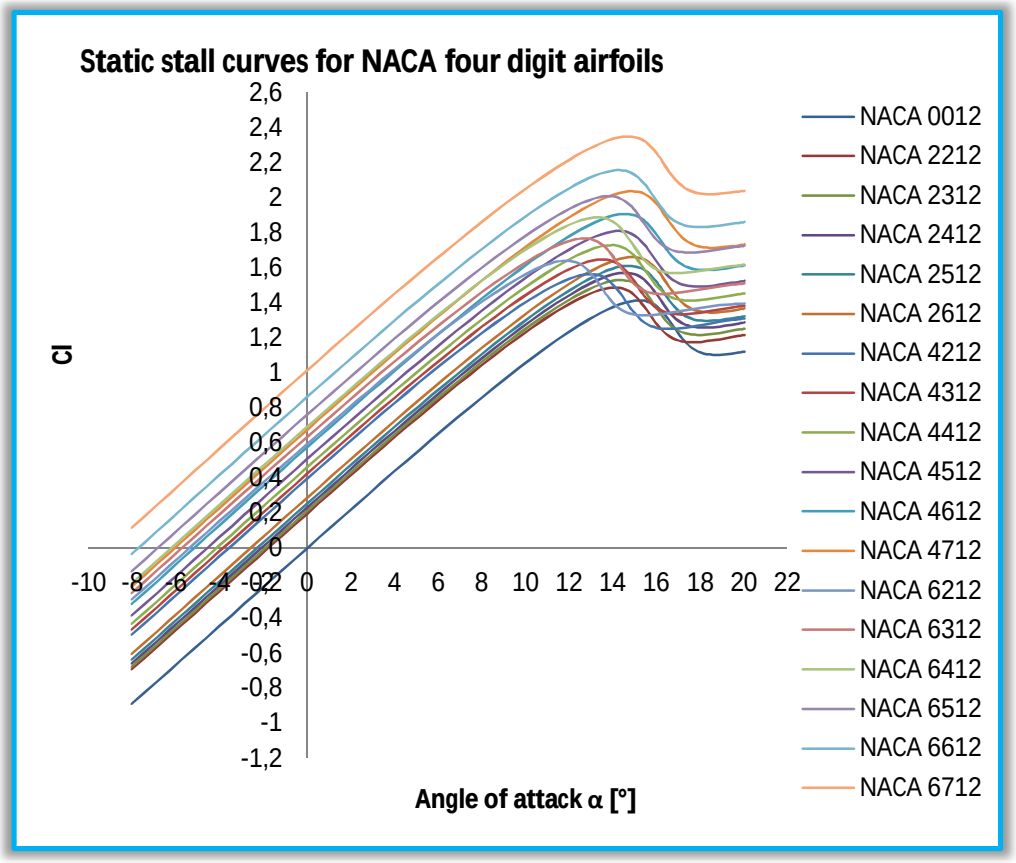

Figure 6.1: Static stall curves for 18 NACA four digit airfoils.

The linear portion of each curve collapse onto a single line and only the non-linear part (the post-stall behavior) has a different trend for each airfoil. This is the part that properly distinguish each airfoil from the others and depends on the angle at which stall occurs. A more interesting graph is obtained when airfoils of the same family are considered (Figure 6.1), since this makes it possible to approximate them by a single lift curve by the synthesis of the linear portion of the lift curve and the post stall behavior. The transition from one regime to the other is defined by the static stall angle α_{ss} which is a function of the generalized coordinates. The static stall angle could be considered the angle at which the experimental lift deviate from the linear. This could be problematic because each airfoil has its own static stall trend. For simplicity, the angle of static stall is considered to be the angle where maximum lift occurs.

The lift residuals are the difference between the expected linear lift given by thin-airfoil theory (equation 6.1) and the experimental lift.

The only difference is that another angle has to be considered in order to collapse all the curves of the residuals in one unique curve (Figure 6.2). This angle is α_{shift} and it is used to align the curves of the residuals with the one of the baseline:

$$\alpha_{shift} = \alpha_{ss(m)} - \alpha_{0l(m)} - \left(\alpha_{ss(b)} - \alpha_{0l(b)}\right) \qquad (6.2)$$

where subscripts (m) and (b) imply the morphed and the baseline airfoil respectively.

α_{shift} is thus zero for the baseline airfoil. Plotting the residual curves as function of $\alpha - \alpha_{0l} - \alpha_{shift}$ permit to align and fit them with a polynomial to provide the approximate static lift for any morphed airfoil. This is extremely useful because the polynomial provides a unique function that can be used for any arbitrary morphology of the baseline airfoil, i.e. it is possible to obtain the characteristics of any morphed airfoil by knowing the characteristics of its baseline. This is a remarkable result obtained by the parameterization with the generalized spatial gradient coefficients h'_n.

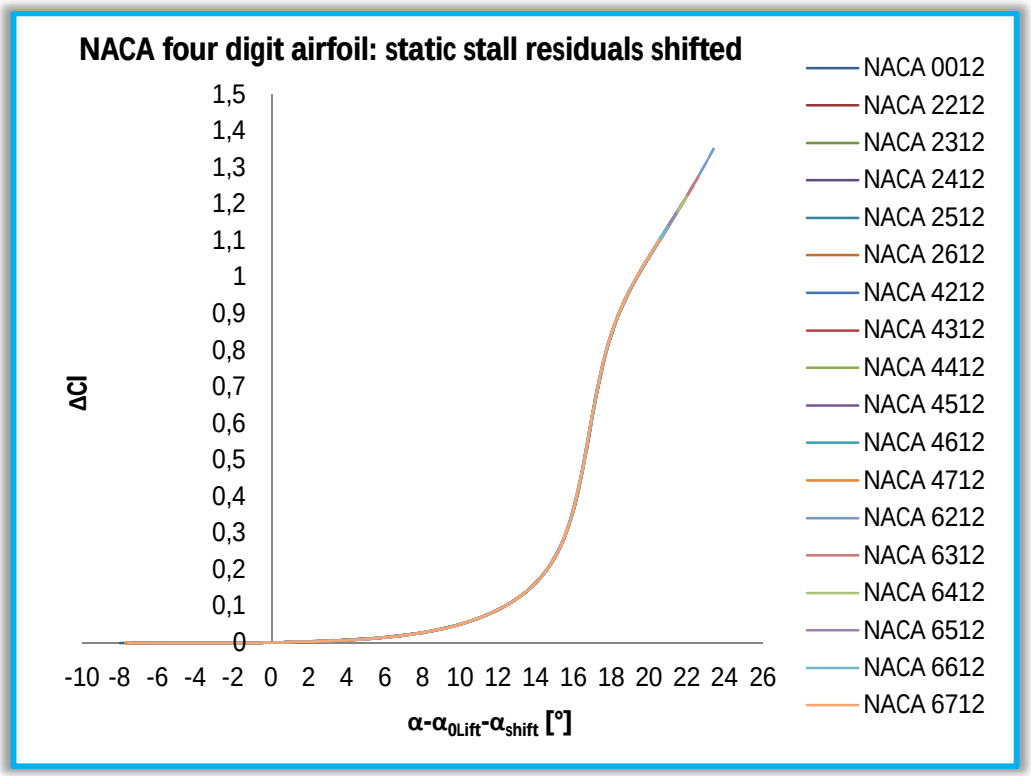

Figure 6.2: Static stall residuals shifted for 18 NACA four digit airfoils.

To be of general value, all the angles are parameterized in terms of generalized morphing variables. As said before, every generalized load residual ΔC_n will be zero until α approaches the static stall angle α_{ss}. That is, the residuals are negligible for angles of attack lower than α_{ss}. As it can be seen in the following section, ΔC_n is a function of z, where

$$z = \alpha - \alpha_{ss(m)} \qquad \text{for } z_0 \geq \alpha_{ss} \qquad (6.3)$$

and z_0 is the value of z below which the stall residual is negligible. The selection of the right z_0 is given to the user. This particular value of z_0 allows the transition between unstalled and stalled behavior at α_{ss}. In terms of the shifted parameters, z can be re-written as follows:

$$z = \alpha - \alpha_{ss(m)} = \alpha - \alpha_{0l(m)} - \alpha_{shift} - \left(\alpha_{ss(b)} - \alpha_{0l(b)}\right) \qquad (6.4)$$

For the baseline airfoil $\alpha_{shift} = 0$ and the morphed variable becomes the baseline one so z is given by

$$z = \alpha - \alpha_{ss(b)} \qquad (6.5)$$

6.1) LINEAR AIRLOADS

In this section are considered the contributions due to the variable geometry of the airfoil to the linear airloads. These contributions are obtained by the expansion in a Glauert series of the spatial gradients h'_n (Appendix B).

The boundary condition (non-penetration) is given by

$$w = \bar{v} + \lambda = u_0 \frac{\partial h}{\partial x} + \frac{\partial h}{\partial t} + v_0 + v_1 \frac{x}{b} = \sum_{n=0}^{\infty} w_n \cos(n\varphi) \qquad (6.6)$$

If the airfoil considered has an arbitrary shape and it is at a fixed angle of attack in a steady horizontal free stream it is possible to make some simplifications to obtain

$$w = u_0 \left(\alpha + \frac{\partial h}{\partial x}\right) = \sum_{n=0}^{\infty} w_n \cos(n\varphi) \qquad (6.7)$$

This new condition contains only the contribution of the morphing geometry. The spatial gradients can now be expanded in Glauert series as done before for the generalized deformations, velocities and induced flow (Chapter 5). It follows that

$$\frac{\partial h}{\partial x} = \sum_{n=1}^{\infty} h'_n \cos(n\varphi) \qquad (6.8)$$

Substitution of this result in the previous equation and the grouping of like terms gives the generalized velocities in a Glauert expansion due to morphing only, where the driver parameters are the spatial gradient coefficients h'_n (Appendix B):

$$w_0 = u_0(\alpha + h'_0) \qquad (6.9)$$

$$w_n = u_0 h'_n \qquad n \geq 1 \qquad (6.10)$$

From thin-airfoil theory the lift coefficient is given by

$$C_{l(l)} = \frac{C_{l\alpha}}{u_0}(w_0 + 0.5w_1) \qquad (6.11)$$

and the ideal zero lift condition is

$$\alpha_{0l} = -(h'_0 + 0.5h'_1) \qquad (6.12)$$

For a symmetric airfoil $h'_0 = h'_1 = 0$ and thus $\alpha_{0l} = 0$.

6.2) STATIC STALL RESIDUALS

Static stall residuals are the forcing functions of the second order differential equation of ONERA model. In order to solve this equation, one must know the static stall residuals. If available, these data must be computed from experimental data by

$$\Delta C_l = C_{l(l)} - C_{l(ss)} = C_{l0}\, cos(\alpha) + C_{l\alpha}\, sin(\alpha) - C_{l(e)} \qquad (6.13)$$

$$\Delta C_m = C_{m0}\, cos^2(\alpha) + C_{m\alpha}\, sin(\alpha)\cos(\alpha) + \frac{a}{2} C_d \sin(\alpha) - C_{m(e)} \qquad (6.14)$$

where C_{l0} and $C_{l\alpha}$ are the magnitude and the slope of the lift curve at $\alpha = 0$ respectively and similarly C_{m0} and $C_{m\alpha}$ for the moment curve.

$C_{l(ss)}$ is the coefficient of lift due to stall and $C_{l(e)}$ is the experimental value of C_l. $C_{l\alpha}$ is the static correction factor presented in Chapter 5.4 whereas C_{l0} , C_{m0} and $C_{m\alpha}$ can be computed from thin-airfoil theory as

$$C_{l0} = C_{l_\alpha}(h_0' + 0.5h_1') \qquad (6.15)$$

$$C_{m0} = -\frac{\pi}{4}(h_1' + h_2') \qquad (6.16)$$

$$C_{m\alpha} = 0 \qquad (6.17)$$

6.3) NACA 0012 AIRFOIL

NACA 0012 airfoil is frequently used as the baseline to demonstrate the validity of a new theory or a computational approach because there are so many static and dynamic data available (See Reference [9] for a complete evaluation of NACA 0012 wind test data). NACA four digit airfoils, like NACA 0012, are usually denoted like NACA *mpxy* where the first digit, *m*, denote the maximum ordinate mean line in percent chord; the second digit, *p*, denote the chord-wise position of maximum ordinate in tenths of chord and finally the last two digit, *xy*, denote the maximum thickness of the airfoil in percent of chord. Therefore the NACA 0012 airfoil is a symmetric airfoil with a thickness equal to 12% of the chord. The meanline has no slope or curvature.

It is not necessary to perform tests for every combination of morphed airfoil and angle of attack to obtain a database of static data: this would be quite complex and would limit the value of the present theory. What it is proposed is that a small subset of static data collected at various values of the morphing variables are parameterized in terms of the generalized spatial gradients coefficients. This database can then be used to analyze any morphing airfoil in terms of the generalized coordinates without taking into account the particular morphology used to create them.

6.3.1) LIFT RESIDUAL

For NACA four digit airfoils, the mean line is known in closed form, so the velocity due to the shape of the airfoil can be computed directly. The first three terms of the generalized spatial gradients coefficients are

$$h_0' = \frac{4mq}{(1-q^2)^2}\left[\frac{4}{\pi}(qsin^{-1}q + \sqrt{1-q^2}) - (1+q^2)\right] \qquad (6.18)$$

$$h_1' = \frac{4m}{(1-q^2)^2}\left[(1+q^2) - \frac{4}{\pi}(qsin^{-1}q + q^2\sqrt{1-q^2})\right] \qquad (6.19)$$

$$h_2' = \frac{32m}{3\pi}\frac{q}{\sqrt{1-q^2}} \qquad (6.20)$$

where $q = 2p - 1$.

The derivations of these terms and of the fourth one are included in Appendix B. However, only the first three terms are used here to build up the static stall database.

Following section 6.1, the equation for α_{0l} is given by $-(h_0' + 0.5h_1')$ but to improve the fit an empirical correction is made by adding a term in h_2'. The new angle of zero lift becomes

$$\alpha_{0l} = -0.87(h_0' + 0.5h_1') + 0.087h_2' \qquad (6.21)$$

The correction factor is added in order to take into account thickness and viscous effects. With such a correction, the equation agrees well with the experimental values of α_{0l}. To make sure that the lift curves collapse onto a single curve, the plot has to be done in function of the angle difference $\alpha_{ss} - \alpha_{0l}$. This difference is obtained by an approximation in terms of h_1' and h_2' and is valid for any NACA four digit airfoil

$$\alpha_{ss} - \alpha_{0l} = 0.293 + 0.336h_1' + 0.403h_2' \qquad (6.22)$$

in which the constant value 0.293 represents the stall angle of the baseline NACA 0012 airfoil, for which, as it has been said before, $h_0' = h_1' = h_2' = 0$ because it is a symmetric airfoil.

Equation (6.22) seems to indicate that the contribution of h_0' is none, but the effect of this term is included in the definition of α_{0l}. Combining (6.21) and (6.22) it is possible to obtain the angle of static stall as

$$\alpha_{ss} = 0.293 - 0.870h_0' - 0.099h_1' + 0.490h_2' \qquad (6.23)$$

From such an expression, the angle of static stall of every other airfoil can be calculated by simply using their characteristic spatial gradients coefficients. The last angle needed is the angle of shift, that ensures the alignment of all the residual curves with the baseline one. This angle, as expected, is function only of the morphing h_1' and h_2' and is given by

$$\alpha_{shift} = 0.336h_1' + 0.403h_2' \qquad (6.24)$$

If the airfoils considered belong to the same family, they have a similar post-stall behavior that differ from each other only on the value at which the maximum C_l occurs, i.e. they differ only by the angle of static stall that is a function of the airfoil shape as said at the beginning of this Chapter.

This procedure permits to obtain a single typical curve or polynomial fit that gives the static lift residual for any morphed airfoil in terms of h_0', h_1' and h_2'. The approximate closed-form expression for the mean lift residual is (Reference [4])

$$\Delta C_l = 0.2689\, tan^{-1}(54.54z) + 15.89(z + 0.3192)^4 + 0.4070 \quad z \geq 0 \qquad (6.25)$$

6.3.2) PITCHING MOMENT RESIDUAL

What has been said for the lift coefficient works also for the pitching moment coefficient. The only thing that change is that there is a vertical offset in the moment curves due to the non-zero pitching moment created by a cambered airfoil. This offset is approximately 20% smaller than the theoretical value of $-\pi/4\,(h_1' + h_2')$ and it is consistent with the static corrections made in the linear airload theory. It is given by

$$C_{m0} = -0.615(h_1' + h_2') \qquad (6.26)$$

For simplicity, the angle of static stall used to calculate the pitching moment is the same of the lift curves. For a more accurate description of the pitching moment, this angle should be derived independently. With this assumption, the shift angle has the same expression of the one used to obtain the lift residuals. Similarly, the fit curve that approximate the whole pitching curves is given by (see Reference [4])

$$\Delta C_m = 0.0276 \tan^{-1}(54.54z) + 2.177(z + 0.3048)^4 + 0.0435 \quad z \geq 0$$

(6.27)

6.4) SC-1095 AIRFOIL

SC-1095 airfoil is a cambered airfoil used in the UH-60A helicopter. Reference [7] shows a study on different morphologies of this airfoil. The ones interesting to verify this new theory approach are the leading and trailing edge deflections. Nevertheless the geometric details of this airfoil were not released, only the meanline shape of the airfoil is needed to validate this theory and fortunately an approximate parabolic representation of the meanline is sufficient. An accurate description to obtain such a shape, with a leading and trailing edge droop, can be found in Appendix C. As for NACA 0012, the static characteristics of the airfoil are parameterized in terms of h_0', h_1' and h_2'. The only difference in this case is that these spatial gradient coefficients are functions both of the deflection angles and the transition points to the baseline geometry (the points at which the deflection is applied).

Based on the meanline equation of the airfoil, the angle of zero lift obtained from the CFD data (see Reference [7]) is

$$\alpha_{0l} = -0.88(h_0' + 0.5h_1') - 0.012 \qquad (6.28)$$

in which it can be seen that the correction factor is nearly identical to the NACA 0012. This correlation is really interesting, because indicates that this is truly the angle of zero lift for the SC-1095 airfoil. Another interesting element of the expression is the constant offset of -0.012. This is due to the fact that the airfoil is not symmetric and it has a cambered meanline.

It is possible to obtain all the static stall data for the SC-1095 airfoil from the same steps followed for the NACA 0012 airfoil (Figures 6.3-6.4). The shift angle is

$$\alpha_{shift} = 0.481h_1' + 1.10h_2' \qquad (6.29)$$

whereas the approximate fits for ΔC_l and ΔC_m are

$$\Delta C_l = 0.2959 \tan^{-1}(42.76z) + 21.83(z + 0.2320)^4 + 0.4351 \quad (6.30)$$

$$\Delta C_m = 0.9246 \tan^{-1}(7.940z) + 5.956z - 0.166z^2 + 50.23z^3 + 5.354z^4 - 248.9z^5 + 0.0561$$

(6.31)

both valid when z is higher than -0.22. This is equivalent to have $\alpha - \alpha_{0l} - \alpha_{shift} > 0$.

The expression for z is

$$z = \alpha - \alpha_{ss} = \alpha - \alpha_{0l} - \alpha_{shift} - \left(\alpha_{ss\,(b)} - \alpha_{0l\,(b)}\right) \qquad (6.32)$$

with

$$\alpha_{ss\,(b)} = 0.21 \qquad \alpha_{0l\,(b)} = -0.012 \qquad (6.33)$$

These equations permit to have a generalized expression for the static stall residuals as a function of only the generalized spatial gradients h'_n.

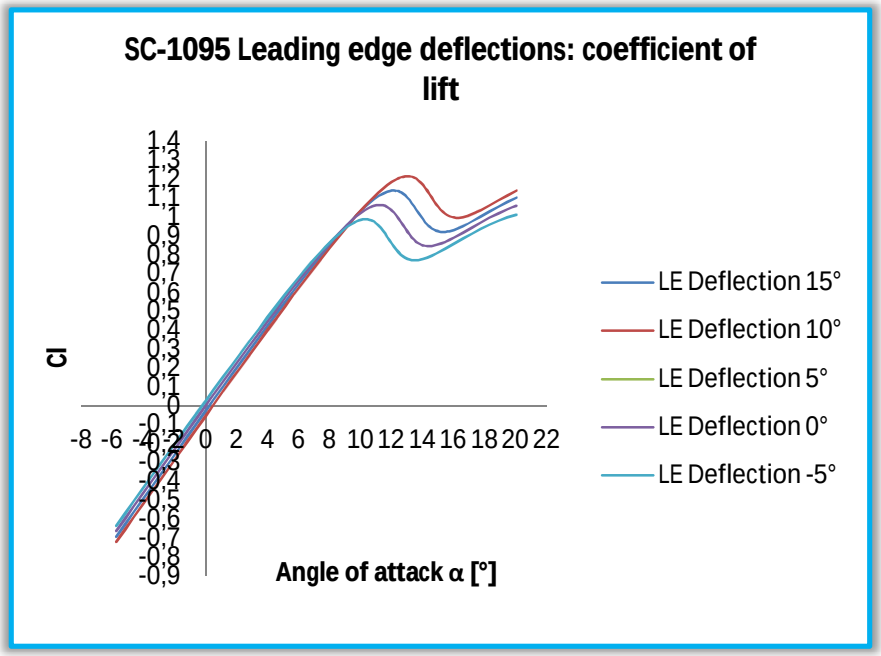

Figure 6.3: SC-1095 Coefficient of lift with different leading edge deflections.

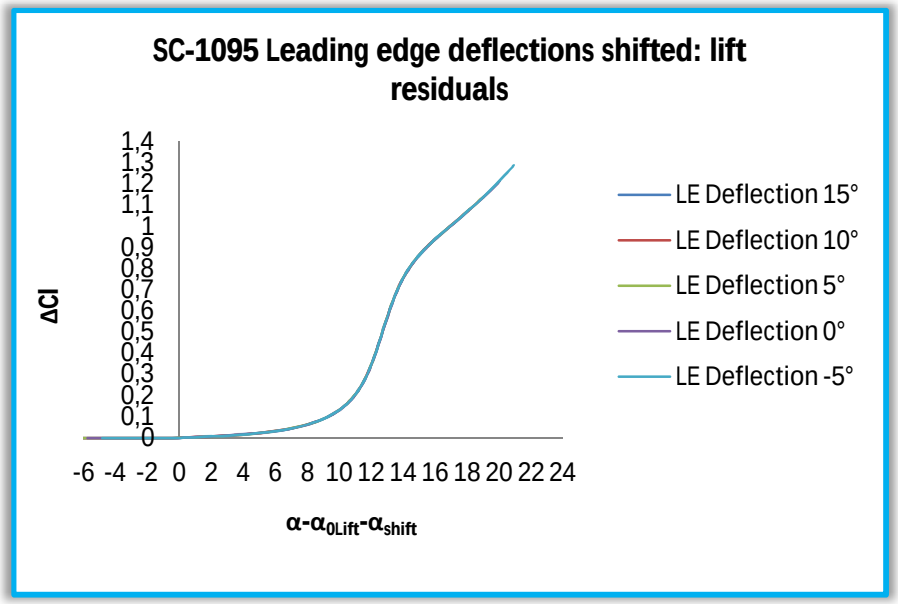

Figure 6.4: SC-1095 Shifted lift residuals with different leading edge deflections.

All the figures presented can be obtained also for the moment coefficient, the trailing edge deflection and a simultaneous leading and trailing edge deflection. For further information about these latter see Reference [4].

6.5) CONCLUSIONS

The airfoil's meanlines of NACA 0012 and SC-1095 has been expanded into the spatial gradients coefficients in order to obtain the static data parameterized in terms of these first three components of the expansion. The result is a single curve or polynomial that fit the data and can be used to predict the static section characteristics for any arbitrary morphology of the baseline airfoil. This means that it is possible to obtain the characteristics of any morphed airfoil by knowing only the characteristics of its baseline. Remembering from chapter 5.2 that the function responsible for the evaluation of the loss of lift due to dynamic stall is given by

$$\frac{b^2}{U}\ddot{\Gamma}_{n2} + \hat{\eta}\frac{b}{U}\dot{\Gamma}_{n2} + \hat{\omega}^2\Gamma_{n2} = -bU\hat{\omega}^2\left[\Delta C_l + \hat{\epsilon}\frac{d\Delta C_l}{dt}\frac{b}{U}\right] \qquad (6.34)$$

with the stall parameters defined as

$$\begin{cases} \hat{\omega} = \omega_0 + \omega_1 \Delta C_l^{\,2} \\ \hat{\eta} = \eta_0 + \eta_1 \Delta C_l^{\,2} \\ \hat{\epsilon} = \epsilon_0 + \epsilon_1 \Delta C_l^{\,2} \end{cases} \qquad (6.35)$$

it is possible to shown clearly the dependence of the dynamic stall on lift residuals (static section characteristics). Therefore, having a single curve (or polynomial) that fit all the residuals is a powerful tool for predicting the dynamic stall: with a single curve it is possible to describe the dynamic stall of any arbitrary morphology of the baseline airfoil.

7) DETERMINATION OF STALL PARAMETERS

This section outlines the procedure used to identify appropriate stall parameters using large-amplitude test data (Reference [8]). A genetic algorithm is used to find the optimum set of parameters. The airfoil selected to validate the theory are a morphed NACA 0012 and the SC-1095 as well. The airfoil used to obtain the expressions is instead the modified Boeing VR-12 airfoil with a variable-droop leading edge. All the experimental data can be found in Reference [8] and [28]. In the tests executed by the authors, the forward 25% of the airfoils remains at zero angle of attack with respect to the free stream whereas the rear 75% perform a pitch oscillation given by:

$$\alpha = 10° + 10°\sin(k\tau) \qquad (7.1)$$

The tests were done at reduced frequencies $k = 0.025, 0.05, 0.075$ and 0.1. τ is the reduced time. The first case is considered quasi-steady and, as explained in Chapter 2 (Figure 2.9), the dynamic lift curve approximates the static one. The lift residual ΔC_l, calculated from the experimental data, is used by ONERA model to calculate the loss of circulation. This latter is obtained by the numerical solution of the second-order differential equation in MATLAB. The numerical solution is then compared to the experimental data and finally a fitness function E is extrapolated, which is simply the sum of the error norms at each of the four reduced frequencies

$$E = E_{0.025} + E_{0.05} + E_{0.075} + E_{0.1} \qquad (7.2)$$

where E is given by

$$E_k = \frac{\frac{1}{N}\sum_{1=1}^{N}|\hat{g}_i(\alpha) - g_i(\alpha)|}{g_{max} - g_{min}} \qquad (7.3)$$

in which g is the experimental data of interest, $\hat{g}$ is the numerical solution and N is the number of points at which the function is evaluated. Further information about the fitness function can be found in Reference

[4]. This is the procedure followed for the Boeing VR-12 and used also for NACA 0012 airfoil and SC-1095.

7.1) FOR NACA 0012 AIRFOIL

In a report which describes the phenomenon of dynamic stall, McCroskey [10] published static and dynamic lift and pitching moment results for several airfoils, including the NACA 0012. These data are used to identify stall parameters for the 0012 airfoil. The static lift residual is computed as explained in Chapter 6.3.1 and is then passed through the dynamic stall second-order differential equation of ONERA model. The optimal stall parameters are then identified through a genetic algorithm optimization. The final set of these stall parameters for the NACA 0012 are

$$\begin{cases} \hat{\omega} = 0.27 + 0.13\Delta C_l{}^2 \\ \hat{\eta} = 0.52 + 0.22\Delta C_l{}^2 \\ \hat{\epsilon} = -0.10\Delta C_l{}^2 \end{cases} \qquad (7.4)$$

Figure 7.1 shows a comparison between the numerical results and the real data collected in Reference [10]. In this case of Figure 7.1, the stall parameters selected for an optimal fit are the following

$$\begin{cases} \hat{\omega} = 0.2581 - 0.0264\Delta C_l{}^2 \\ \hat{\eta} = 0.3861 + 0.223973\Delta C_l{}^2 \\ \hat{\epsilon} = -0.0294 - 0.1607\Delta C_l{}^2 \end{cases} \qquad (7.5)$$

agreeing with reference [16] from which these values of $\hat{\omega}$, $\hat{\eta}$, and $\hat{\epsilon}$ are obtained.

The numerical simulations are run with two induced flow models: Theodorsen's inflow model and the model developed in Reference [13]. Figure 7.1, shows that Theodorsen's inflow model matches closely the data: the linear part collapses onto the experimental data while the non-linear part departs from them only slightly.

Regarding the curve obtained with the model [13], the trend is quite similar but it is possible to see the action of the feedback through the induced flow that modifies the linear airloads (see Figure 5.6). This can be observed in the linear part of the curve but it also affects the whole curve obtained during the first cycle of integration. The feedback

starts instantly after the first time step of integration and the model needs three cycles to converge.

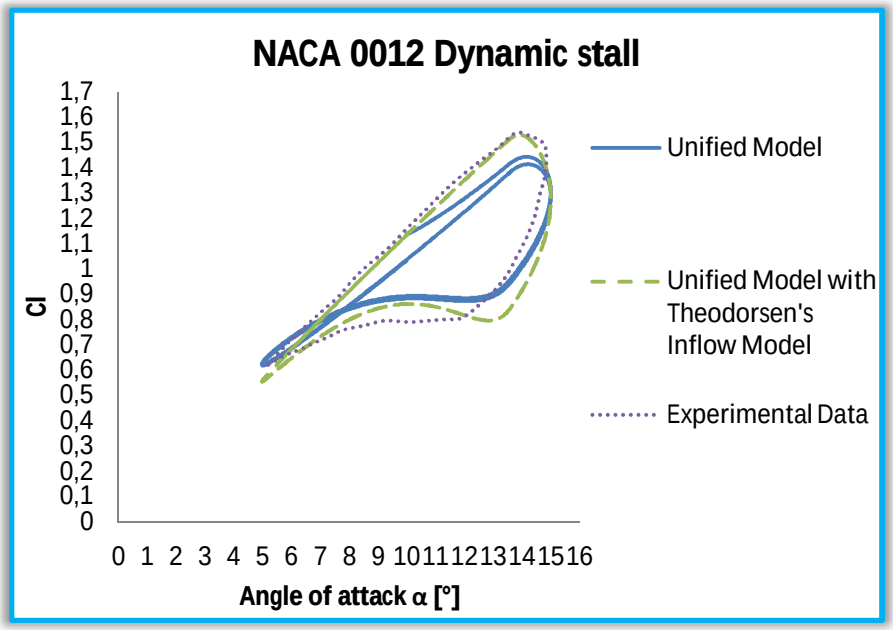

Figure 7.1: NACA 0012 Dynamic stall with two different inflow models.

7.2) STALL PARAMETERS FOR SC-1095 AIRFOIL

The dynamic stall parameters for the SC-1095 airfoil are estimated by the method used for the NACA 0012 airfoil. The estimated parameters are

$$\begin{cases} \hat{\omega} = 0.26 + 0.51\Delta C_l{}^2 \\ \hat{\eta} = 0.49 + 0.21\Delta C_l{}^2 \\ \hat{\epsilon} = 0.013\Delta C_l{}^2 \end{cases} \qquad (7.6)$$

Figures 7.2, 7.3 and 7.4 show the comparison between the experimental data and the numerical results obtained with the implementation of the unified model. Similarly to the previous case Theodorsen's inflow model matches closely the data. The linear part collapses onto the experimental data while the non-linear part departs from them only slightly. Regarding the curve produced by the unified model, the trend is quite similar and it is possible to see again the action of the feedback through the induced flow that modifies the linear

airloads. The effect of the feedback is more emphasized here and the results with Theodorsen's inflow model fit the real data quite well, except from the small region around zero. It is interesting to point out that a better correlation is obtained for higher reduced frequencies.

All the stall parameters used for NACA 0012 and SC-1095 airfoils are listed in Table 7.1 below.

Table 7.1: Stall parameters of the airfoils.

	ω_0	ω_1	η_0	η_1	ϵ_0	ϵ_1
NACA 0012	0.2581	-0.0264	0.3861	0.223973	-0.0294	-0.1607
SC-1095	0.26	0.51	0.49	0.21	-	0.013

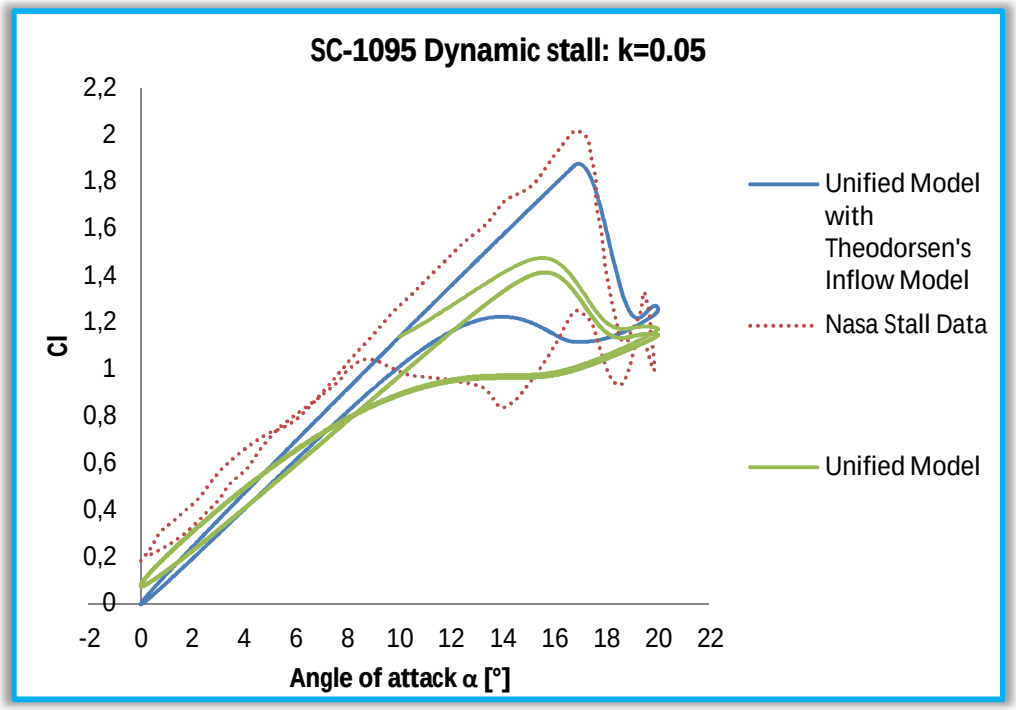

Figure 7.2: SC-1095 Dynamic stall with two different inflow models.

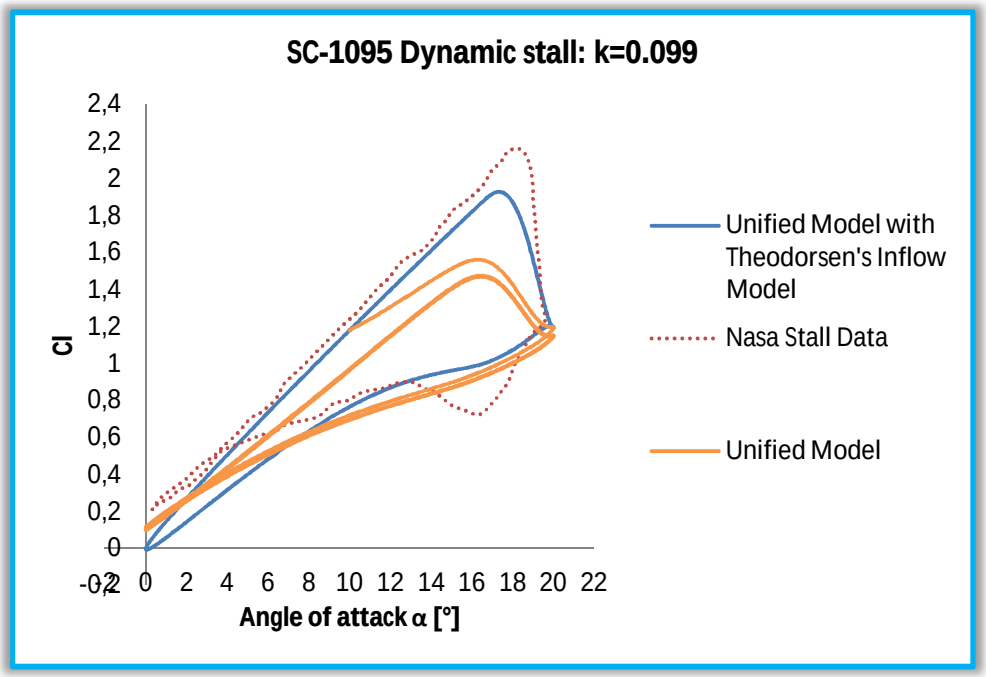

Figure 7.3: SC-1095 Dynamic stall with two different inflow models.

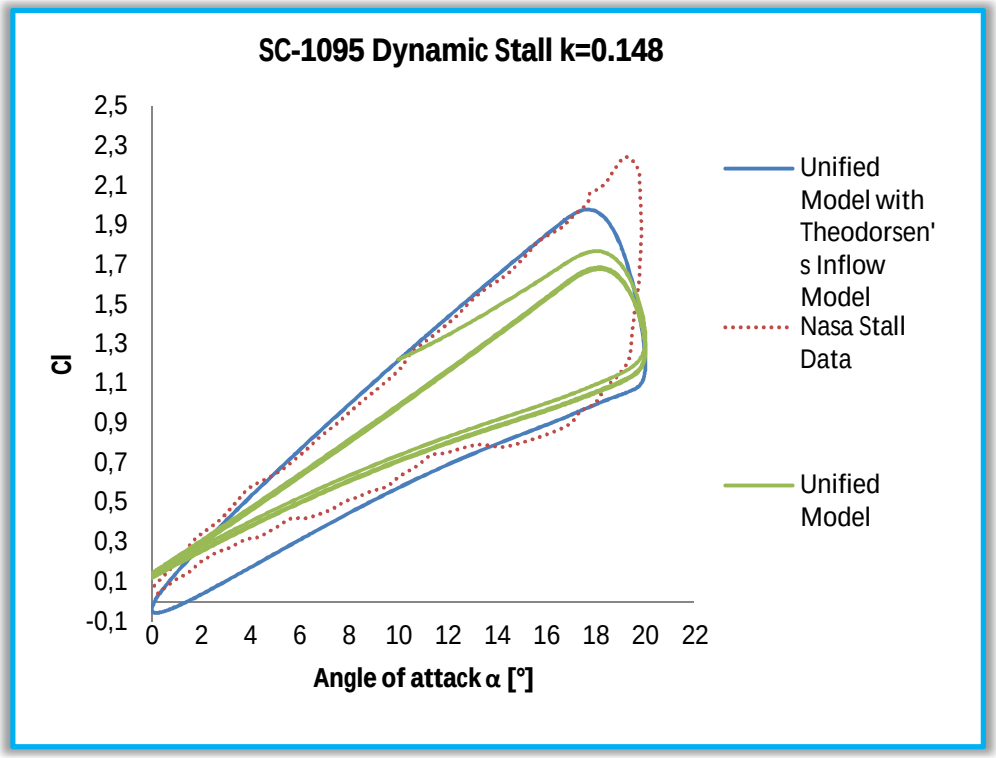

Figure 7.4: SC-1095 Dynamic stall with two different inflow models.

8) DYNAMIC AIRLOAD CORRELATIONS WITH DYNAMIC STALL DATA

In this section the accuracy of Johnson/Peters flexible airload theory will be verified by comparison with dynamic stall data. The theory is used to predict airloads for a drooped leading edge SC-1095 airfoil. This is a very important case because it has a variable geometry which is not present in the other examples of Chapter 7 and Chapter 9. In addition, correlations are presented for experimental data on NACA 0012 airfoil with trailing edge flap deflections.

8.1) SC-1095 WITH LEADING EDGE DROOP

Here we consider the SC-1095 airfoil with a leading edge droop to demonstrate that the unified model is applicable to cambered airfoils with a leading edge droop. Of particular interest is to investigate the mitigation of the dynamic stall due to a dynamic droop deployment (Figure 8.2) for high-thrust forward flight conditions. The motion of the main airfoil α and leading edge droop θ_{LE} are given by

$$\alpha = 10° + 10° \sin(k\tau) \qquad (8.1)$$

$$\theta_{LE} = \theta_0 \sin(nk\tau + \phi) \qquad (8.2)$$

respectively, where θ_0 is the amplitude of the trailing edge droop, ϕ is the phase angle and n is the number of times per revolution the droop is deployed. The reduced frequency used is $k = 0.05$ and the corrections factors are $f_\alpha = 1.044$ and 1 for all the others. This means that only a small correction of the slope of the lift curve is needed. The two conditions that provide the best performance improvement - in terms of the percent change in maximum L/D from the baseline airfoil - are the 2° 1/rev droop with a phase angle of 120° and the 3° 2/rev droop with a phase angle of 60° (Figure 8.1).

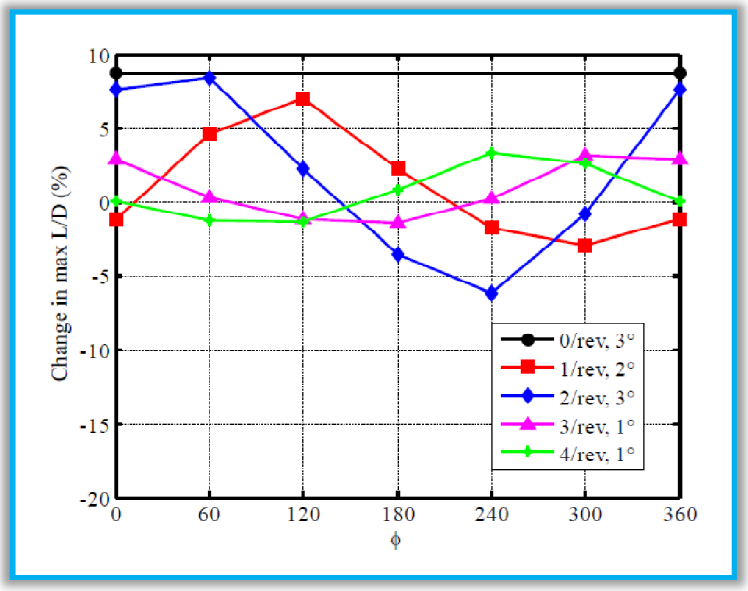

Figure 8.1: Change in airfoil L/D for various leading edge deflections. Figure 5.25 from Reference [4] reprinted here for explanation.

Analyzing the results, it is possible to observe that there is a big difference between the two cases: in the first one the maximum lift is increased, and thus also the efficiency is increased, but the hysteresis in the lift curve is higher in respect of the second case. Actually, this is not a mitigation of the effects of dynamic stall. On the other hand, in the second case the maximum lift is not increased but the hysteresis is less than the previous one, and the mitigation of dynamic stall is higher. Therefore this is the configuration that should be adopted.

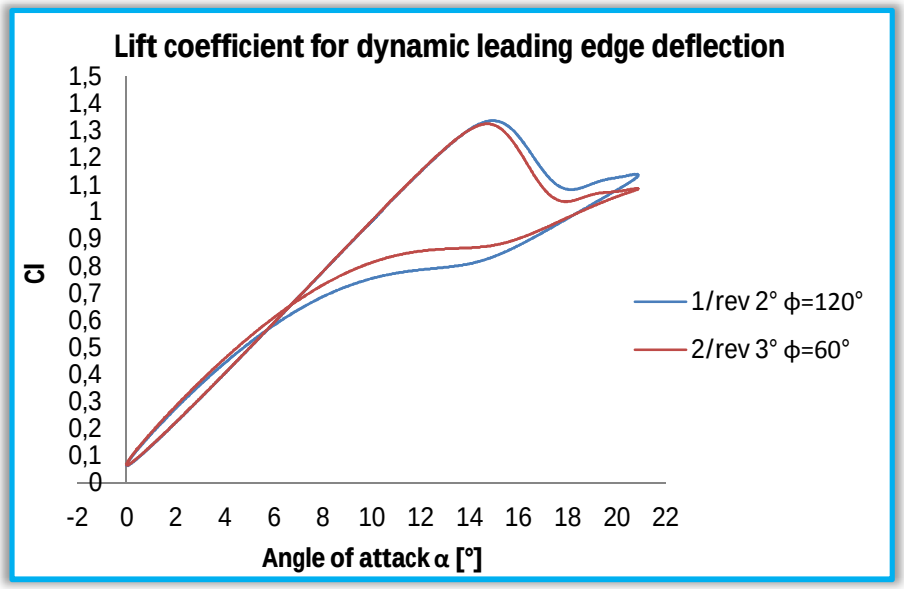

Figure 8.2: Lift coefficient for dynamic leading edge deflection.

8.2) HARMONIC PITCH AND FLAP SIMULATIONS

The data used in this section are obtained for airfoils subjected to forced motions. We consider harmonic variations in pitch angle and trailing edge flap deflection. But first, I will show that the present theory matches Theodorsen's linear theory for pitch and flap deflections. Two cases are considered here

1) a symmetric airfoil undergoing simple harmonic pitching motion α about a point located ab aft of the mid-chord;
2) an airfoil at zero angle of attack and with a trailing edge flap that moves with simple harmonic deflections.

The first case considered is the one of a symmetric airfoil undergoing simple harmonic pitching motion about a point located ab aft of the mid-chord (Figure 8.3), where b is the semi-chord and a is the distance respect to b at which the pitching motion is applied. The theory of Theodorsen in Reference [11], which is included in Appendix E, shows that the lift coefficient is

$$C_{l\,(T)} = 2\pi\left\{\frac{1}{2}\frac{\partial\alpha}{\partial\tau} - \frac{a}{2}\frac{\partial^2\alpha}{\partial\tau^2} + C(k)\left[\alpha + \left(\frac{1}{2} - a\right)\frac{\partial\alpha}{\partial\tau}\right]\right\} \qquad (8.3)$$

where $C(k)$ is Theodorsen lift deficiency function (Figures E.6 and E.7).

For the unified model, with $h_0 = -ba\alpha$ and $h_1 = b\alpha$, the coefficient of lift $C_{l\,(um)}$ is given by

$$C_{l\,(um)} = 2\pi\left\{-a\frac{\partial\alpha}{\partial\tau} - \frac{a}{2}\frac{\partial^2\alpha}{\partial\tau^2} + \frac{\partial\alpha}{\partial\tau} - \frac{\lambda_0}{u_0} + \alpha\right\} \qquad (8.4)$$

and thus comparing these two expressions the steady-state induced flow is obtained as

$$\lambda_0 = \left\{\alpha + \left(\frac{1}{2} - a\right)\frac{\partial\alpha}{\partial\tau}\right\}[1 - C(k)] \qquad (8.5)$$

which is the same result obtained by Theodorsen (see Appendix E, equation $E.43$). This achievement is very important, because it means that with the unified model it is possible to obtain results comparable with Theodorsen's ones, which are supported by experimental data. Figure 8.3 shows the excellent agreement between Theodorsen's theory and the unified model.

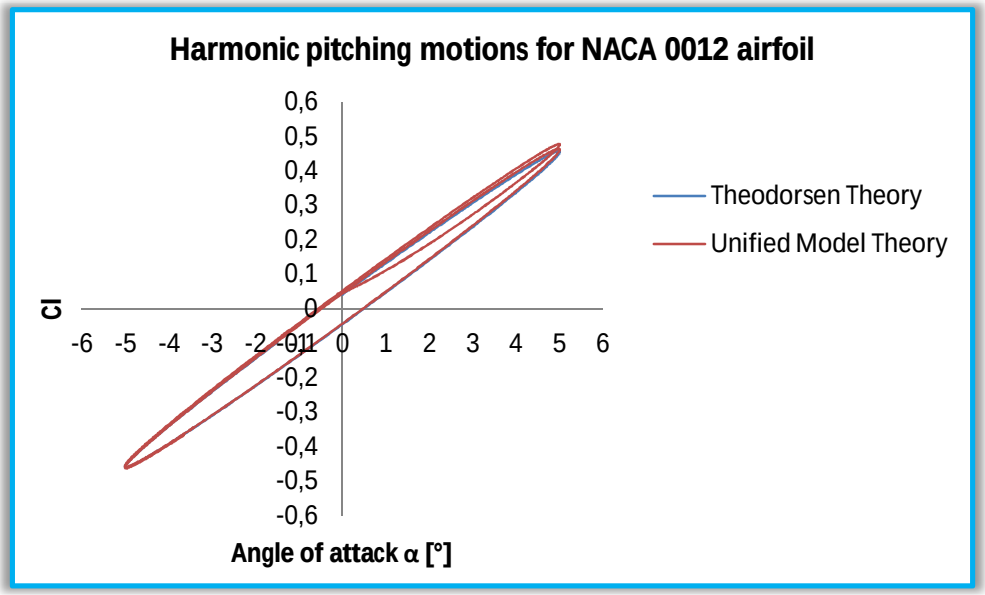

Figure 8.3: Comparison with Theodorsen's theory for harmonic pitch oscillations.

The second case considered (Figure 8.4) is that of an airfoil at zero angle of attack and with a trailing edge flap that moves with simple

harmonic deflections. The flap location is *ab* aft of the mid-chord. Theodorsen [11] showed that the lift in this case is given by

$$C_{l\,(T)} = -T_4 \frac{\partial \beta}{\partial \tau} - T_1 \frac{\partial^2 \beta}{\partial \tau^2} + C(k)\left[2T_{10}\beta + T_{11}\frac{\partial \beta}{\partial \tau}\right] \qquad (8.6)$$

where β is the flap harmonic motion in the form of equation (8.15) and

$$T_1 = -\frac{1}{3}\sqrt{1-d^2}(2+d^2) + d\cos^{-1}(d) \qquad (8.7)$$

$$T_4 = -\cos^{-1}(d) + d\sqrt{1-d^2} \qquad (8.8)$$

$$T_{10} = \sqrt{1-d^2} + \cos^{-1}(d) \qquad (8.9)$$

$$T_{11} = \cos^{-1}(d)\,(1-2d) + \sqrt{1-d^2}(2-d) \qquad (8.10)$$

with d the location of the trailing edge flap.

The Glauert expansion for the deflected flap is $\{h\}_{flap} = \{T\}_{flap}\beta$ where $\{T\}_{flap}$ is given by

$$\{T\}_{flap} = \begin{cases} \frac{1}{\pi}[\sin\varphi_m - \varphi_m \cos\varphi_m] \\ \frac{1}{\pi}[\varphi_m - \sin\varphi_m \cos\varphi_m] \\ \frac{1}{\pi}\left[\frac{1}{1+n}\sin[(n+1)\varphi_m] + \frac{1}{n-1}\sin[(n-1)\varphi_m]\right] \\ \qquad -\frac{2}{n}\sin(n\varphi_m)\cos\varphi_m \\ \qquad \vdots \end{cases} \qquad (8.11)$$

The lift coefficient becomes

$$C_{l\,(um)} = 2\pi\left\{\left(\frac{1}{2}t_0 - \frac{1}{4}t_2\right)\frac{\partial^2 \beta}{\partial \tau^2} + (t_0 + t_1)\frac{\partial \beta}{\partial \tau} - \lambda_0 + \sum_{n=0}^{\infty} n t_n \beta\right\} \qquad (8.12)$$

where t_n's are the components of vector $\{T\}_{flap}$. The induced flow is given by

$$\lambda_0 = \left(t_0 + t_1 + \frac{T_4}{2\pi}\right)\frac{\partial\beta}{\partial\tau} - \frac{C(k)}{2\pi}\left[2T_{10}\beta + T_{11}\frac{\partial\beta}{\partial\tau}\right] + \sum_{n=0}^{\infty} nt_n\beta \qquad (8.13)$$

It should be noted that the term $\partial^2\beta/\partial\tau^2$ is absent because of the cancellation of terms and the infinite sum of the generalized blade deformations. For the validation, only ten terms of the geometric expansion are used. Figure 8.4 show that the unified model recovers perfectly Theodorsen results for harmonic flap oscillations agreeing with Reference [4]. Appendix E describes the relation between Theodorsen/Garrick theory with Johnson/Peters theory.

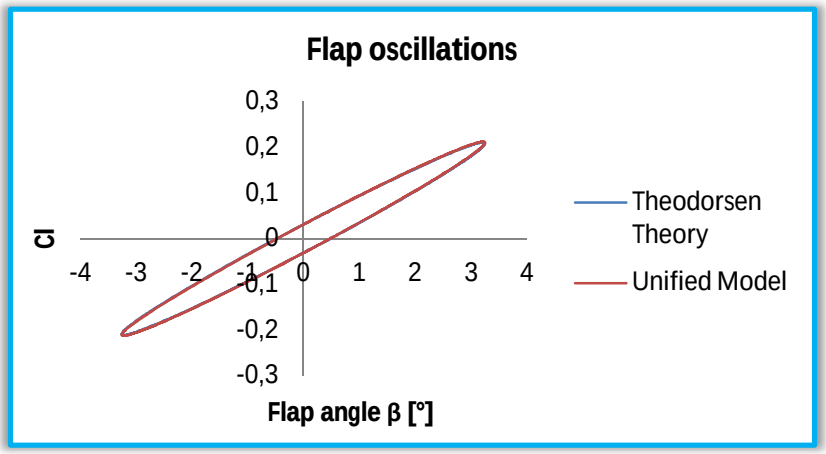

Figure 8.4: Comparison with Theodorsen's theory for harmonic flap oscillations.

8.3) COMBINED PITCH AND FLAP OSCILLATIONS

Reference [12] provides the wind tunnel tests data used to correlate the simulations. The NACA 0012 airfoil is oscillated in pitch about a center of rotation located 35% chord from the leading edge at a reduced frequency $k = 0.02$. At the same time, a 20% trailing edge flap is oscillated at twice the pitch frequency of oscillation of the main airfoil, i.e. $k = 0.04$.

The equations describing the motion of the airfoil α and the flap β are

$$\alpha = \alpha_0 + \bar{\alpha}\sin(k\tau) \qquad (8.14)$$

$$\beta = \beta_0 + \bar{\beta}\sin(2k\tau + \phi) \qquad (8.15)$$

respectively, where ϕ is the phase lag between pitch and flap motions. The parameters α_0, β_0, are the nominal angles of attack and $\bar{\alpha}$, $\bar{\beta}$ are the magnitude of the oscillations. τ is the reduced time. Figures 8.5 to 8.9 show examples of this kind of oscillations for various values of k.

The flap geometry is expanded in Glauert series and it has the form $\{h\}_{flap} = \{T\}_{flap}\beta$ in terms of β derived in equation (8.11).

A transformation between the user variables α and β and the generalized blade deformations h_n is given by $\{h_n\} = [T]\begin{Bmatrix}\alpha\\ \beta\end{Bmatrix}$ where the matrix $[T]$ is defined as

$$[T] = \begin{bmatrix} -ba & \frac{b}{\pi}[\sin\varphi_m - \varphi_m\cos\varphi_m] \\ b & \frac{b}{\pi}[\varphi_m - \sin\varphi_m\cos\varphi_m] \\ 0 & \frac{b}{\pi}\left[\frac{1}{1+n}\sin[(n+1)\varphi_m] + \frac{1}{n-1}\sin[(n-1)\varphi_m]\right] \\ & -\frac{2}{n}\sin(n\varphi_m)\cos\varphi_m \\ & \vdots \quad \vdots \end{bmatrix}$$

(8.16)

The system is implemented in MATLAB and the simulations resolve simultaneously the differential equations of Jonhson/Peters flexible airloads theory ((5.29) and (5.44)) and the ONERA model (equations (5.49) and (5.50)) via time marching. The results are then used as feedback to adjust the values of the loads as explained by the feedback loop of Figure (5.6). The static airfoil data are evaluated through the expressions derived in the previous Chapter 6 and are used as input for the dynamic stall model as explained in Chapter 5.

Static corrections are determined to match the slope of the experimental static lift and pitching moment curves. One of the assumption made at the beginning to validate the approach of Jonhson/Peters theory is that the loads are quasi-static. Considering this, the experimental partial derivatives of the loads can be determined in

order to calculate the appropriate corrections. The data are fitted by the least-squares method. The fitting curves obtained are

$$C_{l\,(e)} = 5.394\alpha + 1.944\beta - 0.04331 \qquad (8.17)$$

$$C_{m\,(e)} = 0.1194\alpha - 0.4719\beta + 0.007395 \qquad (8.18)$$

with a fitting error less than 4% (equation 7.3).

It is possible to obtain the corrections from the derivative of these fitting curves. For the lift force, the correction becomes

$$f_l = \frac{\frac{\partial C_{l\,(e)}}{\partial \alpha}}{\frac{\partial C_{l\,(t)}}{\partial \alpha} f_\alpha} \qquad (8.19)$$

where $f_\alpha = 1$ is a corrective factor referred to the variable α.

Following the same reasoning, the flap correction is given by

$$f_\beta = \frac{\frac{\partial C_{l\,(e)}}{\partial \beta}}{\frac{\partial C_{l\,(t)}}{\partial \beta} f_l} \qquad (8.20)$$

For the pitching moment correction the derivation becomes more difficult, because the pitching moment about the center of rotation is comprised of two components: the moment about the mid-chord and the one generated by the lift force that is applied out of the center of rotation. For this reason, a correction about the center of rotation is made in order to take into account this offset and thus obtain the overall pitching moment. Therefore, the pitching moment correction f_m must satisfy

$$f_m = \frac{\frac{\partial C_{m\,(e)}}{\partial \alpha}}{\frac{\partial C_{m\,(t)}}{\partial \alpha} f_\alpha} = \frac{\frac{\partial C_{m\,(e)}}{\partial \beta}}{\frac{\partial C_{m\,(t)}}{\partial \beta} f_\beta} \qquad (8.21)$$

From the definition of the force coefficients

$$C_{m\,(t)} = \frac{1}{2\rho u_0^2 b}(L_1 - a_c b L_0) \qquad (8.22)$$

and its derivatives are

$$\frac{\partial C_{m\,(t)}}{\partial \alpha} = \frac{1}{2\rho u_0^2 b}\left(\frac{L_1}{\partial \alpha} - a_c b \frac{L_0}{\partial \alpha}\right) \qquad (8.23)$$

$$\frac{\partial C_{m\,(t)}}{\partial \beta} = \frac{1}{2\rho u_0^2 b}\left(\frac{L_1}{\partial \beta} - a_c b \frac{L_0}{\partial \beta}\right) \qquad (8.24)$$

The four equations above can be combined to obtain the correction factors f_m and a_c. The final set of correction can be found as

$$f_\alpha = 1$$

$$f_l = 0.8584$$

$$a_c = -0.4692 \qquad (8.25)$$

$$f_\beta = 0.6497$$

$$f_m = 1.2352$$

Figures 8.5 to 8.8 show a prescribed flap oscillation as a function of the angle of attack and the C_l of NACA 0012 airfoil with this oscillating trailing edge flap. The purpose of these examples is to verify the accuracy of the airload theory with dynamic stall data taken from Reference [12]. From the Figures, it is possible to see that the simulations results fit quite well the experimental data. For Figures 8.5 and 8.6, the range of the oscillations does not give rise to dynamic stall and therefore the airload behavior is linear. The stall residual ΔC_l is zero and there is no loss in circulation due to dynamic stall. These figures were also used to validate the static correction factors derived above.

(a)

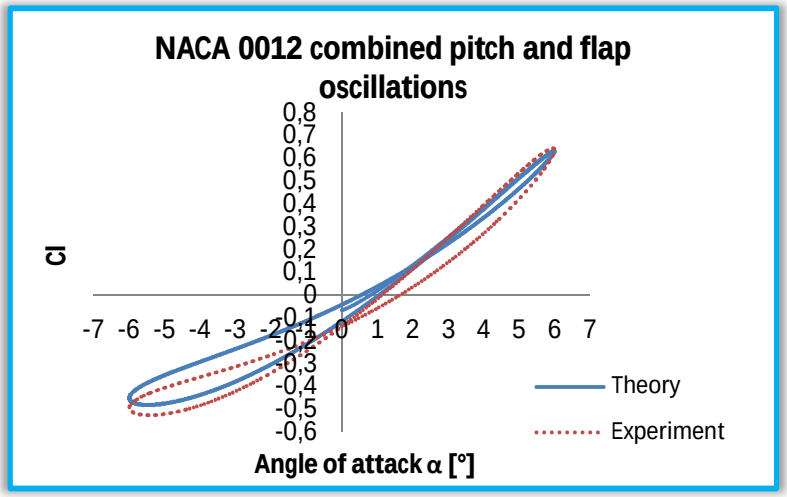

(b)

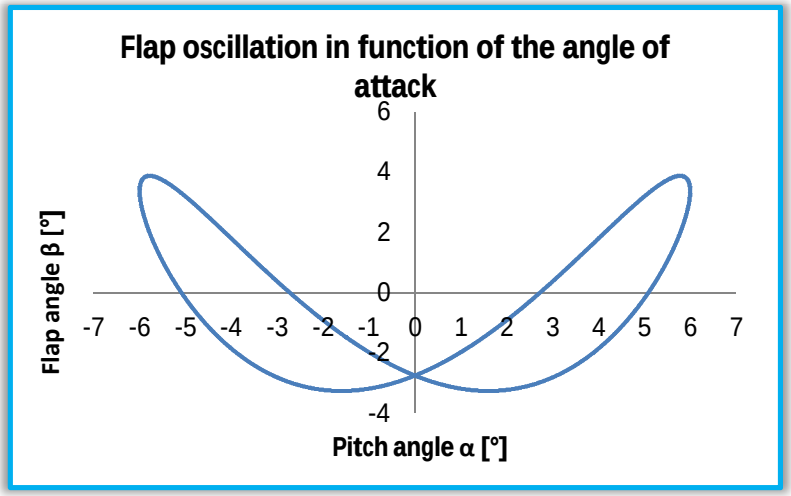

Figure 8.5: (a) Flap oscillation in function of the angle of attack and (b) coefficient of lift of NACA 0012 airfoil with oscillating trailing edge flap. Airfoil motion: $\alpha = 6°\sin(0.02\tau)$, flap motion: $\beta = 0.50° + 5.50°\sin(0.04\tau + 59°)$, M=0.4. Error norm: 0.039.

(a)

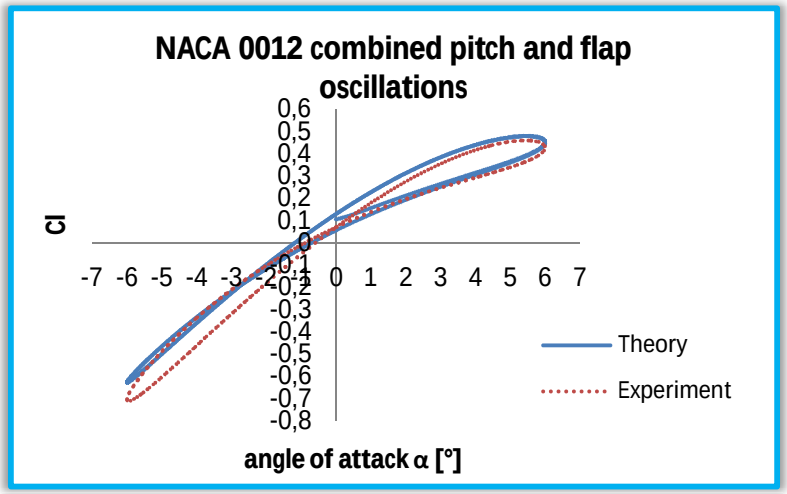

(b)

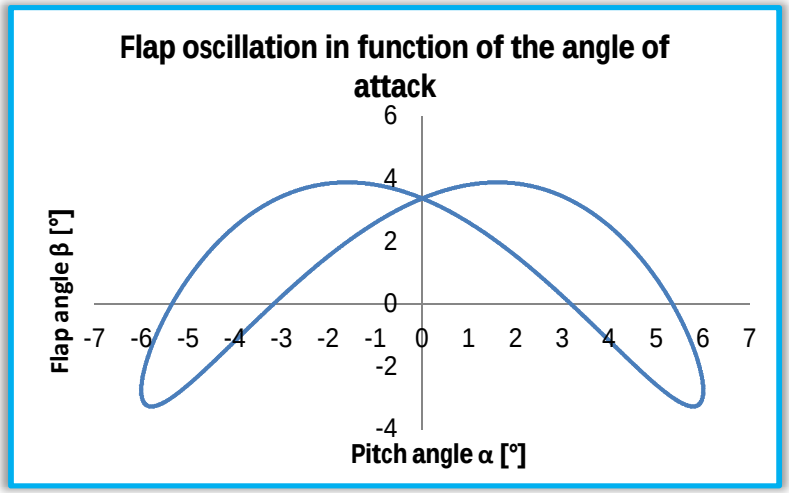

Figure 8.6: (a) Flap oscillation in function of the angle of attack and (b) coefficient of lift of NACA 0012 airfoil with oscillating trailing edge flap. Airfoil motion: $\alpha = 6°\sin(0.02\tau)$, flap motion: $\beta = 0.50° + 5.50°\sin(0.04\tau + 239°)$, M=0.4. Error norm: 0.035.

Figures 8.7 and 8.8 show that this range of oscillation gives rise to a moderate dynamic stall. The stall residuals are therefore not zero and they are used to correct the circulation as explained in Chapter 5.

(a)

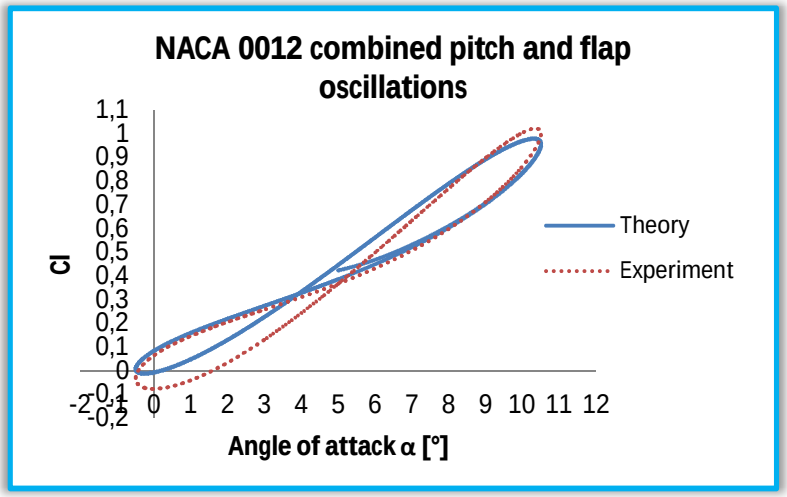

(b)

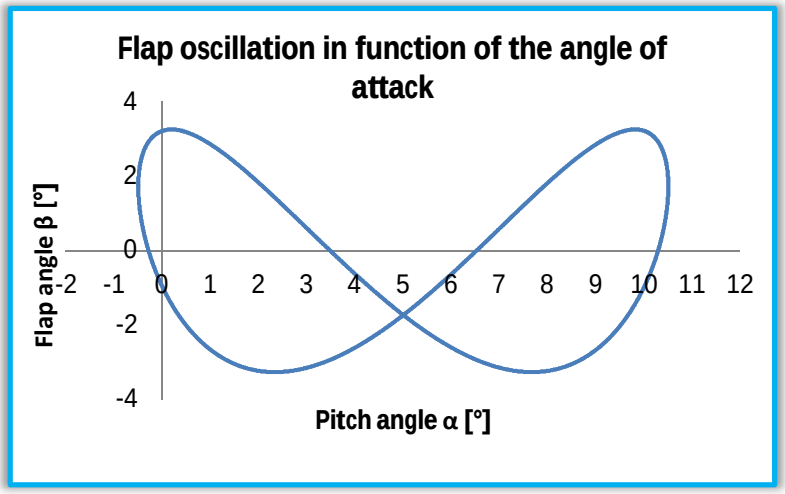

Figure 8.7: (a) Flap oscillation in function of the angle of attack and (b) coefficient of lift of NACA 0012 airfoil with oscillating trailing edge flap. Airfoil motion: $\alpha = 5° + 5.50°\sin(0.02\tau)$, flap motion: $\beta = 5°\sin(0.04\tau + 148°)$, M=0.4. Error norm: 0.036.

(a)

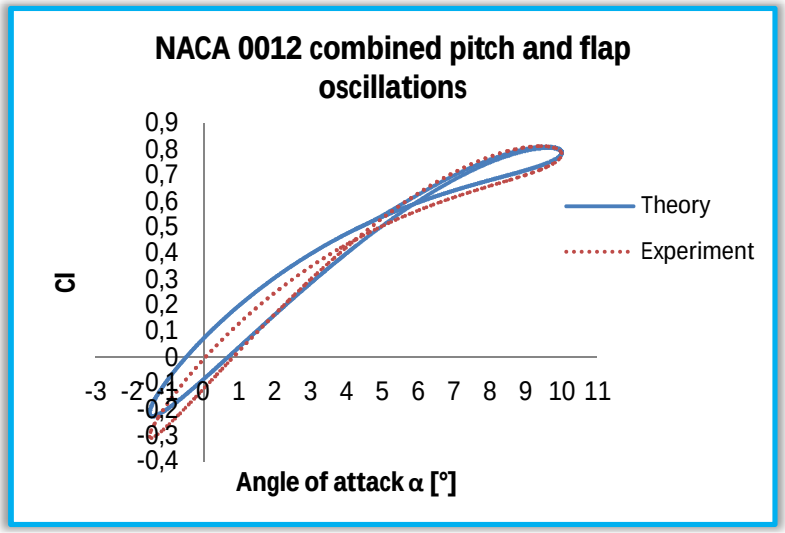

(b)

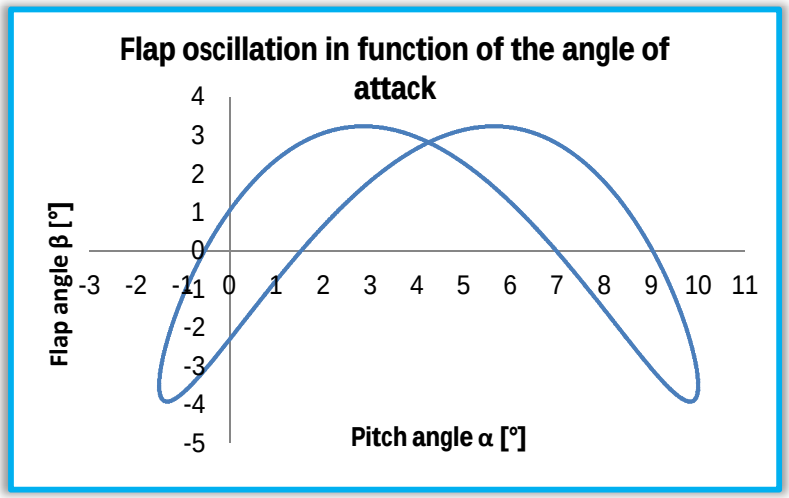

Figure 8.8: (a) Flap oscillation in function of the angle of attack and (b) coefficient of lift of NACA 0012 airfoil with oscillating trailing edge flap. Airfoil motion: $\alpha = 5.75° + 4.25°\sin(0.02\tau)$, flap motion: $\beta = -0.50° + 5.50°\sin(0.04\tau + 298°)$, M=0.4. Error norm: 0.033.

It is possible to establish that the theory is in good correlation with experimental data when moderate dynamic stall is considered. In particular, it is possible to notice that for high angles of attack (when the airfoil is subject to dynamic stall) the curves are nearly superimposed while for low angles there is a small discrepancy (always less than 4% in norm). This mismatch may be due to the fitting factor f_α that is equal to 1 and thus no significant correction is applied to the angle of attack.

9) REDUCED FREQUENCY EFFECTS IN DYNAMIC STALL WITH HARMONIC OSCILLATIONS

In this chapter are investigated the effects of the reduced frequency k in dynamic stall with harmonic oscillations. Two airfoils are considered: the NACA 0012 airfoil, which is symmetric and has no camber, and the NACA 6712 which is cambered. The aim is to compare the effect of the harmonic oscillations in cambered and not cambered airfoils. For these tests, two different motions at different reduced frequencies are choose. For a small mean angle of attack, the motion follows this expression:

$$\alpha = \alpha_m + \alpha_a \sin(k\tau) = 5° + 12° \sin(k\tau) \qquad (9.1)$$

where $k = 0.001, 0.01, 0.03, 0.05, 0.07, 0.09, 0.11 \text{ and } 0.13$ (Figure 9.1). α_a is equal to $12°$ because in this manner the angle of static stall is overshoot only by a small amount (for NACA 0012 airfoils the angle of static stall is equal to $0.293\, rad$ and the maximum angle reached with this kind of oscillation is $17° = 0.296\, rad$). The figure shows that for $k = 0.001$ the static stall curve is obtained as expected and that increasing the reduced frequency a more significant dynamic stall is obtained.

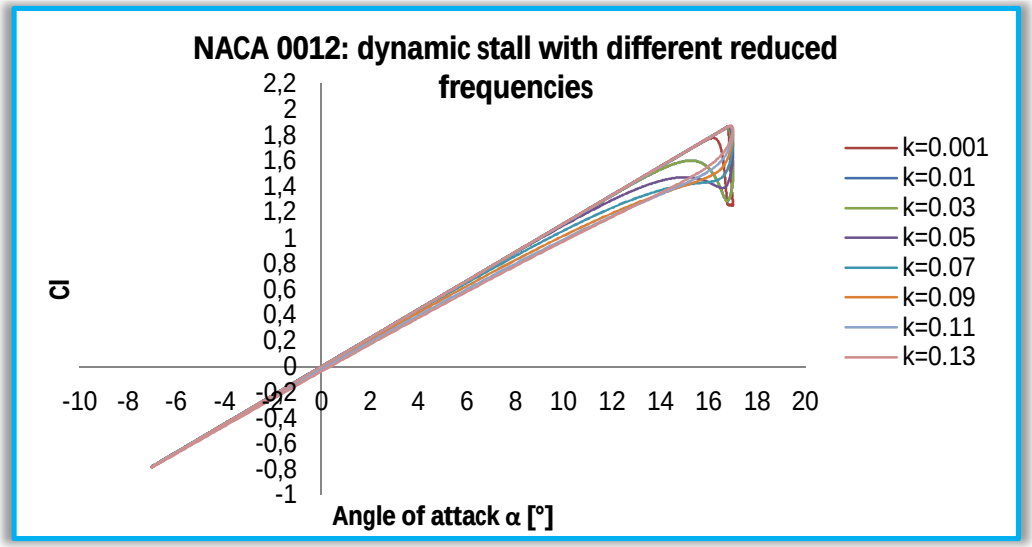

Figure 9.1: Effect of small harmonic oscillations on dynamic stall for NACA 0012 airfoil. It is important to notice the trend of the curve for $k = 0.001$ that collapse onto the static stall curve.

Figures 9.2-9.5 show the comparison between NACA 0012 and NACA 6712. Of particular interest is Figure 9.2 where it is possible to see clearly the exact match between the static and dynamic stall curves.

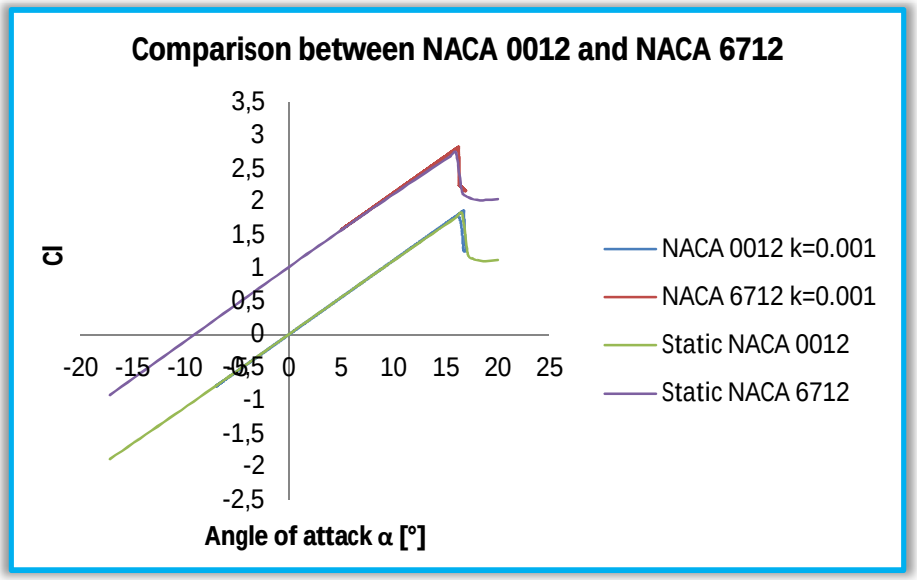

Figure 9.2: Comparison between NACA 0012 and 6712 for a reduced frequency equal to 0.001.

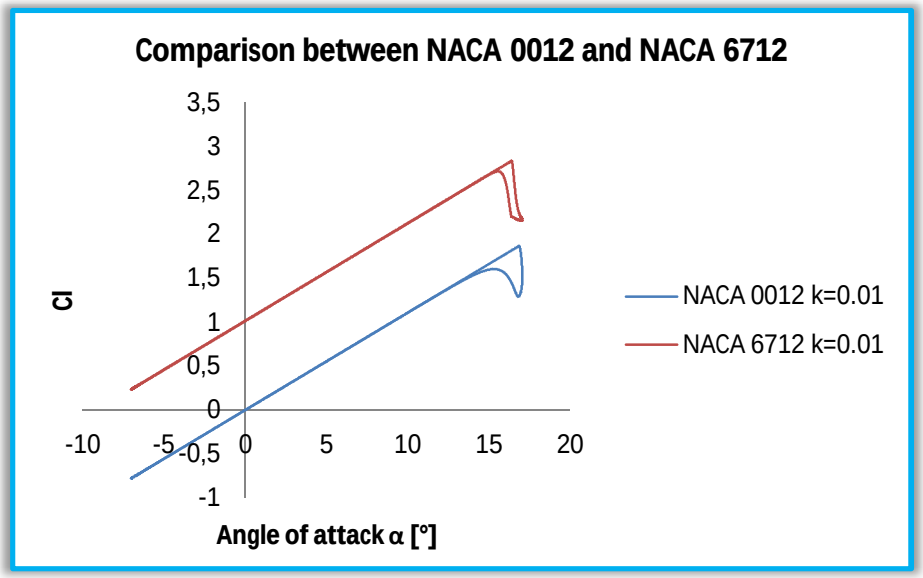

Figure 9.3: Comparison between NACA 0012 and 6712 for a reduced frequency equal to 0.01.

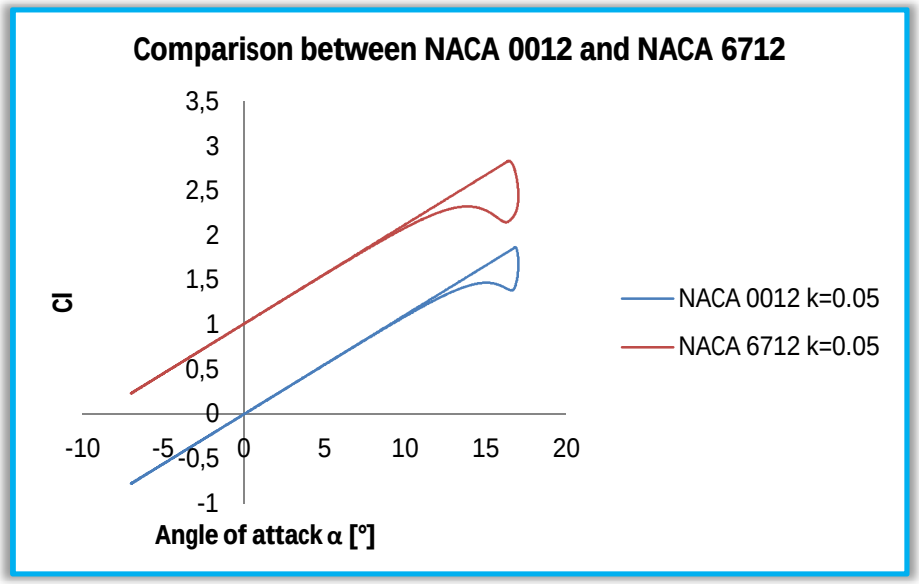

Figure 9.4: Comparison between NACA 0012 and 6712 for a reduced frequency equal to 0.05.

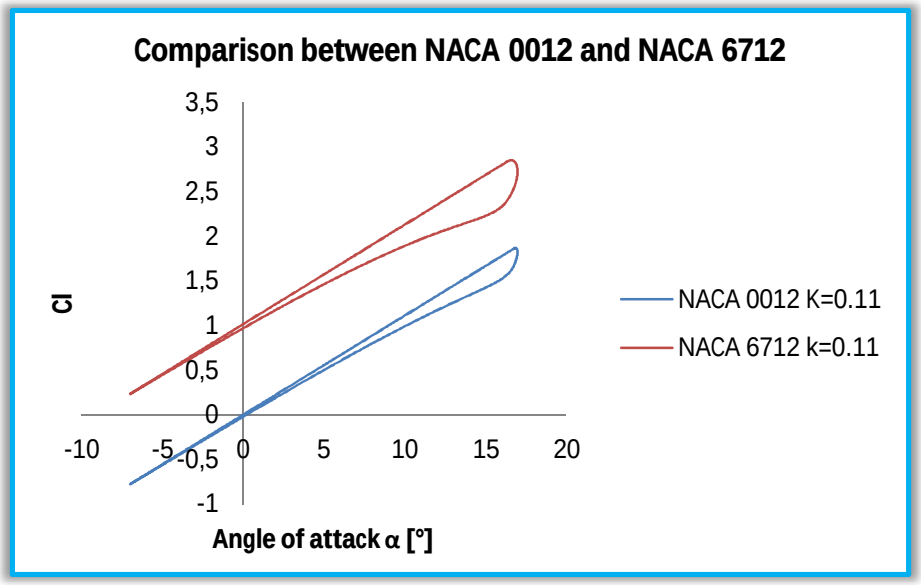

Figure 9.5: Comparison between NACA 0012 and 6712 for a reduced frequency equal to 0.11.

For bigger mean angle of attack the motion adopted is the following:

$$\alpha = \alpha_m + \alpha_a \sin(k\tau) = 10° + 12° \sin(k\tau) \qquad (9.2)$$

which permits a deep overshoot of the angle of static stall and therefore a higher dynamic stall effect (Figure 9.6).

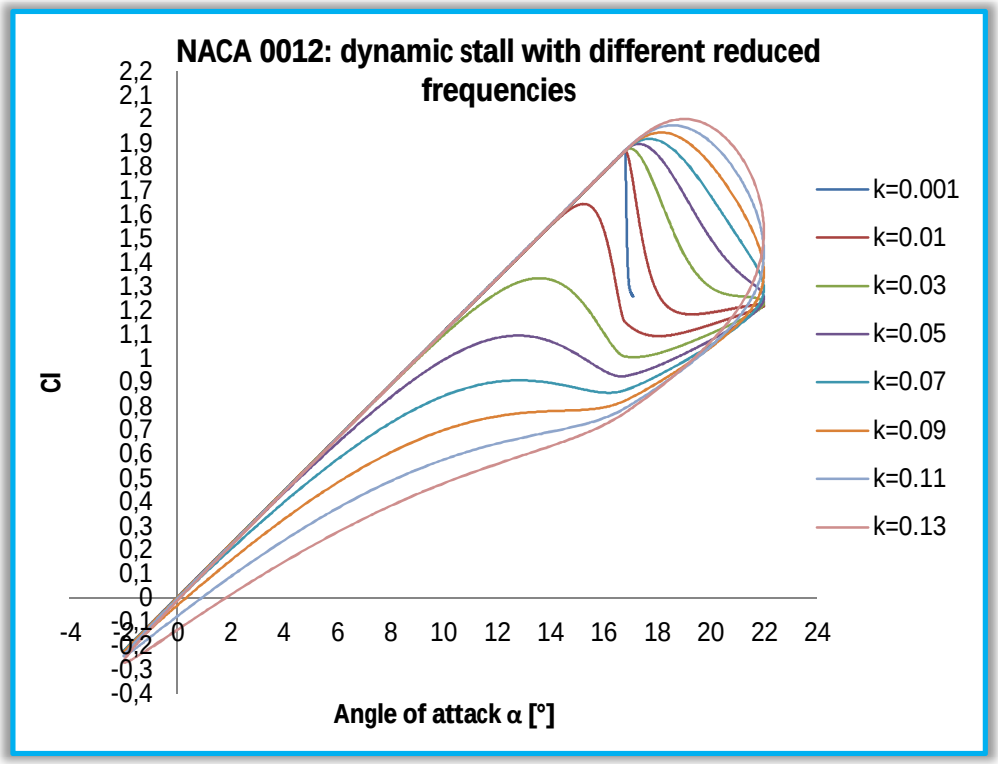

Figure 9.6: Effect of large harmonic oscillations on dynamic stall for NACA 0012 airfoil. It is important to notice the trend of the curve for k=0.001 that collapse onto the static stall curve also in this case of large oscillations.

Following the theory, for small angle of attack and small oscillations the lift coefficient does not differ from the one predicted from the thin-airfoil theory. In particular, for small angles and small reduced frequencies the trend is the same: the static stall curve and the dynamic one collapse onto each other (Figure 9.2). Only when the frequency is raised it is possible to notice a significant dynamic stall effect (Figures 9.3-9.5). Analogous results can be obtained if harmonic oscillations of large amplitude are considered, with the difference that the dynamic stall in these cases is more relevant (Figure 9.6).

10) COMPARISON BETWEEN ORIGINAL ONERA MODEL AND UNIFIED MODEL

In this section the results obtained by the implementation of the original ONERA model (Chapter 4, Reference [2]) are compared with the results obtained by the implementation of the Unified model. The aim of this chapter is to compare the C_l produced by the two different model when they are used to predict dynamic stall.

All the conditions regarding the forced motions are the same of Chapter 4 (equation 4.1). Figures 10.1, 10.2 and 10.3 show the lift coefficient in function of the pitch angle. Figure 10.1 shows that, for small oscillations, the unified model fit better the experimental data. In particular, the curve collapse onto the original ONERA model results for low angle of attack whereas it follows better the real trend for high and positive angles. This is the part where the new model fits with more accuracy the experimental data.

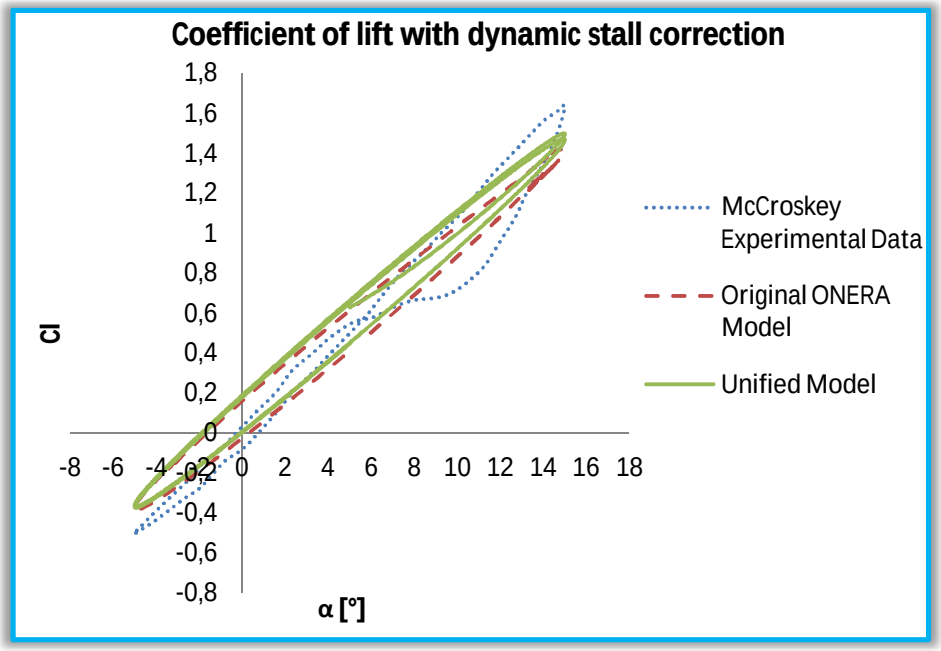

Figure 10.1: Lift coefficient comparison among McCroskey experimental data, the original ONERA model implementation and unified model implementation. The forced oscillation is $\alpha(t) = 5° + 10° sin(0.1\tau)$.

Figure 10.2 shows a better agreement between the experimental data and the unified model results. The linear part of the curve follows the experimental curve better than the original ONERA model implementation, except near the maximum C_l. In the non-linear part, the unified model matches well the experimental data. At low incidences there is no loop at the end of the cycle (from $5°$ to $0°$) and the curve matches almost exactly the real data around zero. In fact, the lift coefficient obtained from the unified model is zero for $\alpha = 0°$ as it should be from theory and following the experimental results obtained by McCroskey [9]. On the contrary this result is not obtained by the original ONERA model implementation, from which $C_l \neq 0$ when $\alpha = 0°$.

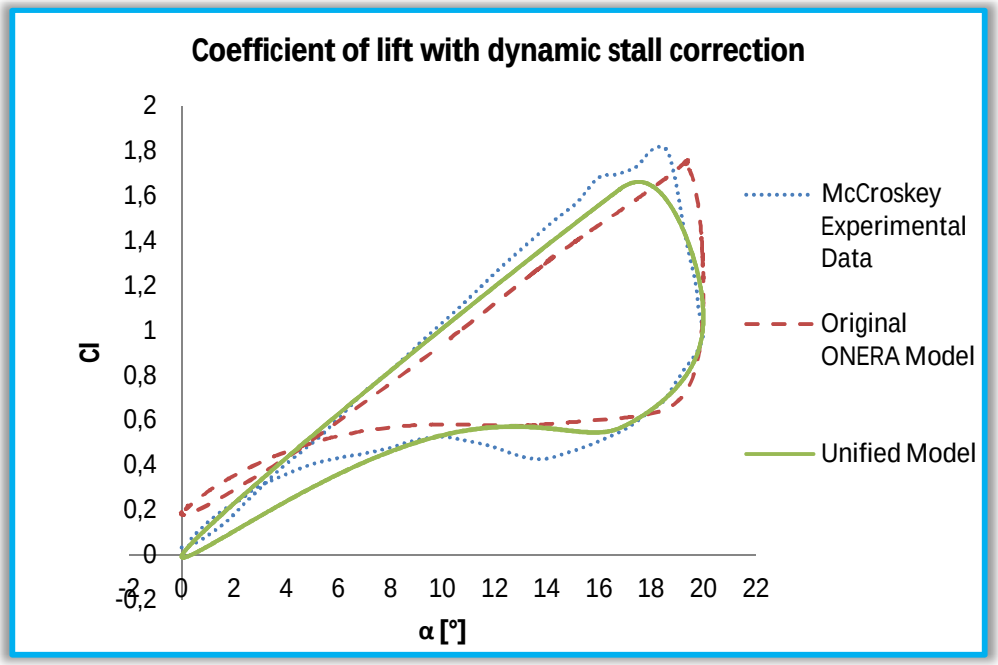

Figure 10.2: Lift coefficient comparison among McCroskey experimental data, the original ONERA model implementation and unified model implementation. The forced oscillation is $\alpha(t) = 10° + 10° \sin(0.1\tau)$.

Finally, Figure 10.3 compares the results with the experimental data for $\alpha(t) = 15° + 10° \, sin(0.1\tau)$. Here there are no significant differences between the original ONERA model and the implementation of the unified model, except if the modified ONERA model implementation by Laxman & Venkatesan (Chapter 3.3, Reference [21]) is considered (see Figure 4.1).

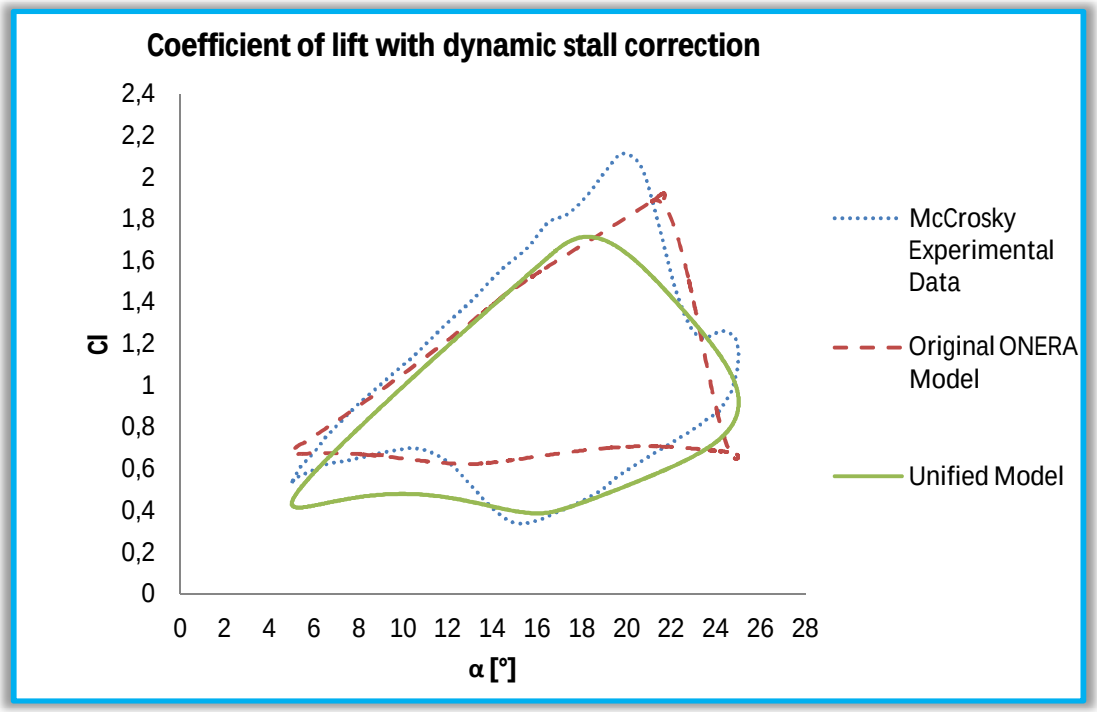

Figure 10.3: Lift coefficient comparison among McCroskey experimental data, the original ONERA model implementation and unified model implementation. The forced oscillation is $\alpha(t) = 15° + 10° \sin(0.1\tau)$.

For the moment coefficient, two forced motions are considered: $\alpha(t) = 10° + 10° \, sin(0.1t)$ in Figures 10.4, 10.5, and $\alpha(t) = 15° + 10° \, sin(0.1t)$ in Figures 10.6 and 10.7. The comparison is carried out among the moment coefficients calculated with the original ONERA model, the unified model and experimental data. For the unified model, two inflow models are considered: the one developed in Reference [13] (Figures 10.5 and 10.7) and used as the main theory in this work and the induced flow model developed by Theodorsen (Figures 10.4 and 10.6, see Appendix E for more details on Theodorsen's theory). This is possible because the ONERA model can be coupled with any desired wake model. Table 10.1 resume all cases.

Table 10.1: Cases of study for the moment coefficient with dynamic stall corrections.

Figure	Forced motion	Inflow model
Figure 10.4	$\alpha(t) = 10° + 10° \, sin(0.1t)$	Theodorsen model
Figure 10.5	$\alpha(t) = 10° + 10° \, sin(0.1t)$	Unified model [13]
Figure 10.6	$\alpha(t) = 15° + 10° \, sin(0.1t)$	Theodorsen model
Figure 10.7	$\alpha(t) = 15° + 10° \, sin(0.1t)$	Unified model [13]

Figure 10.4 shows that the theory with Theodorsen's inflow model is very similar to the original ONERA model result and it does not give a better solution.

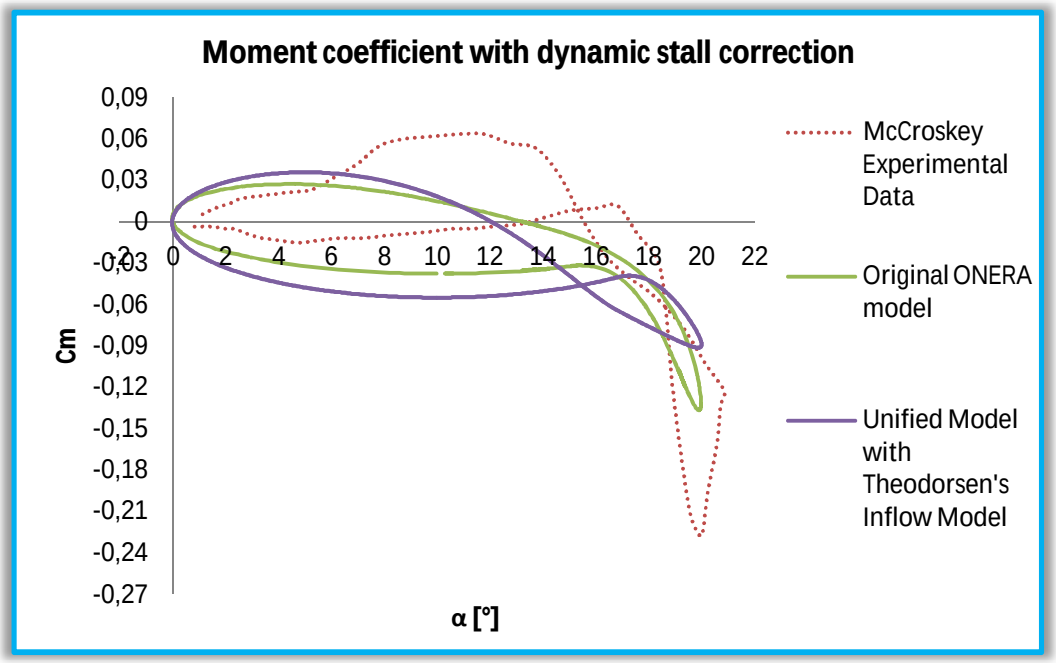

Figure 10.4: Moment coefficient comparison among McCroskey experimental data, the original ONERA model implementation and unified model implementation with Theodorsen's inflow model. The forced oscillation is $\alpha(t) = 10° + 10° \sin(0.1t)$.

On the other hand, the unified model which considers the inflow model developed in Reference [13] (Figure 10.5) has a better trend for higher angle of attack (i.e. it reaches more negative values of C_m) but it does not match the experimental data. Moreover, the trend for small angle of attack is completely wrong.

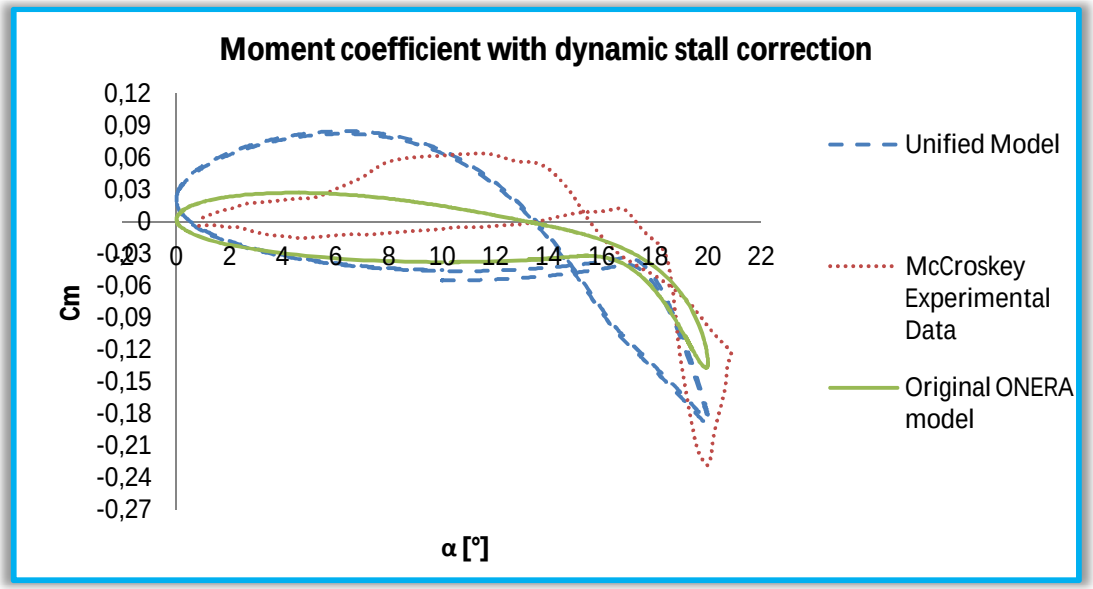

Figure 10.5: Moment coefficient comparison among McCroskey experimental data, the original ONERA model implementation and unified model implementation with the inflow model developed in Reference [13].
The forced oscillation is $\alpha(t) = 10° + 10° \sin(0.1t)$.

The same considerations can be expressed for Figures 10.6 and 10.7, even if the trends of the curves fit better the experimental data if compared with the previous example.

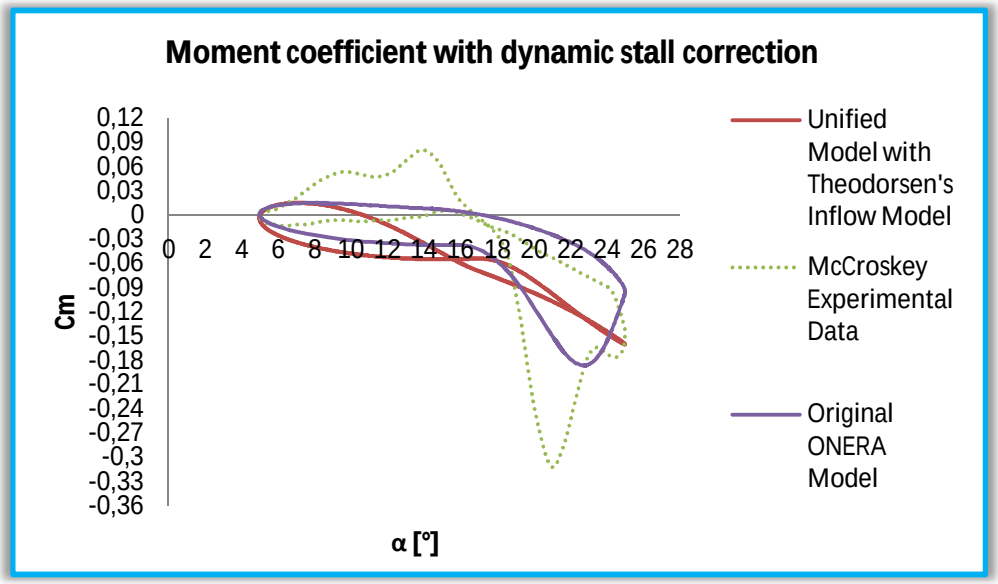

Figure 10.6: Moment coefficient comparison among McCroskey experimental data, the original ONERA model implementation and unified model implementation with Theodorsen's inflow model. The forced oscillation is $\alpha(t) = 15° + 10° \sin(0.1t)$.

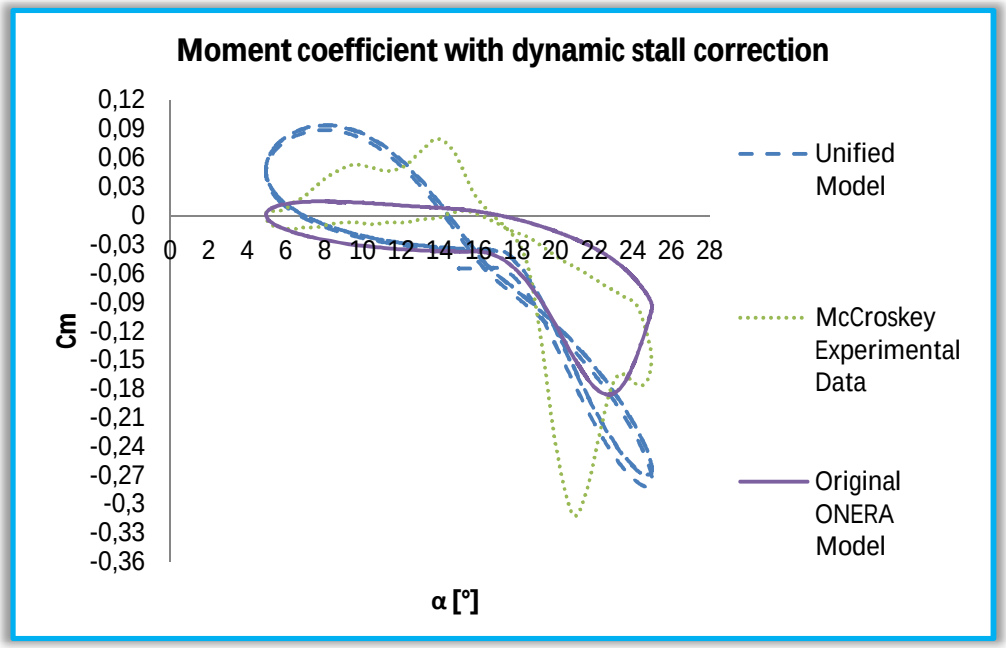

Figure 10.7: Moment coefficient comparison among McCroskey experimental data, the original ONERA model implementation and unified model implementation with the inflow model developed in Reference [13].
The forced oscillation is $\alpha(t) = 15° + 10° \sin(0.1t)$.

10.1) CONCLUSIONS

These implementations of the ONERA model are in good agreement with the experimental data only when the lift coefficient is considered: lift coefficients predictions are better than moment coefficient predictions. Furthermore, the unified model seems to provide a better agreement with experimental data than the original ONERA model implementation. An estimation of the relative error between real data curves and numerical curves can confirm this assertion and could be the topic of a future work.

For the moment coefficient is necessary a different implementation of the model because the phenomenon of the dynamic stall affects these loads in a different way. In general, it is more difficult to obtain good agreement with experimental pitching moment data because they depend on the lift, the shape of the camber line and the location of the center of pressure (Chapter 2). Experience has shown that the effective center of pressure in the thin-airfoil coordinate system may need to be adjusted slightly in order to correlate experimental moment data.

11) CONCLUSIONS AND FURTHER WORK

This thesis, following the work of Ahaus [4], presents a unified model for determining the dynamic airloads for morphing airfoils. The model is composed by three main parts:

- Johnson/Peters flexible thin-airfoil theory for the calculations of the linear loads. This theory is developed considering an inviscid, incompressible two-dimensional potential flow. All the equations are derived in terms of generalized airfoil deformations to allow the description of any general arbitrary morphing of the meanline geometry;
- an induced flow model to take into account the effect of the wake; the inflow model is based on the study of Karunamoorthy [13] which present great agreement with Theodorsen lift deficiency function when developed with eight states;
- a dynamic stall model (ONERA model) to describe accurately this phenomenon. In the present work, only the second-order ordinary differential equation is implemented to obtain the dynamic stall correction. This equation is written in terms of circulation, because it is the variation of this parameter that cause the dynamic stall.

Each component of the model is essential and is validated by correlation with classical aerodynamic theories and experimental data. In order to use ONERA dynamic stall model, the static stall residuals are computed from available static data for every airfoil considered (in this case, NACA 0012 and SC-1095). The residuals are then parameterized in terms of generalized gradients of the airfoil's meanline in order to obtain a general static database that can be adopted for any morphology of the baseline airfoil. In this manner, one needs only be able to find the gradients in terms of the morphing variables of interest to predict the corresponding lift and moment coefficients. This is the main achievement of this project: by using a general formulation (arbitrary geometry) it is possible to reproduce results for single airfoils, airfoils with flaps or airfoils with drooping leading edge both in the low and high angles of incidence.

Furthermore, the stall parameters are obtained from large-amplitude test data (instead of a large number of small-amplitude pitch

oscillations as ONERA did) with a genetic optimization algorithm. Also the angle of static stall for various combinations of morphing variables has to be extract from experimental data. This angle is crucial for the theory, because is the angle from which the dynamic stall correction is applied using the ONERA model.

Finally, the model is validated by correlation with Theodorsen results for harmonic pitch motions and harmonic trailing edge deflections. The validation is confirmed also by comparison with experimental data on dynamic stall behavior: the theory captures the essential characteristics of the phenomenon. It is important to underline that the required experimental constants to implement the theory are remarkably low. If, for example, one would calculate the dynamic stall effect on the lift and moment coefficients for a baseline airfoil, the experimental constants that has to implement are the following:

- nine constants are required to completely parameterize the baseline airfoil. In particular: two correction factors to match the theoretical lift curve and moment slopes with the data; if the lift and moment offset have to be matched as well, other two shift terms have to be added in the residual formulation; to implement the dynamic stall model, other five constants are required. Therefore, the final number of experimental constants for the baseline airfoil is 9.

- considering the N_M morphing variables introduced into the airfoil with N_L required morphing loads. In the linear region Johnson/Peters theory can fit experimental data by using one correction factor for the pitching moment, one for each morphing variable and one for each morphing load. Therefore the correction factors are $1 + N_M + N_L$. In addition, for the morphed airfoil, another angle is needed in order to apply the theory. This angle is function of the generalized gradients of the airfoil's meanline and so other two additional constants are needed. The total number of constants is then $N_M + N_L + 3$.

If one morphing variable and two morphing loads are considered, only fourteen constants are required to analyze dynamic stall.

The results presented here show that the proposed methods can predict with reasonable accuracy the behavior of morphing airfoils in dynamic stall from their static aerodynamic characteristics. There are many directions that can be choose from this point.

- Implementation of the flutter behavior in order to discover the realms of aeroelastic stability and instability of this phenomenon.

Some investigations relatively the linear regime on flexible airfoils have been made by J. Murua, R. Palacios and J. Peirò [17] but there are no information about the stall regime. This could be an interesting direction to follow.

- Flutter (linear) analysis for cambered airfoils with further degrees of freedom.

- Application to stall flutter. Nothing has been done beyond pitch and plunge.

- Optimal parameters of the model and study of sensitivity of the model response to the variations in the parameters. Do the parameters change significantly within airofoils?

- Incorporation of the model into a 3D simulation (for example, into blade-element momentum theory).

- Characterization of other airfoils used in rotorcraft. All the steps executed here for the NACA 0012 and SC-1095 can be followed to study other airfoils.

APPENDIX A: MATRICES AND VECTORS FOR THE UNIFIED MODEL

This appendix define the matrices an vectors used in the formulation of the unified model. *M* refers to the numbers of states in the Glauert expansion and thus the matrices and vectors are of the following form:

$$(M + 1) \times (M + 1) \text{ and } (M + 1) \times 1.$$

N refers to the numbers of inflow states and, as said in Chapter 5.1 for the numbers of coefficients $\lambda_0, \dots, \lambda_N$, the matrices and vectors are in the following form:

$$(N \times N) \text{ and } N \times 1$$

The vectors used are

$\{1\} = \{1\ 0\ 0\ 0\ 0\ \dots\}^T$

$\{b_n\} = \{b_1\ b_2\ b_3\ b_4\ b_5 \dots\ b_N\}^T$

$\{d\} = \left\{\frac{1}{2}\ 0\ 0\ 0\ 0 \dots\right\}^T$

$\{e\} = \left\{1\ \frac{1}{2}\ 0\ 0\ 0 \dots\right\}^T$

$\{f\} = \{0\ 1\ 2\ 3\ 4 \dots\ M\}^T$

$\{h_n\} = \{h_1\ h_2\ h_3\ h_4\ h_5\ \dots\ h_M\}^T$

$\{v_n\} = \{v_0\ v_1\ 0\ 0\ 0\ \dots\}^T$

$\{\dot{v}_n + \ddot{h}_n\} = \{\dot{v}_0 + \ddot{h}_0\ \dot{v}_1 + \ddot{h}_1\ 0\ 0\ 0 \dots\}^T$

$\{\lambda_0\} = \{\lambda_0\ 0\ 0\ 0\ 0\ \dots\}^T$

$\{\lambda_1\} = \{\lambda_0\ \lambda_1\ 0\ 0\ 0\ \dots\}^T$

The matrices used are

$$[A] = \left[D + \{d\}\{b\}^T + \{c\}\{d\}^T + \frac{1}{2}\{c\}\{b\}^T\right]$$

$$[C] = \begin{bmatrix} f & 1 & 0 & 0 & 0 & \cdots \\ -\frac{1}{2} & 0 & \frac{1}{2} & 0 & 0 & \cdots \\ 0 & -\frac{1}{2} & 0 & \frac{1}{2} & 0 & \cdots \\ 0 & 0 & -\frac{1}{2} & 0 & \frac{1}{2} & \ddots \\ 0 & 0 & 0 & -\frac{1}{2} & 0 & \ddots \\ \vdots & \vdots & \vdots & \ddots & \ddots & \ddots \end{bmatrix}$$

$$[D] = \begin{bmatrix} 0 & -\frac{1}{2} & 0 & 0 & \cdots & 0 \\ \frac{1}{4} & 0 & -\frac{1}{4} & 0 & \cdots & 0 \\ 0 & \frac{1}{6} & 0 & -\frac{1}{6} & \ddots & 0 \\ 0 & 0 & \frac{1}{8} & \ddots & \ddots & 0 \\ \vdots & \vdots & \ddots & \ddots & 0 & \ddots \\ 0 & 0 & 0 & 0 & \frac{1}{2N} & 0 \end{bmatrix}$$

$$[G] = \begin{bmatrix} 0 & \frac{1}{2} & 0 & 0 & 0 & \cdots \\ 0 & 0 & \frac{1}{4} & 0 & 0 & \cdots \\ 0 & -\frac{1}{4} & 0 & \frac{1}{4} & 0 & \cdots \\ 0 & 0 & -\frac{1}{4} & 0 & \frac{1}{4} & \ddots \\ 0 & 0 & 0 & -\frac{1}{4} & 0 & \ddots \\ \vdots & \vdots & \vdots & \ddots & \ddots & \ddots \end{bmatrix}$$

$$[H] = \begin{bmatrix} 0 & 0 & 0 & 0 & 0 & \cdots \\ 0 & \frac{1}{2} & 0 & 0 & 0 & \cdots \\ 0 & 0 & \frac{2}{2} & 0 & 0 & \cdots \\ 0 & 0 & 0 & \frac{3}{2} & 0 & \cdots \\ 0 & 0 & 0 & 0 & \frac{4}{2} & \cdots \\ \vdots & \vdots & \vdots & \vdots & \vdots & \ddots \end{bmatrix}$$

$$[K] = \begin{bmatrix} 0 & f & 2 & 3f & 4 & \cdots \\ 0 & -\frac{1}{2} & 0 & 0 & 0 & \cdots \\ 0 & 0 & -\frac{2}{2} & 0 & 0 & \cdots \\ 0 & 0 & 0 & -\frac{3}{2} & 0 & \ddots \\ 0 & 0 & 0 & 0 & \ddots & \ddots \\ \vdots & \vdots & \vdots & \vdots & \ddots & -\frac{M}{2} \end{bmatrix}$$

$$[M] = \begin{bmatrix} \frac{1}{2} & 0 & -\frac{1}{4} & 0 & 0 & \cdots \\ 0 & \frac{1}{16} & 0 & -\frac{1}{16} & 0 & \cdots \\ -\frac{1}{4} & 0 & \frac{1}{6} & 0 & \ddots & \ddots \\ 0 & -\frac{1}{16} & 0 & \ddots & 0 & \ddots \\ 0 & 0 & \ddots & 0 & \ddots & \ddots \\ \vdots & \vdots & \ddots & -\frac{1}{8M} & \vdots & \frac{M}{4(M^2-1)} \end{bmatrix}$$

$$[S] = \begin{bmatrix} f & 0 & 0 & 0 & 0 & \cdots \\ 0 & 0 & 0 & 0 & 0 & \cdots \\ 0 & 0 & 0 & 0 & 0 & \cdots \\ 0 & 0 & 0 & 0 & 0 & \cdots \\ 0 & 0 & 0 & 0 & 0 & \cdots \\ \vdots & \vdots & \vdots & \vdots & \vdots & \ddots \end{bmatrix}$$

where f is the reversed flow parameter (equal to 1 in the present work).

APPENDIX B: SPATIAL GRADIENT COMPONENTS

This appendix define the spatial gradients for a NACA four digit airfoil.As discussed in Chapter 6.3, the NACA 0012 airfoil is a four digit airfoil. In the designation, every digit has a meaning that recalls the characteristics of the airfoil. For four digits airfoils the equation of the meanline is known in closed form as

$$\frac{y_{meanline}}{c} = \begin{cases} \left(\frac{m}{p^2}\right)[2p\bar{x} - \bar{x}^2] & 0 \le \bar{x} \le p \\ \left[\frac{m}{(1-p)^2}\right][1 - 2p + 2p\bar{x} - \bar{x}^2] & p < \bar{x} \le 1 \end{cases}$$

$$(B.1)$$

where

$$m = 0.01\bar{m} \qquad p = 0.1\bar{p} \qquad q = 2p - 1$$

$$\bar{x} = \frac{\left(1 + \frac{x}{b}\right)}{2} \qquad (B.2)$$

The expression above is defined for $\bar{x} = [0,1]$ but for the thin-airfoil theory the mean line has to be defined on the interval $x = [-b, b]$. The variables have to be transformed accordingly. The transformation is

$$x = b(2\bar{x} - 1), \qquad b = \frac{c}{2} \qquad (B.3)$$

and the new expressions for the mean line are

$$\frac{y_{meanline}}{c} = \begin{cases} \frac{2m}{b^2(1+q)^2}[b^2(1 + 2q) + 2bqx - x^2] & -b \le x \le qb \\ \frac{2m}{b^2(1-q)^2}[b^2(1 - 2q) + 2bqx - x^2] & qb < x \le b \end{cases}$$

$$(B.4)$$

Since $h \equiv -y_{meanline}$, also the spatial gradient is calculated in closed form as

$$\frac{\partial h}{\partial x} = \begin{cases} \dfrac{4m(x - bq)}{b(1 + q)^2} & -b \le x \le qb \\ \dfrac{4m(x - bq)}{b(1 - q)^2} & qb < x \le b \end{cases} \qquad (B.5)$$

and with the Glauert change of variable, $x = b\cos\varphi$, the final form of the spatial gradient is

$$\frac{\partial h}{\partial x} = \begin{cases} \dfrac{4m(\cos\varphi - q)}{(1 - q)^2} & 0 \le \varphi \le \varphi_b \\ \dfrac{4m(\cos\varphi - q)}{(1 + q)^2} & \varphi_b < \varphi \le \pi \end{cases} \qquad (B.6)$$

where φ_b is the Glauert variable evaluated at q. In this form, the gradient can be integrated to solve for the Glauert expansions coefficients. The first four terms are

$$h_0' = \frac{1}{\pi}\int_0^{\pi} \frac{\partial h}{\partial x} d\varphi$$

$$= \frac{4mq}{(1 - q^2)^2}\left[\frac{4}{\pi}(qsin^{-1}q + \sqrt{1 - q^2}) - (1 + q^2)\right] \qquad (B.7)$$

$$h_1' = \frac{2}{\pi}\int_0^{\pi} \frac{\partial h}{\partial x}\cos\varphi \, d\varphi$$

$$= \frac{4m}{(1 - q^2)^2}\left[(1 + q^2) - \frac{4}{\pi}(qsin^{-1}q + q^2\sqrt{1 - q^2})\right]$$

$$(B.8)$$

$$h_2' = \frac{2}{\pi}\int_0^{\pi} \frac{\partial h}{\partial x}\cos\varphi \, 2d\varphi = \frac{32m}{3\pi}\frac{q}{\sqrt{1 - q^2}} \qquad (B.9)$$

$$h_3' = \frac{2}{\pi}\int_0^{\pi} \frac{\partial h}{\partial x}\cos 3\varphi \, d\varphi = \frac{32m}{3\pi}\frac{q^2}{\sqrt{1 - q^2}} \qquad (B.10)$$

APPENDIX C: MEAN LINE EXPANSION FOR THE TRAILING EDGE AND LEADING EDGE DROOP

This appendix explains how to derive a simple closed form expression for a parabolic leading or trailing edge droop, like the one adopted to obtain the mean line of the SC-1095 airfoil. In fact, only the mean line of the airfoil is needed for the airloads calculation in this theory. This geometry is similar to the one adopted in Reference [7] in which the authors deflect the leading edge and the trailing edge of the airfoil by fitting a parabola to the main mean line. The new shape is defined by two angles, θ_{LE} and δ_{TE}, that represent respectively the angle deflection of the leading and trailing edges. The angles are measured from the leading or trailing edge to the initiation point of the droop and the deflections are easily derived as

$$y = -\frac{\theta_{LE}}{b}\frac{(x + eb)^2}{1 - e} \qquad -b \le x \le -eb \quad \text{leading} - \text{edge droop} \quad (C.1)$$

$$y = -\frac{\delta_{TE}}{b}\frac{(x - db)^2}{1 - d} \qquad db \le x \le b \quad \text{trailing} - \text{edge droop} \quad (C.2)$$

The slope of the mean line becomes

$$\frac{dy}{dx} = \begin{cases} \dfrac{-2\theta_{LE}\left(\dfrac{x}{b} + e\right)}{1 - e} & -b \le x < -be \\ 0 & -be \le x \le bd \\ \dfrac{-2\delta_{TE}\left(\dfrac{x}{b} - d\right)}{1 - d} & bd < x \le b \end{cases} \qquad (C.3)$$

with $0 \le e \le 1$ and $0 \le d \le 1$.

The generalized deformations h_n and the generalized spatial gradients h_n' can be calculated as

$$h_0 = -\frac{1}{\pi}\int_0^{\pi} y(\varphi)d\varphi \qquad (C.4)$$

$$h_n = -\frac{2}{\pi}\int_0^{\pi} y(\varphi)\cos(n\varphi)\,d\varphi \qquad n \geq 1 \qquad (C.5)$$

$$h_0' = -\frac{1}{\pi}\int_0^{\pi} \frac{dy(\varphi)}{dx}\,d\varphi \qquad (C.6)$$

$$h_n' = -\frac{2}{\pi}\int_0^{\pi} \frac{dy(\varphi)}{dx}\cos(n\varphi)\,d\varphi \qquad n \geq 1 \qquad (C.7)$$

The resultant integrals are

$$h_0 = \frac{b\delta_{TE}}{2\pi(1-d)}\left[(1+2d^2)\cos^{-1}d - 3d\sqrt{1-d^2}\right] + \frac{b\theta_{LE}}{2\pi(1-e)}\left[(1+2e^2)\cos^{-1}e - 3e\sqrt{1-e^2}\right] \qquad (C.8)$$

$$h_1 = \frac{2b\delta_{TE}}{3\pi(1-d)}\left[-3d\cos^{-1}d + (2+d^2)\sqrt{1-d^2}\right] + \frac{2b\theta_{LE}}{3\pi(1-e)}\left[3e\cos^{-1}e - (2+e^2)\sqrt{1-e^2}\right] \qquad (C.9)$$

$$h_2 = \frac{b\delta_{TE}}{6\pi(1-d)}\left[3\cos^{-1}d + (5-2d^2)d\sqrt{1-d^2}\right] + \frac{b\theta_{LE}}{6\pi(1-e)}\left[3\cos^{-1}e - (5-2e^2)e\sqrt{1-e^2}\right] \qquad (C.10)$$

$$h_n = Q_1\Big\{[1-n^2 + d^2(2+n^2)]\sin(n\cos^{-1}d) 3d\sqrt{1-d^2}\,n\cos(n\cos^{-1}d)\Big\} + Q_2\Big\{[1-n^2+e^2(2+n^2)]\sin(n\cos^{-1}e) - 3e\sqrt{1-e^2}\,n\cos(n\cos^{-1}e)\Big\} \qquad n \geq 3 \qquad (C.11)$$

with

$$Q_1 = \frac{4b\delta_{TE}}{n\pi(1-d)(n^2-4)(n^2-1)} \qquad (C.12)$$

$$Q_2 = \frac{4b\theta_{LE}(-1)^n}{n\pi(1-d)(n^2-4)(n^2-1)} \qquad (C.13)$$

and

$$h_0' = \frac{2\delta_{TE}}{\pi(1-d)}\left[-d\cos^{-1}d + \sqrt{1-d^2}\right] + \frac{2\theta_{LE}}{\pi(1-e)}\left[e\cos^{-1}e - \sqrt{1-e^2}\right] \qquad (C.14)$$

$$h_1' = \frac{2\delta_{TE}}{\pi(1-d)}\left[\cos^{-1}d - d\sqrt{1-d^2}\right] + \frac{2\theta_{LE}}{\pi(1-e)}\left[\cos^{-1}e - e\sqrt{1-e^2}\right] \qquad (C.15)$$

$$h_n' = \frac{4\delta_{TE}}{n\pi(1-d)(n^2-1)}\left\{d\sin(n\cos^{-1}d) - n\sqrt{1-d^2}\cos(n\cos^{-1}d)\right\} + \frac{4\theta_{LE}}{n\pi(1-e)(n^2-1)}\left\{e\sin(n\cos^{-1}e) + (-1)^n n\sqrt{1-e^2}\cos(n\cos^{-1}e)\right\} \qquad n \geq 2 \qquad (C.16)$$

APPENDIX D: TIME DERIVATIVE OF STALL RESIDUALS

This appendix illustrates the method to calculate the total derivative of the stall residuals, which are used in the second order differential equation in ONERA model. From Chapter 6.3, where the static stall residuals are presented, it is possible to see the dependence on α, α_{0l} and α_{shift} which in turn are functions of both h_n' and z.

The total derivative is therefore

$$\frac{d(\Delta C_n)}{dt} = \frac{\partial(\Delta C_n)}{\partial z}\frac{dz}{dt} = \frac{\partial(\Delta C_n)}{\partial z}\left[\frac{\partial z}{\partial \alpha}\frac{d\alpha}{dt} + \frac{\partial z}{\partial h_0'}\frac{dh_0'}{dt} + \frac{\partial z}{\partial h_1'}\frac{dh_1'}{dt} + \cdots\right] \qquad (D.1)$$

Now the process will be illustrate considering NACA 0012 airfoil. From Chapter 6.3.1 the variable z and the expression of ΔC_l are given by

$$z = \alpha - \alpha_{ss} = \alpha - 0.293 + 0.870h_0' + 0.099h_1' - 0.490h_2' \qquad (D.2)$$

$$\Delta C_l = 0.2689\tan^{-1}(54.54z) + 15.89(z + 0.3192)^4 + 0.4070 \qquad (D.3)$$

and thus the total derivative of z and the partial derivative of ΔC_l are

$$\frac{dz}{dt} = \frac{d\alpha}{dt} + 0.870\frac{dh_0'}{dt} + 0.099\frac{dh_1'}{dt} - 0.490\frac{h_2'}{dt} \qquad (D.4)$$

$$\frac{\partial(\Delta C_l)}{\partial z} = \frac{14.67}{1 + 2975z^2} + 63.56(z + 0.3192)^3 \qquad (D.5)$$

Finally, from the latest two expressions, it is possible to obtain the total derivative of the residuals

$$\frac{d(\Delta C_n)}{dt} = \frac{\partial(\Delta C_n)}{\partial z}\frac{dz}{dt} = \left(\frac{14.67}{1 + 2975z^2} + 63.56(z + 0.3192)^3\right)\left[\frac{d\alpha}{dt} + 0.870\frac{dh_0'}{dt} + 0.099\frac{dh_1'}{dt} - 0.490\frac{h_2'}{dt}\right] \qquad (D.6)$$

If a morphing variable is used, like a flap with the deflection characterized by the angle β, this total derivative can be written alternatively in terms of this variable obtaining

$$\frac{d(\Delta C_n)}{dt} = \frac{\partial(\Delta C_n)}{\partial z}\frac{dz}{dt}$$
$$= \left(\frac{14.67}{1 + 2975z^2} + 63.56(z + 0.3192)^3\right)\left[\frac{d\alpha}{dt}\right.$$
$$\left. + \left(0.870\frac{\partial h_0'}{d\beta} + 0.099\frac{\partial h_1'}{d\beta} - 0.490\frac{\partial h_2'}{d\beta}\right)\frac{d\beta}{dt}\right] \qquad (D.7)$$

For an airfoil with a trailing edge flap the first three terms of the partial derivatives $\partial h_n'/\partial\beta$ are

$$\frac{\partial h_0'}{d\beta} = \frac{1}{\pi}\cos^{-1} d \qquad (D.8)$$

$$\frac{\partial h_1'}{d\beta} = \frac{2}{\pi}\sqrt{1 - d^2} \qquad (D.9)$$

$$\frac{\partial h_2'}{d\beta} = \frac{2}{\pi}d\sqrt{1 - d^2} \qquad (D.10)$$

APPENDIX E: THEODORSEN AND GARRICK AERODYNAMIC THEORY

This chapter presents the original theories developed by Theodorsen/Garrick that confirm the unsteady airloads theory developed by Peters. A thin oscillating deformable airfoil is considered here and the aerodynamic loads are derived. The presentation here follows the work of W. P. Walker [6].

E.1) LIFT DERIVATION

Theodorsen's method for thin oscillating airfoils is based on ideal flow in two dimensions. The flow is composed by two main parts: the flow due to the presence of the airfoil in the flow, also known as the flow due to the circulation around the airfoil, and the flow due to the vortices in the wake (Appendix F). These components of the flow are elementary flow solutions to Laplace's equation and their sum is still a solution to this equation. Laplace's equation is

$$\nabla^2\phi = 0 \qquad (E.1)$$

where ϕ is the velocity potential.

The airloads model is developed for a flat plate. The non-circulatory flow (the flow due to the presence of the airfoil in the flow) is developed with a source-sink pair distributed along the chord. The strength of the sheet is obtained by the imposition of the boundary condition: the absence of flow through the surface of the airfoil. Similarly, the circulatory flow (the flow due to the wake) is developed by using a vortex sheet on the airfoil and in the wake which extends to infinity. The strength of this sheet is obtained by the imposition of the Kutta condition: the flow must leave the trailing edge smoothly.

E.2) AIRFOIL SHAPE

The airfoil motion is represented by plunge, pitch and different forms of camber shapes. These last shapes are obtained by using Chebyshev orthogonal polynomials, which permit the representation of

any deformed shape by considering enough polynomials in the solution. These polynomials are chosen to guarantee the verification between this theory and Peters's one (Chapter 5), that uses Chebyshev polynomials too, but it is not compulsory: any set of orthogonal polynomials could be chosen. In general, Chebyshev polynomials are given as

$$T_0(x) = 1$$

$$T_1(x) = x \qquad (E.2)$$

$$T_{n+1}(x) = 2xT_n(x) - T_{n-1}(x)$$

where x is the non-dimensional variable along the chord that varies from -1 at the leading edge to 1 at the trailing edge. The first five polynomials, that are used for the development of this theory, are given below and shown in Figure E.1. Note that the first three are the same derived in Peters theory:

$$T_0(x) = 1$$

$$T_1(x) = x$$

$$T_2(x) = 2x^2 - 1 \qquad (E.3)$$

$$T_3(x) = 4x^3 - 3x$$

$$T_4(x) = 8x^4 - 8x^2 + 1$$

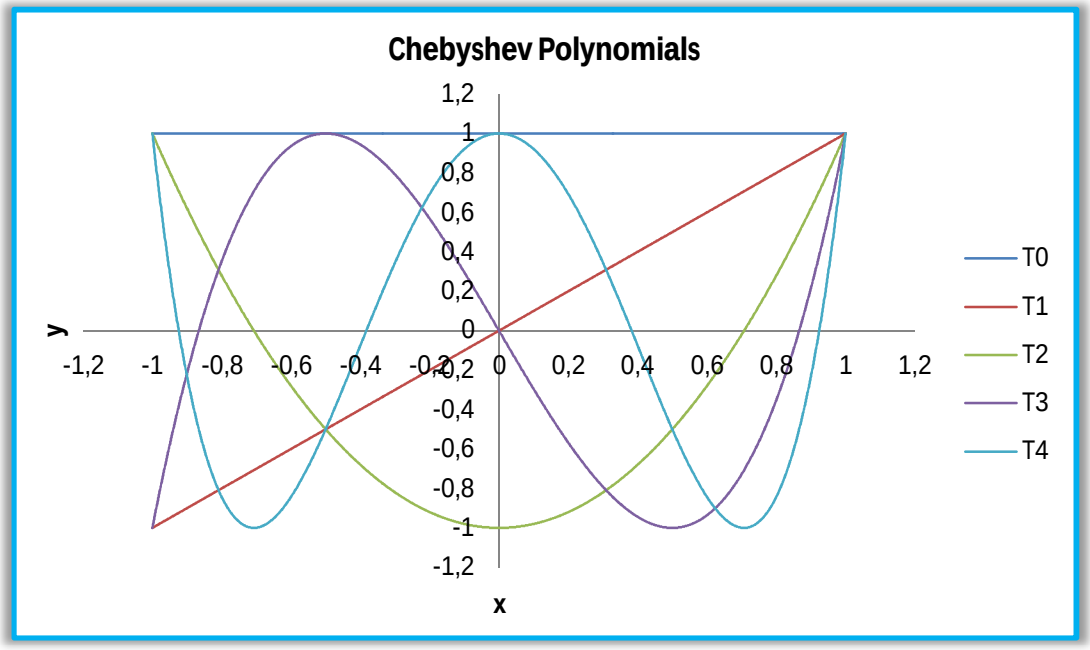

Figure E.1: Chebyshev polynomials.

The first Chebyshev polynomial is a constant in space and it represents the vertical displacement, plunge. The second polynomial represents a linear function which can be associated to the flat plate subjected to an angle of attack, pitch. From the third polynomial onwards the functions are no more linear: these polynomials represents the camber's deformations. It is possible to obtain a generalized airfoil shape in terms of Chebyshev polynomials as

$$y(x) = A_0 T_0(x) + A_1 T_1(x) + A_2 T_2(x) + \cdots + A_n T_n(x) + \cdots + A_N T_N(x) \qquad (E.4)$$

where the A_n's are the magnitude of each polynomial contributing to the complete airfoil shape. The A_n's can be related to the usual airfoil variables, such as h for plunge and α for pitch. In this manner it is possible to obtain

$$y(x,t) = \frac{h}{b} T_0(x) + \alpha T_1(x) + \frac{bk_1}{4} T_2(x) + \frac{b^2 k_2}{24} T_3(x) + \frac{b^3 k_3}{192} T_4(x) + \cdots + A_N(t) T_N(x) \qquad (E.5)$$

where the k_n's coefficients are the curvature variables of the airfoil and b is the semi-chord. The A_n's are written in terms of the physically relevant deformation variables by adding a scaling factor corresponding to the highest nonzero derivative (the terms that multiply the Chebyshev polynomials):

$$A_n = \frac{b^{n-1}}{\frac{\partial^n T_n}{\partial x^n}} \frac{\partial^n y_n}{\partial x^n} \qquad (E.6)$$

E.3)LIFT DUE TO THE NON-CIRCULATORY FLOW

As it has been said previously (Chapter E.1) the non-circulatory lift is developed using a source-sink pair distributed along the chord. The velocity potential due to a source or a sink $\phi_{s/s}$ is given by

$$\phi_{s/s} = \frac{\sigma}{4\pi} \log\left((X - X_1)^2 + (Y - Y_1)^2\right) \qquad (E.7)$$

where ϕ is the strength and X_1, Y_1 are the location of the source/sink. X and Y are non-dimensional spatial variables in the unmapped domain. The Joukowski conformal mapping function is used here to map the circle of radius b in a flat plate of semi-chord b. With this special conformal transformation all the points on the circle are mapped directly

to the flat plate whereas all the other points are mapped outside the circle (Figure E.2). The transformation is the following

$$x + iy = X + iY + \frac{b^2}{X + iY} \qquad (E.8)$$

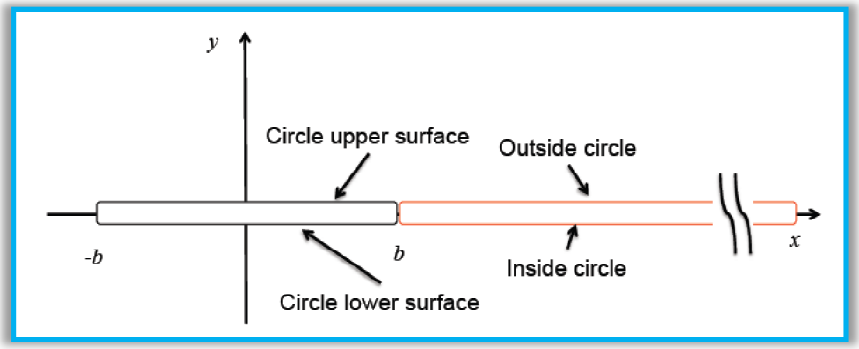

Figure E.2: Transformation of the circle points into the flat plate.

If a double source of strength 2σ is placed at a point (X_1, Y_1) and a double sink of strength -2σ is placed at a point $(X_1, -Y_1)$, like in Figure E.3, the total velocity potential of the source/sink pair is found by summing the singular velocity potential expressions, obtaining

$$\phi_{s/s} = \frac{\sigma}{2\pi} \log\left(\frac{(X - X_1)^2 + (Y - Y_1)^2}{(X - X_1)^2 + (Y + Y_1)^2}\right) \qquad (E.9)$$

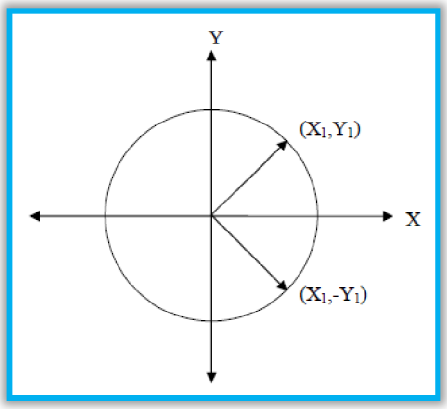

Figure E.3: Locations of the double sources.

Now, using the conformal transformation on the surface of the circle, it is possible to obtain the following expression for the mapped velocity potential on the surface of the airfoil:

$$\phi_{s/s} = \frac{\sigma}{2\pi} \log \left(\frac{(x - x_1)^2 + \left(\sqrt{1 - x^2} - \sqrt{1 - x_1^2}\right)^2}{(x - x_1)^2 + \left(\sqrt{1 - x^2} + \sqrt{1 - x_1^2}\right)^2} \right) \qquad (E.10)$$

Integrating the expression along the chord gives a general relationship for the velocity potential due to the source/sink pair sheet

$$\phi_{\underline{s}} = \frac{b}{2\pi} \int_{-1}^{1} \sigma(x, t) \log \left(\frac{(x - x_1)^2 + \left(\sqrt{1 - x^2} - \sqrt{1 - x_1^2}\right)^2}{(x - x_1)^2 + \left(\sqrt{1 - x^2} + \sqrt{1 - x_1^2}\right)^2} \right) dx_1$$

$$(E.11)$$

The velocity must satisfy the boundary condition of impermeability and, as it has been said previously in Chapter E.1, the strength of the source/sink sheet depend on this condition. Approaching the surface of the source/sink sheet, the velocity must be perpendicular to the surface: the velocity of the flow which is flowing out of the source represent the strength of the source. For a generic airfoil shape, the strength of the source/sink could be written as

$$\sigma(x, t)_{s/s} = U \frac{\partial y(x, t)}{\partial x} + b \frac{\partial y(x, t)}{\partial t} \qquad (E.12)$$

where U is the free stream velocity.

If the airfoil deformation expression $y(x, t)$ (equation $E.5$) is substituted into the source/sink strength equation $(E.12)$ and this equation is substituted into the velocity potential expression (equation $E.11$), it is possible to obtain the potential for the non-circulatory flow as a function of x.

Now that the potential is calculated, it is necessary to obtain an expression for the lift force in order to compare the results with the Peters's ones. Therefore, the next step is to calculate the pressure with Bernoulli's equation

$$p_0 = p + \frac{1}{2}\rho U^2 + \rho \frac{\partial \phi}{\partial t} \qquad (E.13)$$

that gives the following expression for the total pressure in the free stream flow

$$p_0 = p_\infty + \frac{1}{2}\rho U^2 \qquad (E.14)$$

where ρ is the density of the air.

Considering small disturbances, it is possible to linearize and rewrite the equation as

$$p_0 - p_\infty = -\rho\left(\frac{U}{b}\frac{\partial\phi}{\partial x} + \frac{\partial\phi}{\partial t}\right) \qquad (E.15)$$

The difference between the velocity potential of two locations is equal to the integral of the velocity along the surface between the two locations. This assertion gives

$$\phi_2 - \phi_1 = \int_{x_1}^{x_2} U' dx \qquad (E.16)$$

where x_1 and x_2 are the locations and ϕ_1 and ϕ_2 are the velocity potentials respectively.

In the unmapped domain (the circle), the flows in two locations that are antisymmetric must be the same. This condition has to be satisfied also in the mapped domain (the flat plate) giving the following result:

$$\phi_{LE} - \phi_U(x) = \phi_L(x) - \phi_{LE} \qquad (E.17)$$

where ϕ_{LE} is the potential at the leading edge, ϕ_U is the potential in a location on the upper surface of the circle and ϕ_L is the potential in the antisymmetric location respect to the previous one in the lower surface. Thus the pressure difference between the upper and lower surface is

$$p_L - p_U = -2\rho\left(\frac{U}{b}\frac{\partial\phi_U}{\partial x} + \frac{\partial\phi_U}{\partial t}\right) \qquad (E.18)$$

The integration of the previous equation gives the lift force for the non-circulatory flow

$$L_{NC} = b\int_{-1}^{1}(p_L - p_U)\,dx = -\pi\rho b^2\left[U\dot{\alpha} + \ddot{h} - \frac{b^2}{8}\ddot{k}_1\right] \qquad (E.19)$$

where $\dot{\alpha}$ is the pitch velocity, $\ddot{h}$ is the plunge acceleration and $\ddot{k}_1$ is the second derivative of the first high order shape term.

E.4) LIFT DUE TO CIRCULATORY FLOW

The non-circulatory flow does not satisfy the Kutta condition, which states that the pressure difference at the trailing edge should be zero. This can be seen if $x = 1$ is put in the pressure difference equation: a nonzero value is obtained. Thus, a second flow has to be developed to satisfy this condition.

The circulatory flow is the answer and is developed using a sheet of vortices on the body and on the wake. The velocity potential for a point vortex ϕ_v is

$$\phi_v = \frac{\Gamma}{2\pi}\tan^{-1}\left(\frac{Y - Y_1}{X - X_1}\right) \qquad (E.20)$$

where Γ is the strength of the vortex.

In general, the locations of the vortex on the wake follow the motion of the airfoil but for small disturbances the wake can be approximated by a flat wake with negligible errors. Under these hypothesis, the vortex sheet of the wake can be considered moving downstream along the x-axis at the free stream velocity U. accordingly with Kelvin's condition, the magnitude of the wake circulation will be always equal and opposite to the circulation of the airfoil, and constant in time.

In the unmapped domain, the point vortices are located one into the circle at $(1/X_0, 0)$ and the other one outside the circle, in the wake at $(X_0, 0)$ respectively (Figure E.4).

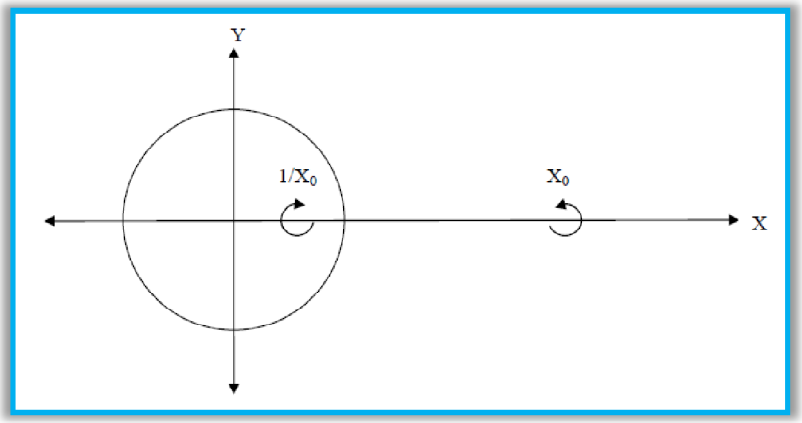

Figure E.4: Locations of the vortices.

The singularities have equal but opposite strength: this guarantee the condition that the total circulation is zero and, in addition, the condition of impermeability of the surface. The velocity potential for such a pair of vortices is given as,

$$\phi_{\Gamma_0} = \frac{\Gamma}{2\pi}\left[\tan^{-1}\left(\frac{Y-Y_0}{X-X_0}\right) - \tan^{-1}\left(\frac{Y-Y_0}{X-\frac{1}{X_0}}\right)\right] \qquad (E.21)$$

where Γ is the strength of each point vortex.

Applying the Joukowski mapping (equation E.18), the expression above become

$$\phi_{\Gamma_0} = -\frac{\Gamma}{2\pi}\tan^{-1}\left[\left(\frac{\sqrt{1-x^2}\sqrt{x_0^2-1}}{1-xx_0}\right)\right] \qquad (E.22)$$

where x is the chord variable in the mapped plane and x_0 is the location of the vortices, which is on the x-axis as it was in the unmapped dominion.

The pressure difference due to the circulatory flow is given as,

$$\Delta p = -\frac{2\rho U}{b}\left[\frac{\partial\phi}{\partial x} + \frac{\partial\phi}{\partial x_0}\right] \qquad (E.23)$$

Differentiating equation $(E.21)$ and substituting it into the pressure difference expression lead to the following result

$$\Delta p = -\frac{\rho U b \Gamma}{\pi}\left[\frac{x_0 + x}{\sqrt{1-x^2}\sqrt{x_0^2-1}}\right] \qquad (E.24)$$

The integration of equation $(E.24)$ along the chord permits to obtain the expression of the lift for the circulatory flow, which is:

$$L_C = -\rho U \Gamma \frac{x_0}{\sqrt{x_0^2-1}} \qquad (E.25)$$

where the strength of the circulation is given by $\Gamma = b\gamma_w(x_0, t)dx_0$ with $\gamma_w(x_0, t)$ the circulation per unit length.

Substituting this expression of the circulation into the lift equation gives

$$L_C = -\rho U b \int_1^\infty \frac{x_0}{\sqrt{x_0^2 - 1}} \gamma_w(x_0, t) dx_0 \qquad (E.26)$$

that is the lift for the circulatory flow.

The velocity potential for the vortex sheet is then

$$\phi_\Gamma = -\frac{b}{2\pi} \int_1^\infty \tan^{-1}\left(\frac{\sqrt{1-x^2}\sqrt{x_0^2-1}}{1-xx_0}\right) \gamma_w(x_0, t) dx_0 \qquad (E.27)$$

The magnitude of the circulation, $\gamma_w(x_0, t)$, is determined by the Kutta condition, which force the flow to leave the trailing edge smoothly or, in other words, that force the velocity at the trailing edge to be finite. This latter assumption permit to have a useful equation for the deformation shape

$$\frac{1}{2\pi} \int_1^\infty \sqrt{\frac{x_0+1}{x_0-1}} \gamma_w(x_0, t) dx_0 = U\alpha + \dot{h} + \frac{b}{2}\dot{\alpha} + \frac{Ub}{2} k_1 + \frac{Ub^2}{8} k_2 + \frac{Ub^3}{48} k_3 = Q$$

$$(E.28)$$

that can be used to calculate the lift

$$L_C = -2\pi\rho U b Q \frac{\int_1^\infty \frac{x_0}{\sqrt{x_0^2-1}} \gamma_w(x_0, t) dx_0}{\int_1^\infty \sqrt{\frac{x_0+1}{x_0-1}} \gamma_w(x_0, t) dx_0} = -2\pi\rho U b Q C(k) \qquad (E.29)$$

where $C(k)$ is the Theodorsen's function, explained in the following Chapter.

E.5) THEODORSEN'S FUNCTION

The hypothesis which validate the equations written till now is the assumption of small disturbances. If the motion is considered harmonic, there is a solution to the ratio of integrals above and therefore it is possible to calculate the lift force. To obtain this result, the motion is written as a function of frequency of harmonic oscillation

$$\alpha(x, t) = \bar{\alpha} e^{i(wt + \varphi_\alpha)} \qquad (E.30)$$

$$h(x, t) = \bar{h} e^{i(wt + \varphi_h)} \qquad (E.31)$$

$$k_1(x, t) = \bar{k}_1 e^{i(wt + \varphi_{k_1})} \qquad k_2(x, t) = \bar{k}_2 e^{i(wt + \varphi_{k_2})}$$

$$k_3(x,t) = \bar{k}_3 e^{i(wt+\varphi_{k_3})}$$

$$(E.32)$$

where $\bar{\alpha}$, $\bar{h}, \bar{k}_1$, $\bar{k}_2$, $\bar{k}_3$ are the magnitude of the oscillation, w is the frequency and t the time. The terms in φ are the phases of the motion.

Also the wake vortex sheet strength is written in terms of oscillatory motion

$$\gamma_{wake}(x,t) = \bar{\gamma}_{wake} e^{i(wt-kx)} \qquad (E.33)$$

where $k = wb/U$ is the reduced frequency.

As said before, the motion written as an harmonic oscillation permits to calculate the ratio of integrals with Theodorsen's function denoted by $C(k)$. This function depend only on the reduced frequency k and take the form of Hankel functions:

$$C(k) = F(k) + iG(k) = \frac{H_1^{(2)}(k)}{H_1^{(2)}(k) + iH_0^{(2)}(k)} \qquad (E.34)$$

where

$$F(k) = \frac{J_1(k)\big(J_1(k) + Y_0(k)\big) + Y_1(k)(Y_1(k) - J_0(k))}{(J_1(k) + Y_0(k))^2 + (Y_1(k) - J_0(k))^2} \qquad (E.35)$$

$$G(k) = \frac{Y_1(k)Y_0(k) + J_1(k)J_0(k)}{(J_1(k) + Y_0(k))^2 + (Y_1(k) - J_0(k))^2} \qquad (E.36)$$

are the real and imaginary parts of $C(k)$ plotted in Figure E.5.

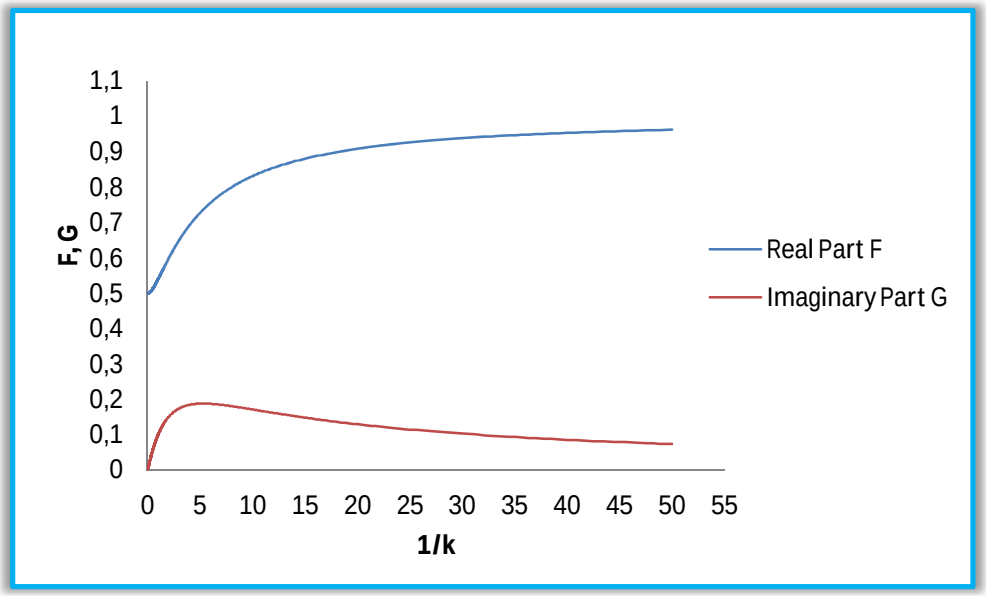

Figure E.5: Theodorsen's function. Real (F) and imaginary (G) parts.

A complex plot of $C(k)$ is given in Figure E.6 below.

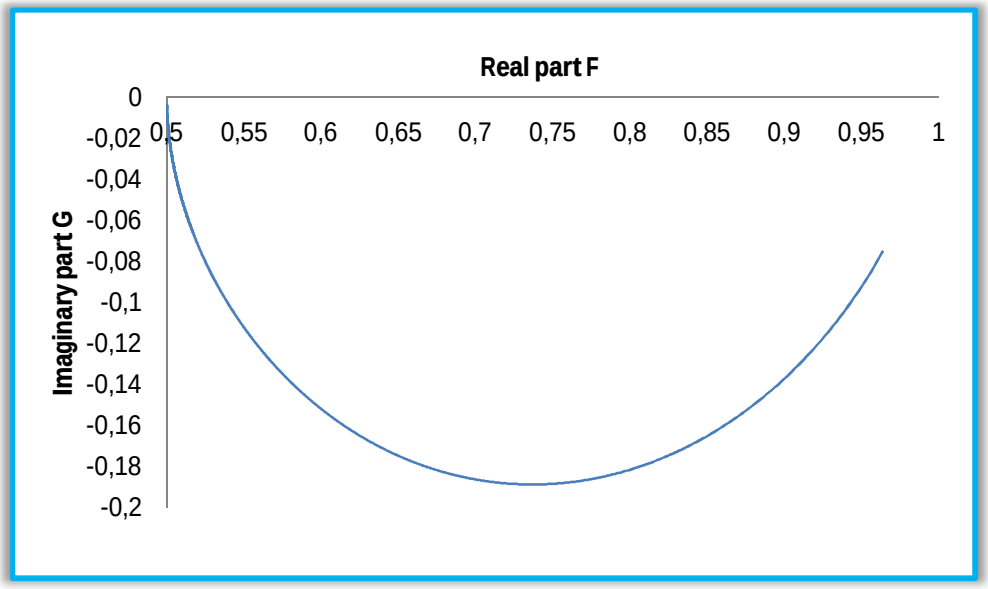

Figure E.6: Theodorsen's function C(k).

The function reduces the amplitude of the circulatory lift with increasing reduced frequency of oscillation: it is a reduction factor which depends on the frequency of oscillation. It can be seen as a measure of

unsteadiness and it gives information about which combination of frequency, chord length and free-stream velocity give an equal unsteady flow. With such information it is possible to ignore the effect of the wake.

The Hankel functions are a complex combinations of Bessel function of the first $J_n(k)$ and second $Y_n(k)$ kind (Figures E.7 and E.8 respectively).

$$H_n^{(2)}(k) = J_n(k) - iY_n(k) \qquad (E.37)$$

$$H_0^{(2)}(k) = J_0(k) - iY_0(k) \qquad H_1^{(2)}(k) = J_1(k) - iY_1(k) \qquad (E.38)$$

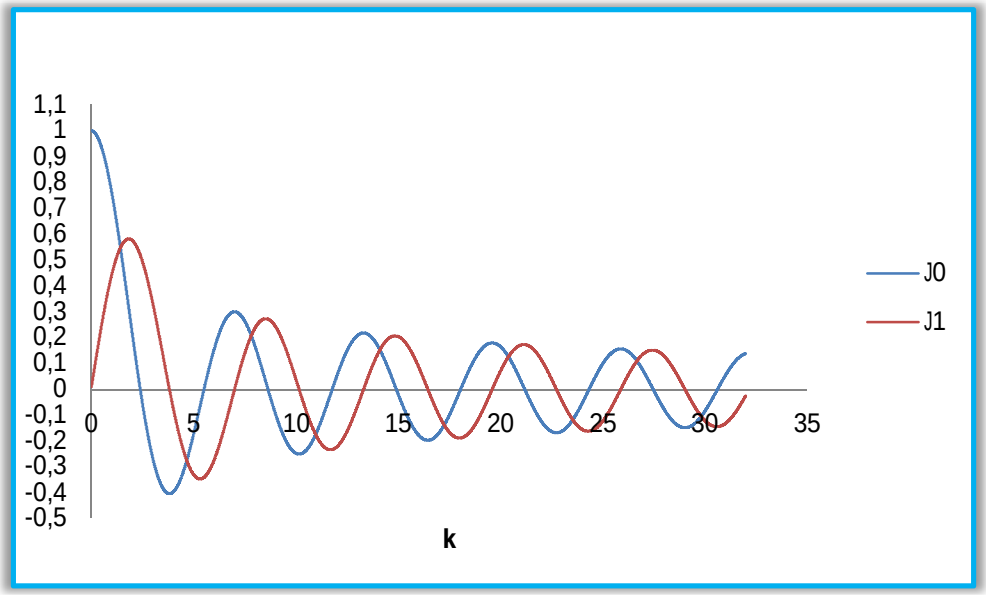

Figure E.7: Bessel functions of the first kind.

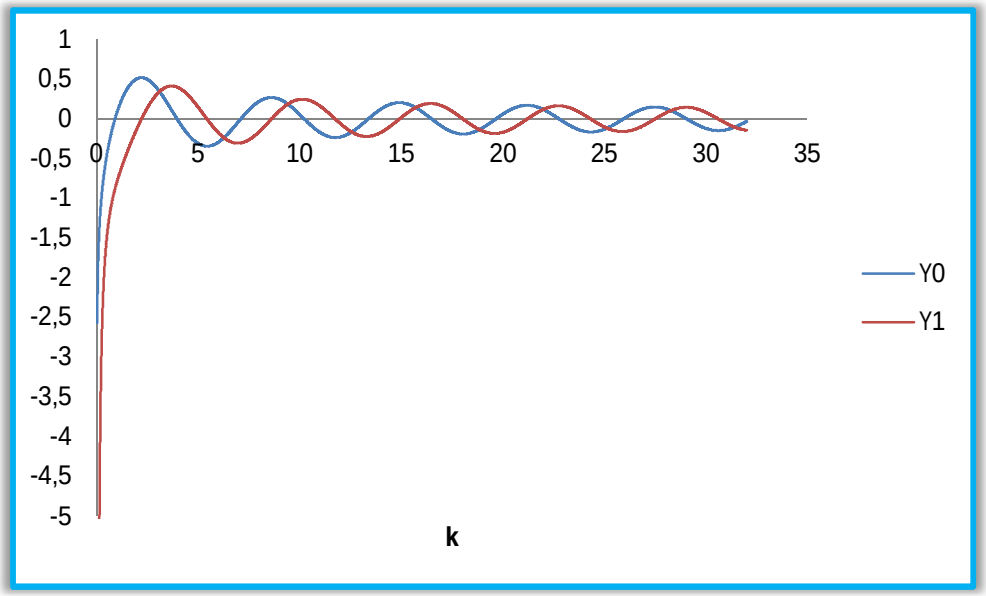

Figure E.8: Bessel functions of the second kind.

E.6) TOTAL LIFT EXPRESSION

The addition of the circulatory and non-circulatory components give the complete lift. The final expression is complex, where the amplitude of the complex number is the amplitude of oscillation and the phase is the phase of the force relative to the phase of the motion.

$$L = L_{NC} + L_C = -\pi\rho b^2\left[U\dot{\alpha} + \ddot{h} - \frac{b^2}{8}\ddot{k}_1\right] - 2\pi\rho UbQC(k)$$

$$= -\pi\rho b^2\left[U\dot{\alpha} + \ddot{h} - \frac{b^2}{8}\ddot{k}_1\right]$$

$$- 2\pi\rho UbC(k)\left(U\alpha + \dot{h} + \frac{b}{2}\dot{\alpha} + \frac{Ub}{2}k_1 + \frac{Ub^2}{8}k_2\right.$$

$$\left. + \frac{Ub^3}{48}k_3\right) \qquad (E.39)$$

From the expression above, it is possible to obtain the lift contributions due to each deformation shape, corresponding velocities and accelerations. Table E.1 shows these contributions. The first two rows of the table match Theodorsen's results.

Table E.1: Lift contributions derived from Theodorsen/Garrick theory.

	1	$\frac{\partial}{\partial t}$	$\frac{\partial^2}{\partial t^2}$
h	0	$-2\pi\rho UbC(k)$	$-\pi\rho b^2$
α	$-2\pi\rho U^2 bC(k)$	$-\pi U\rho b^2[C(k)+1]$	0
k_1	$-\pi\rho U^2 b^2 C(k)$	0	$-\frac{1}{8}\pi\rho b^4$
k_2	$-\frac{1}{4}\pi\rho U^2 b^3 C(k)$	0	0
k_3	$-\frac{1}{24}\pi\rho U^2 b^4 C(k)$	0	0

The table shows easily which airfoil motion shape contribute to the lift and also the existence of Theodorsen's term $C(k)$ display instantly if the lift force is due to circulatory or non-circulatory flow. The first column represent only the circulatory forces (static airfoil shapes) because there are no acceleration or velocities that can contribute to the circulatory flow. The second column shows that the plunge velocity contributes to the lift force in the same form as a static angle of attack. This is quite obvious because a constant velocity in the plunge direction can resemble a static angle of attack. The third column shows that only two airfoil motion shapes contribute to the lift force and that both terms are non-circulatory.

Now, if a generic airfoil is forced to a small harmonic motion, Peters theory gives the same results as Theodorsen and Garrick. From Chapter 5 (equation 5.22) the lift force is given by

$$L = -2\pi\rho bf u_0(w_0 - \lambda_0) - \pi\rho b u_0 w_1 - \pi\rho b^2\left(\dot{w}_0 - \frac{1}{2}\dot{w}_2\right) \qquad (E.40)$$

If the components of the total velocity field w_n and the accelerations $\dot{w}_n$ are replaced with the ones derived in Chapter 5 and λ_0 is substituted by

$$\lambda_0 = (w_0 + w_1)[1 - C(k)] \qquad (E.41)$$

the results are quite the same obtained in table E.1 and shown in table E.2. This means that the two theories are really similar and can both be implemented in ONERA model.

Table E.2: Lift contributions derived from Peters' theory.

	1	$\frac{\partial}{\partial t}$	$\frac{\partial^2}{\partial t^2}$
h_0	0	$-2\pi\rho u_0 bC(k)$	$-\pi\rho b^2$
h_1	$-2\pi\rho u_0^2 C(k)$	$-\pi u_0 \rho b^2[C(k)+1]$	0
h_2	$-4\pi\rho u_0^2 C(k)$	0	$-\frac{1}{2}\pi\rho b^2$
h_3	$-6\pi\rho u_0^2 C(k)$	0	0
h_4	$-8\pi\rho u_0^2 C(k)$	0	0

This result was also shown in Section 8.2 for harmonic pitch and flap simulations.

APPENDIX F: WAKE MODEL

The formation of lift around an airfoil is associated to the presence of a circulation $\Gamma(t) \neq 0$ (Figure F.1). Every variation in the condition of motion of the airfoil is followed by a variation in the circulation. Since the global circulation must be preserved, as a consequence, a vortex must detaches from the trailing edge of the airfoil.

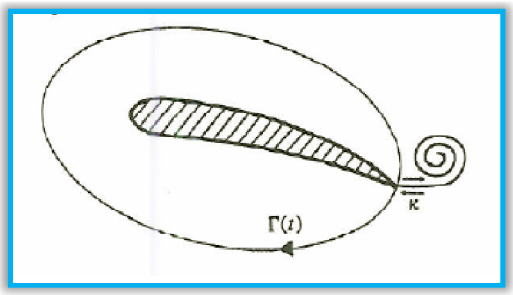

Figure F.1: Circulation variation and formation of a trailing edge vortex. Source of the figure: Reference [5].

The strength of this vortex must be equal to the variation in the circulation and its rotation must be opposite the one of the circulation. If the condition of motion of the airfoil varies with continuity, then a continuous detachment of vorticies is produced and gives the formation of a wake.

The wake shed from the trailing edge of an airfoil can be modeled by doublet or vortex distributions (Figure F.2). For simplicity, a discrete vortex model of this continuous vortex sheet is adopted here. The strength of each vortex is equal to the vorticity shed during the corresponding time step and therefore the location and strength of each vortex element must be specified at every step.

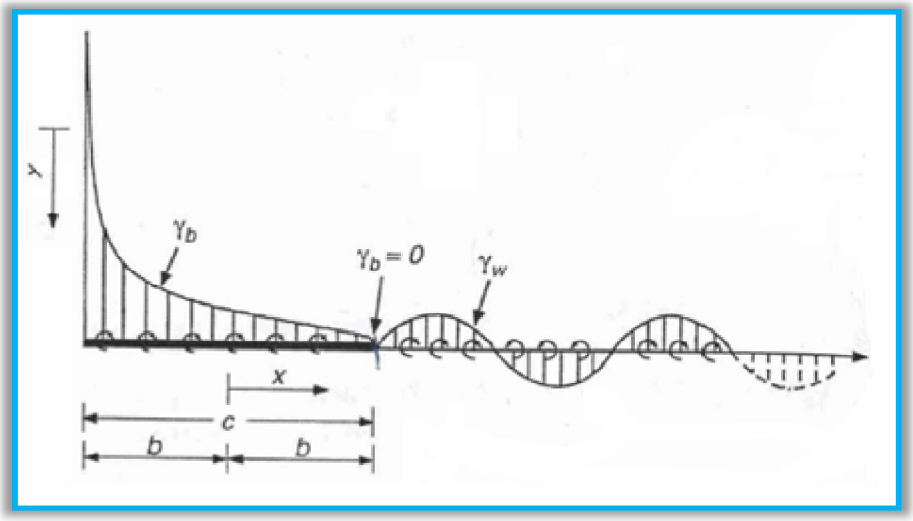

Figure F.2: Wake shed from the trailing edge. Source of the figure: Reference [5].

What is needed is the components of velocity due to the shed wake, $\{\lambda_n\}$, because they induce a velocity field in the plane of motion of the airfoil that alter the overall flow around the body. These components are obtained by the calculation of the downwash due to the wake. Before doing this, the wake's circulation at each time step is necessary and it can be found applying the Kelvin's condition. The components of velocity are so important because once they are collected it is possible to proceed on with the calculation of the generalized loads.

Consider now the airfoil. At the beginning of the motion the first wake element is produced. The location of this first element is the trailing edge, where $x = b$ in concordance with the position of the coordinate system (mid-chord). Although the airfoil can moves in the xz plane, the wake is considered mono-dimensional and it spreads along the x-axis. Therefore, at each time step, the position of the wake's elements is specified by only the x coordinate. The strength of this element is found by the application of the Kelvin's condition:

$$\frac{d\Gamma}{dt} = \frac{d\Gamma(t)}{dt} + \frac{d\Gamma_w}{dt} = 0 \qquad (F.1)$$

where $\Gamma(t)$ is the airfoil's circulation and Γ_w is the wake's circulation. For the first time step the Kelvin's condition led to:

$$\Gamma(t) + \Gamma_{w1} = 0 \qquad (F.2)$$

from which is obtained the value of Γ_{w1}.

At the second time step the first wake's element moves along the x-axis of a specific quantity that is given by $U\Delta t$, where U is the flow velocity whereas Δt is the time step. Contemporaneously a second wake's element forms at the trailing edge of the airfoil. Once again the Kelvin's condition has to be met and thus, for this second element, it is possible to write the following equation:

$$\Gamma_{w2} = -[\Gamma(t_2) + \Gamma_{w1}] \qquad (F.3)$$

where $\Gamma(t_2)$ is the total circulation of the airfoil (that has changed) at the second time step and Γ_{w1} is the previous wake's circulation due to the first wake's element. The assumption made here is that there is no vortex decay. Accordingly to Helmholtz theorems, if a wake vortex element is shed from the trailing edge, its strength will be conserved.

By assuming that the Kelvin condition was met at each previous time step, it is possible to write the following equation for the ith time step:

$$\Gamma_{wi} = -\left[\Gamma(t_i) + \sum_{k=1}^{i-1} \Gamma_{wk}\right] \qquad (F.4)$$

where k is the counter of the wake vorticies.

Now, recalling that the downwash induced by the airfoil bound circulation $\gamma_b(\xi, t)$ (Chapter 5) is

$$\bar{v} = -\frac{1}{2\pi}\int_{-b}^{+b} \frac{\gamma_b(\xi, t)}{x - \xi} d\xi \qquad (F.5)$$

it is possible to calculate the total downwash induced on the airfoil by simply adding the downwash due to the N_w discrete vortices of the wake

$$w_w = \frac{\partial \phi_w}{\partial z}(x, t)_{z=0} = \sum_{k=1}^{N_w} \frac{-\Gamma_k}{2\pi} \frac{1}{(x - x_k)} \qquad (F.6)$$

where x_k is the position of the kth wake's vortex.

Finally, imposing boundary condition, the unsteady motion of a two-dimensional thin airfoil theory gives

$$\frac{\partial \phi_B}{\partial z} = \bar{v} = -\frac{1}{2\pi}\int_{-b}^{+b} \frac{\gamma_b(\xi, t)}{x - \xi} d\xi =$$

$$U(t)\frac{\partial \eta(x,t)}{\partial x} - w_w - \dot{\theta}(t)x + \frac{\partial \eta(x,t)}{\partial t} \qquad 0 < x < c \qquad (F.7)$$

which is the time-dependent equivalent of the steady-state boundary condition and must hold for each point x on the airfoil's chord. In addition, the Kutta condition must be respected for this flow, i.e.

$$\gamma_b(c, t) = 0 \qquad (F.8)$$

APPENDIX G: MATLAB CODE FLOW CHART OF ONERA MODEL

The following flow chart recap what the MATLAB code implemented by Onur [2] does. The code, developed to validate ONERA model, is divided into three files:

- the main program, that defines the testing conditions and integrates the system of differential equations;
- the original ONERA Edlin Model, that contains all the differential equations of structure and the Onera Model;
- the modified ONERA Model by Laxman, that contains all the differential equations of structure and the Onera Model.

In addition, there are other four files that contain the characteristics and the parameters of the airfoils, calculate the linear flutter and plot the results. These files are called from the main program or from the ONERA model in order to integrate the differential equations with the ODE15s solver.

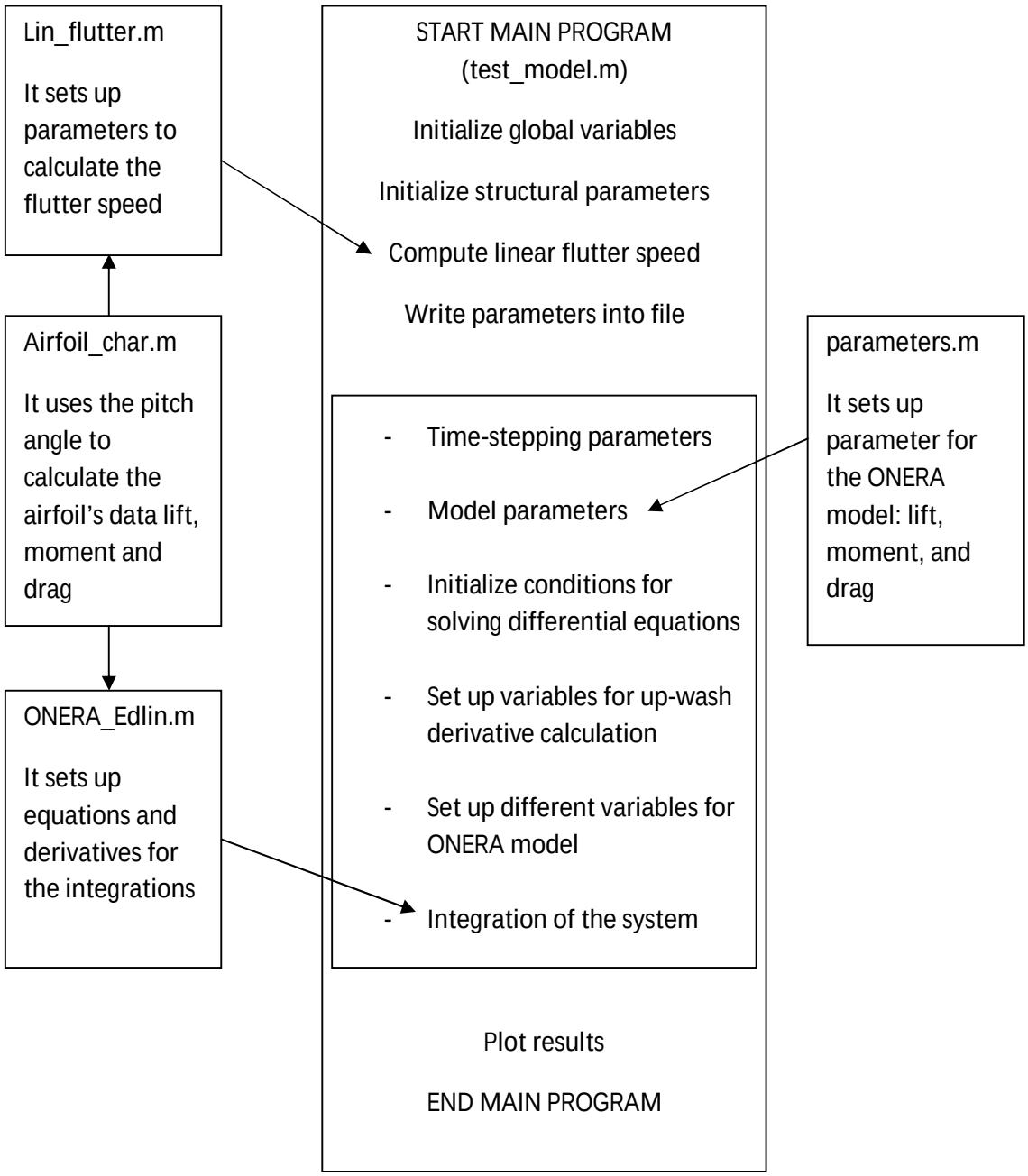

Figure G.1: Matlab code's flowchart.

The main program is called test_model.m. When the simulation starts, it begins with the initialization of the global variables (i.e. variables that are shared with the other sub-functions of the code) and the structural parameters. The flutter speed is not considered for the validation.

Flutter is a self-feeding and potentially destructive vibration that produces rapid periodic motion of an airfoil. It occurs when aerodynamic forces on the airfoil couple with his natural mode of vibration. This phenomenon is self-fed because the vibrational movement increases the aerodynamic load which in turn drives the airfoil to move further. It could create a vicious circle in which, if the energy input by the aerodynamic excitation is larger than the one dissipated by the damping in the system, the amplitude of vibration will increase, resulting in a self-exciting oscillation that could lead to rapid failure.

The core of the main program is the time-step integration of the system. The goal of this part of the program is to calculate the differential equations of the ONERA model. Therefore it calls the parameters for the model (parameters.m) and starts the integration of the equations contained in the sub-function ONERA_Edlin.m. The final step is the plot of the results.

BIBLIOGRAPHY

[1] D. Petot – Differential Equation Modeling Of Dynamic Stall. *Rech. Aérosp.* – n°1989 – 5.

[2] O. Celebi – Aerodynamic Analysis Of A Typical Airfoil Section Using the ONERA Model, *EH401 Project, Department of Aeronautics, Imperial College*, 2010.

[3] Daniel J. Rudy – Three Interpretations of the ONERA Dynamic Stall Model with Applications to Rotor Blade Flapping Response. *Master of Sciences Thesis, Washington University*, St. Louis, Missouri, 1983.

[4] Loren A. Ahaus – An Airloads Theory For Morphing Airfoils In Dynamic Stall With Experimental Correlations. *A Dissertation Presented to the School of Engineering of Washington University*, St. Louis, Missouri, May 2010.

[5] C. Marongiu – Dynamic Stall. *Seminar during the Course of Rotors Aerodynamics*, CIRA (Italian Aerospace Research Center), University "Federico II", Naples, 27th May 2009.

[6] W. P. Walker – Unsteady Aerodynamics of Deformable Thin Airfoils, Faculty of the Virginia Polytechnic Institute and State University, Blacksburg, Virginia, August 5 2009.

[7] R. Jain, K. Szema,R. Munipalli, H. Yeo, and I. Chopra – CFD-CSD analysis of active control of helicopter rotor for performance improvement. *Proceedings of the American Helicopter Society 65th Annual Forum*, Grapevine, Texas, USA, 27-29 May 2009.

[8] M. S. Chandrasekhara, P.B. Martin, and C. Tung – Compressible Dynamic Stall Control Using a Variable Droop Leading Edge Airfoil. *Journal of Aircraft*, 41(4):862-869, July-August 2004.

[9] W. J. McCroskey – A Critical Assessment of Wind Tunnel Results for the NACA 0012 Airfoil. *NASA TM 100019*, October 1987.

[10] W. J. McCroskey – The Phenomenon of Dynamic Stall. *NASA TM 81264*, March 1981.

[11] T. Theodorsen – General Theory of Aerodynamic Instability and the Mechanism of Flutter. *NACA Rept. 496*, May 1934.

[12] A. Krzysiak and J. Narkiewicz – Aerodynamic Loads on Airfoil with Trailing edge Flap Pitching with Different Frequencies. *Journal of Aircraft*, 43(2):407-418, March-April 2006.

[13] D. A. Peters, S. Karunamoorthy and W. Cao – Finite State Induced Flow Models Part I: Two-Dimensional Thin Airfoil. *Journal of Aircraft*, 32(2):313-322, March-April 1995.

[14] T. Theodorsen – General Theory of Aerodynamic Instability and the Mechanism of Flutter. *NACA TR No. 496*, May 1934.

[15] I. E. Garrick – Propulsion of a Flapping and Oscillating Airfoil. *NACA TR No. 567*, May 1936.

[16] L. Ahaus – Correlating Unsteady Airloads Theory and Oscillating Airfoil Data with Dynamic Stall. 2008 *Robert L. Lichten Award competition*.

[17] J.Murua, R. Palacios, J. Peirò – Camber Effects in the Dynamic Aeroelasticity of Compliant Airfoils. *Journal of Fluids and Structures*, 527-543, 29 January 2010.

[18] D. A. Peters, M. Hsieh and A. Torrero – A State-Space Airloads Theory for Flexible Airfoils. In *Proceedings of the American Helicopter Society 62nd Annual Forum*, May 2006.

[19] D. A. Peters, D. Barwey and M. Johnson – Finite-State Airloads Modeling with Compressibility and Unsteady Free-Stream. In *Proceedings of the Sixth International Workshop on Dynamics and Aeroelastic Stability Modeling of Rotorcraft Systems*, November 1995.

[20] D. A. Peters –Towards a Unified Lift Model for Use in Rotor Blade Stability Analysis. *40th Annual Forum of the American Helicopter Society*, Arlington/Va, 1984.

[21] V. Laxman and C. Venkatesan – Chaotic Response of an Airfoil due to Aeroelastic Coupling and Dynamic Stall. *AIAA Journal*, 45 (1), 271-280, 2007.

[22] Mac Gaunaa – Investigation of the Effect of Deformable Trailing Edge Geometry Control Systems on Flutter Velocity. *Risø National Laboratory, Wind Energy Department*, 2007.

[23] Mac Gaunaa – Unsteady Two-Dimensional Potential-Flow Model for Thin Variable Geometry Airfoils. *Risø-DTU National Laboratory for Sustainable Energy, Wind Energy Division*, Roskilde, Denmark, 2010.

[24] C. P. van Dam, R. Chow, J. R. Zayas and D. E. Berg – Computational Investigations of Small Deploying Tabs and Flaps for Aerodynamic Load Control. *Journal of Physics*, Conf. Ser. 75 012027, 2007.

[25] B. Santiago – Load Alleviations in Wind Turbines Using Variable Airfoil Geometry (a Two-Dimensional Analysis). *Technical University of Denmark, Fluid Mechanics Section*. February 12, 2004.

[26] D. Petot. Progress in the semi-empirical prediction of the aerodynamic forces due to large amplitude oscillations of an airfoil in attached or separated flow. In *Proceedings of the Ninth European Rotorcraft Forum*, September 1983.

[27] K. McAlister, O. Lambert, and D. Petot. Application of the ONERA model of dynamic stall. *NASA Technical Paper 2399*, 1984.

[28] P. B. Martin, K. W. McAlister, M. S. Chandrasekhara, and W. Geissler. Dynamic stall measurements and computations for a VR-12 airfoil with a variable droop leading edge. In *Proceedings of the American Helicopter Society 59th Annual Forum*, May 2003.

[29] J. G. Leishman. Principles of helicopters aerodynamics. Cambridge University press, 2000.